COPPE
Instituto Alberto Luiz Coimbra de Pós-Graduação e Pesquisa de Engenharia
UFRJ

NONLINEAR STIFFNESS CONCEPT IN WAVE ENERGY CONVERSION

Zhijia Wu

Tese de Doutorado apresentada ao Programa de Pós-graduação em Engenharia Oceânica, COPPE, da Universidade Federal do Rio de Janeiro, como parte dos requisitos necessários à obtenção do título de Doutor em Engenharia Oceânica.

Orientadores: Segen Farid Estefen
Carlos Antonio Levi da Conceição

Rio de Janeiro
Dezembro de 2019

NONLINEAR STIFFNESS CONCEPT IN WAVE ENERGY CONVERSION

Zhijia Wu

TESE SUBMETIDA AO CORPO DOCENTE DO INSTITUTO ALBERTO LUIZ COIMBRA DE PÓS-GRADUAÇÃO E PESQUISA DE ENGENHARIA DA UNIVERSIDADE FEDERAL DO RIO DE JANEIRO COMO PARTE DOS REQUISITOS NECESSÁRIOS PARA A OBTENÇÃO DO GRAU DE DOUTOR EM CIÊNCIAS EM ENGENHARIA OCEÂNICA.

Orientadores: Segen Farid Estefen
Carlos Antonio Levi da Conceição

Aprovada por: Prof. Segen Farid Estefen
Prof. Carlos Antonio Levi da Conceição
Prof. Antonio Carlos Fernandes
Prof. Edson Hirokazu Watanabe
Dr. Allan Carré de Oliveira
Prof. Joel Sena Sales Junior
Prof. Renato Maia Matarazzo Orsino

RIO DE JANEIRO, RJ – BRASIL
DEZEMBRO DE 2019

Wu, Zhijia

Nonlinear stiffness concept in wave energy conversion/Zhijia Wu. – Rio de Janeiro: UFRJ/COPPE, 2019.

XX, 124 p.: il.; 29, 7cm.

Orientadores: Segen Farid Estefen

Carlos Antonio Levi da Conceição

Tese (doutorado) – UFRJ/COPPE/Programa de Engenharia Oceânica, 2019.

Referências Bibliográficas: p. 113 – 124.

1. Wave energy converter. 2. Point absorber. 3. Nonlinear stiffness system. 4. Latching control. I. Estefen, Segen Farid *et al.* II. Universidade Federal do Rio de Janeiro, COPPE, Programa de Engenharia Oceânica. III. Título.

To my dear family for their endless love, support and encouragement

Acknowledgement

It would not be possible to accomplish the present thesis without supports from many people. First, I would like to express my sincere gratitude to my supervisor, Prof. Segen Farid Estefen, who leads me to the area of ocean renewable energy and guides me with the methodology of conducting research.

I would like to thank my co-supervisor, Prof. Carlos Antonio Levi da Conceição, for his valuable suggestions and insightful comments, besides the hydrodynamics related to my topic. I have learned a lot from the enthusiastic discussion with him.

Special thanks to Dr. Milad Shadman. Thank you for the sincere advice on my thesis topic and the help through my entire study at LTS (Laboratório de Tecnologia Submarina). Dr. Gustavo Omar and Dr. Mojtaba Maali Amiri helped me a lot in CFD and other areas. I would express my gratitude to them as well.

Special thanks to all my friends. I feel very warm in such a foreign country because of their help. The talks on imagining the future, celebrations of various special days, and happy but uncommon travelings, made my life here much more colorful. The time living and studying together with them is my most precious memories in Rio de Janeiro.

Special thanks to Fabian Wendt, Kim Nielsen, Yi-Hsiang Yu because of their support in providing the data from the International Energy Agency (IEA) Ocean Energy Systems (OES) Task 10 project.

The financial support from the Brazilian National Council for the Improvement of Higher Education (CAPES) is gratefully acknowledged. Many thanks also go to the PENO and staff of LTS for all the help during my doctoral study.

I am also grateful for the support from the China Ship Scientific Research Center (CSSRC), not only the financial support but also allowing me such a valuable opportunity.

Last, but certainly not least, to my family: my wife, Jinyu Xu, thanks for her endless love encouraging me to insist on my study; my son, Anan, he is my most valuable reward; my parents and in-laws, thanks for their encouragement. I would not have reached this stage without their support.

Resumo da Tese apresentada à COPPE/UFRJ como parte dos requisitos necessários para a obtenção do grau de Doutor em Ciências (D.Sc.)

CONCEITO DE RIGIDEZ NÃO LINEAR NA CONVERSÃO DE ENERGIA DAS ONDAS

Zhijia Wu

Dezembro/2019

Orientadores: Segen Farid Estefen
Carlos Antonio Levi da Conceição

Programa: Engenharia Oceânica

A tese investiga o conceito de sistema de rigidez não linear na melhoria da conversão de energia das ondas para um conversor de energia das ondas do tipo absorvedor de ponto (PA). Uma esfera semi-submersível é adotada juntamente com as abordagens analíticas e de mesclagem no cálculo da força não linear de Froude-Krylov. A abordagem analítica é aprimorada para resolver a força não linear de Froude-Krylov na superfície molhada instantânea em condições regulares e irregulares de ondas com mais eficiência, ajustando a função de Bessel e a função exponencial com séries polinomiais adequadas de acordo com várias frequências de ondas.

A análise estática de uma sistema de rigidez não linear clássico com molas de compressão mecânica (NSMc) descreve três tipos de configurações: biestável, QZS (rigidez quase zero) e configuração monoestável. A resposta em condições de onda regulares indica que, com a abordagem não linear, a resposta de ressonância é empurrada até um período mais longo, além de ampliar a largura de banda da resposta. Um procedimento é estabelecido para determinar a região viável dos parâmetros do NSMc. Devido à consideração prática, as possíveis melhorias na conversão de energia das ondas associadas às vantagens do NSMc são dramaticamente enfraquecidas.

Em seguida, a sistema de rigidez não linear alternativo com cilindros pneumáticos (NSPn) é investigado na sequência, mostrando que em sua região viável, a produção anual de energia não reduz muito. Para o clima de ondas com um longo período na região costeira do Rio de Janeiro, Brasil, a PA poderia colher mais energia das ondas com o NSPn do que com o controle de trava. Além disso, a menor taxa de potência pico/média mostra que, usando o NSPn, o processo de absorção de energia é mais suave.

Abstract of Thesis presented to COPPE/UFRJ as a partial fulfillment of the requirements for the degree of Doctor of Science (D.Sc.)

NONLINEAR STIFFNESS CONCEPT IN WAVE ENERGY CONVERSION

Zhijia Wu

December/2019

Advisors: Segen Farid Estefen
Carlos Antonio Levi da Conceição

Department: Ocean Engineering

The thesis investigates the nonlinear stiffness system (NSS) concept in improving wave energy conversion for a point absorber (PA) type wave energy converter (WEC). One semi-submersible sphere is adopted together with the meshing and analytical approaches in calculating the nonlinear Froude-Krylov force. The analytical approach is improved to solve the nonlinear Froude-Krylov force at the instantaneous wetted surface in both regular and irregular wave conditions more efficiently through fitting Bessel function and exponential function with suitable polynomial series according to various wave frequencies.

The static analysis of one classical NSS with mechanical compression springs (NSMc) describes three types of configurations: bi-stable, QZS (quasi-zero stiffness), and mono-stable configuration. The response in regular wave conditions indicates that with the nonlinear approach the resonance response is pushed even to a longer period range, besides broadening the response bandwidth. One procedure is established to determine the feasible region of NSMc parameters. Due to the practical consideration, the potential improvements in wave energy conversion associated with the NSMc's advantages are dramatically weakened.

Then the alternative NSS with pneumatic cylinders (NSPn) is investigated in the sequence, showing that in its feasible region, the annual energy production (AEP) does not reduce too much. For the wave climate featuring a long period in the nearshore region of Rio de Janeiro, Brazil, PA could harvest more wave energy with the NSPn, than with the latching control. Moreover, the lower peak-to-average power ratio shows that using the NSPn, the process of power absorption is smoother.

Contents

List of Figures **xi**

List of Tables **xv**

List of Symbols **xvi**

List of Abbreviations **xix**

1 Introduction **1**

1.1 Overview 1

1.2 Motivation and objectives 2

1.3 Outline of the thesis 4

2 Literature Review **7**

2.1 Latching and declutching control 7

2.2 Two-body WEC 10

2.3 Nonlinear stiffness system 11

2.4 Nonlinear Froude-Krylov force 15

2.5 Summary 16

3 Mathematical Model **17**

3.1 Equation of motion 17

3.1.1 Linear model 18

3.1.2 Nonlinear model 19

3.1.3 Performance evaluation 30

3.2 Code-to-code verification 32

3.2.1 Free-decay test 32

3.2.2 Regular wave situations 33

3.2.3 Irregular wave situations 36

3.3 Summary 37

4 Nonlinear Stiffness System (NSS) in WEC **39**
4.1 NSS with mechanical compression springs (NSMc) . . . 39
4.1.1 Description . . . 39
4.1.2 Mathematical model . . . 41
4.2 Static characteristic analysis . . . 42
4.3 Response in regular wave . . . 46
4.3.1 Case without NSMc . . . 46
4.3.2 Case with NSMc . . . 51
4.4 Summary . . . 63

5 NSMc in WEC: Practical Considerations **64**
5.1 Irregular wave conditions . . . 64
5.1.1 spectrum . . . 64
5.1.2 Nonlinear Froude-Krylov force . . . 66
5.2 Convergence analysis in irregular waves . . . 67
5.2.1 Case without NSMc . . . 67
5.2.2 Case with NSMc . . . 72
5.3 Mechanical compression spring constraints . . . 74
5.3.1 NSMc Feasibility . . . 74
5.3.2 Feasible NSMc performance . . . 78
5.4 Summary . . . 83

6 Alternative NSS in WEC **84**
6.1 NSS with pneumatic cylinders (NSPn) . . . 84
6.1.1 Description . . . 84
6.1.2 Mathematical model . . . 84
6.2 Static characteristic analysis . . . 88
6.3 Validation and convergence analysis . . . 90
6.3.1 Response for regular wave conditions . . . 90
6.3.2 Convergence analysis for irregular wave conditions . . . 92
6.4 NSPn Feasibility . . . 92
6.5 Performance analysis . . . 99
6.5.1 The α effect . . . 99
6.5.2 The γ effect . . . 100
6.5.3 The C_d effect . . . 101
6.6 Comparisons . . . 102
6.6.1 Frequency response contour . . . 102
6.6.2 Performance in a given sea site . . . 105
6.7 Summary . . . 108

7 Conclusions and Future Work **109**
7.1 Conclusions 109
7.1.1 Nonlinear Froude-Krylov force model 109
7.1.2 NSS characteristics 110
7.1.3 NSS with nonlinear Froude-Krylov force model 110
7.2 Future work 111

Bibliography **113**

List of Figures

1.1 Schematic conceptual classification of wave energy converters 2
1.2 Possible approaches to improve wave energy conversion 3
1.3 Thesis organization 5

2.1 Illustration of latching control with constant latching duration 8
2.2 Schematics of two-body WECs 11
2.3 Schematics of NSS 12
2.4 CorPower buoy 13

3.1 Schematics of wetted surface 20
3.2 Schematics of a heaving sphere under 3 different situations 22
3.3 Taylor expansions of e^{kRx} with different kR values 28
3.4 Polynomial fittings of $J_0(kR\sqrt{1-x^2})$ and e^{kRx} with different kR values 28
3.5 Free decay response in heave 33
3.6 Heave RAO, no PTO damping 35
3.7 Heave RAO with optimal PTO damping 35
3.8 Normalized mean power with optimal PTO damping 36
3.9 Mean power for the irregular wave case, with $H_S = 11.0\,\text{m}$, $T_P = 15.4\,\text{s}$, optimal PTO damping 37
3.10 Annual average absorbed power AAP, with optimal PTO damping . . 38

4.1 Schematic view of NSS with mechanical compression springs (NSMc) 40
4.2 Schematic view of PA type WEC with the NSS 40
4.3 NSMc force and potential energy ($\alpha = 1.0$, $\gamma = 0.6$, $L = 2.0\,\text{m}$) 42
4.4 Sphere hydrostatic restoring force and potential energy 43
4.5 Sphere static characteristics with NSMc ($\alpha = 1.0$, $L = 2.0\,\text{m}$) 44
4.6 Sphere static characteristics with NSMc ($\gamma = 0.5$, $L = 2.0\,\text{m}$) 44
4.7 Sphere ($D = 5.0\,\text{m}$) hydrodynamic characteristics 47
4.8 CWR calculated by different approaches ($S = 0.010$) 49
4.9 CWR calculated by different approaches ($S = 0.018$) 49
4.10 CWR calculated by different approaches ($S = 0.025$) 49

4.11 Linear model results ($T = 7.0\,\mathrm{s}$): displacements, phase portraits, and spectrum 50
4.12 Analytical nonlinear model model results ($T = 7.0\,\mathrm{s}$): displacements, phase portraits, and spectrum 51
4.13 Sphere CWR without NSMc ($H = 1.0\,\mathrm{m}$) 51
4.14 Sphere CWR without NSMc ($H = 2.0\,\mathrm{m}$) 52
4.15 Sphere CWR with NSMc: bi-stable configuration ($H = 1.0$ m, $B_{PTO} = 10\,\mathrm{kNs/m}$) 53
4.16 Analytical nonlinear model results ($T = 3.1$ s, $B_{PTO} = 10\,\mathrm{kNs/m}$): displacements, phase portraits, and spectrum 53
4.17 Analytical nonlinear model results ($T = 10.1$ s, $B_{PTO} = 10\,\mathrm{kNs/m}$): displacements, phase portraits, and spectrum 54
4.18 Linear model results ($T = 5.8$ s, $B_{PTO} = 10\,\mathrm{kNs/m}$): displacement, phase portrait, and spectrum 54
4.19 Sphere CWR with NSMc: bi-stable configuration ($H = 1.0$ m, $B_{PTO} = 30\,\mathrm{kNs/m}$) 55
4.20 Analytical nonlinear model results ($H = 1.0$ m, $T = 3.1$ s, $B_{PTO} = 30\,\mathrm{kNs/m}$): displacements, phase portraits, and spectrum 55
4.21 Analytical nonlinear model results ($H = 1.0$ m, $T = 10.1$ s, $B_{PTO} = 30\,\mathrm{kNs/m}$): displacements, phase portraits, and spectrum 56
4.22 Sphere CWR with NSMc: bi-stable configuration ($H = 2.0$ m, $B_{PTO} = 30\,\mathrm{kNs/m}$) 56
4.23 Analytical nonlinear model results ($H = 2.0$ m, $T = 4.9$ s, $B_{PTO} = 30\,\mathrm{kNs/m}$): displacements, phase portraits, and spectrum 56
4.24 Analytical nonlinear model results ($H = 2.0$ m, $T = 10.1$ s, $B_{PTO} = 30\,\mathrm{kNs/m}$): displacements, phase portraits, and spectrum 57
4.25 Sphere CWR with NSMc: QZS configuration ($H = 1.0$ m, $B_{PTO} = 10\,\mathrm{kNs/m}$) 58
4.26 Analytical nonlinear model results ($H = 1.0$ m, $T = 4.9$ s, $B_{PTO} = 10\,\mathrm{kNs/m}$): displacements, phase portraits, and spectrum 58
4.27 Analytical nonlinear model results ($H = 1.0$ m, $T = 6.1$ s, $B_{PTO} = 10\,\mathrm{kNs/m}$): displacement, phase portrait, and spectrum 59
4.28 Analytical nonlinear model results ($H = 1.0$ m, $T = 8.1$ s, $B_{PTO} = 10\,\mathrm{kNs/m}$): displacement, phase portrait, and spectrum 59
4.29 Sphere CWR with NSMc: QZS configuration ($H = 2.0$ m, $B_{PTO} = 10\,\mathrm{kNs/m}$) 59
4.30 Analytical nonlinear approach results ($H = 2.0\,\mathrm{m}$, $T = 4.9\,\mathrm{s}$, $B_{PTO} = 10\,\mathrm{kNs/m}$): displacement, phase portrait and spectrum 60
4.31 Sphere CWR with NSMc: QZS configuration ($H = 1.0\,\mathrm{m}$) 60

4.32 Sphere CWR with NSMc: QZS configuration ($H = 2.0$ m) 61
4.33 NSMc effects on the peak CWR and period for different wave heights: QZS configuration 61
4.34 Sphere CWR with NSMc: mono-stable configuration I ($H = 1.0$ m) . 62
4.35 Sphere CWR with NSMc: mono-stable configuration II ($H = 1.0$ m) . 62

5.1 Irregular wave spectrum and wave elevation ($H_S = 2.5$ m, $T_P = 8.0$ s) 66
5.2 Convergence analysis of the simulation length (t_S) for sea state: $S_P = 0.025$, $T_P = 4.0,\ 8.0,\ 12.0$ s 68
5.3 Linear and nonlinear models: CWR for wave steepness $S_P = 0.010$ . . 68
5.4 Linear and nonlinear models: CWR for wave steepness $S_P = 0.018$ . . 69
5.5 Linear and nonlinear models: CWR for wave steepness $S_P = 0.025$ . . 69
5.6 Meshing and analytical nonlinear models: mean power comparison . . 70
5.7 Meshing and analytical nonlinear models: displacement and amplitude spectrum($S_P = 0.025$, $T_P = 5.0\ s$) 70
5.8 Meshing and analytical nonlinear models: displacement and amplitude spectrum ($S_P = 0.025$, $T_P = 12.0\ s$) 71
5.9 Linear, meshing and analytical nonlinear models: wave excitation force ($S_P = 0.025$, $T_P = 5.0\ s$) 71
5.10 Linear, meshing and analytical nonlinear models: wave excitation force ($S_P = 0.025$, $T_P = 12.0\ s$) 71
5.11 Sphere CWR with NSMc: bi-stable configuration ($\alpha = 1.0$, $\gamma = 0.4$, $L = 2.0$ m) for sea state: $S_P = 0.025$, $T_P = 4.0,\ 8.0,\ 12.0$ s 72
5.12 Convergence analysis of the simulation length (t_S) with QZS NSMc ($\alpha = 1.0$, $\gamma = 0.5$, $L = 2.0$ m) for sea states: $S_P = 0.025$, $T_P = 4.0,\ 8.0,\ 12.0$ s 73
5.13 Convergence analysis of the simulation length (t_S) with mono-stable NSMc ($\alpha = 1.0$, $\gamma = 0.6$, $L = 2.0$ m) for sea states: $S_P = 0.025$, $T_P = 4.0,\ 8.0,\ 12.0$ s 73
5.14 Case I and Case II comparisons: QZS and mono-stable configurations 74
5.15 Schematic and dimensions of mechanical compression springs 75
5.16 NSMc feasible regions 77
5.17 AEP: sphere buoy with NSMc1 ($n = 6$) in the nearshore region of Rio de Janeiro 80
5.18 AEP percentage increase: sphere buoy with NSMc1 81
5.19 AEP: sphere buoy with NSMc3 ($n = 6$) in the nearshore region of Rio de Janeiro 82
5.20 AEP percentage increase: sphere buoy with NSMc3 83

6.1 Schematic view of NSS with pneumatic cylinders (NSPn) 85

6.2 P/P_0 patterns for different γ values ($L = 2.5$ m) 87
6.3 Pneumatic cylinder schematic view 87
6.4 Hydrostatic force and NSPn force ($\alpha = 1.0$, $\gamma = 1.0$, $L = 2.5$ m) . . . 88
6.5 Sphere static restoring force with NSPn ($L = 2.5$ m) 89
6.6 Sphere potential energy with NSPn ($L = 2.5$ m) 89
6.7 CWR comparisons between linear and nonlinear models ($H = 1.0$ m) 91
6.8 CWR with bi-stable configuration ($\alpha = 0.8, \gamma = 1.0, L = 2.5$ m) using linear approach 92
6.9 CWR with bi-stable configuration ($\alpha = 0.8, \gamma = 1.0, L = 2.5$ m) using analytical nonlinear approach 93
6.10 Convergence analysis of the simulation length (t_S) with QZS configuration ($\alpha = 1.0$, $\gamma = 1.0$, $L = 2.5$ m) for sea states: $S_P = 0.025$, $T_P = 4.0,\ 8.0,\ 12.0$ s 93
6.11 Convergence analysis on the simulation length (t_S) with mono-stable configuration ($\alpha = 1.2$, $\gamma = 1.0$, $L = 2.5$m) for sea states: $S_P = 0.025$, $T_P = 4.0,\ 8.0,\ 12.0$ s 94
6.12 NSPn feasible regions 95
6.13 AEP: sphere buoy with NSPn1 ($n = 4$) in the nearshore region of Rio de Janeiro 96
6.14 AEP percentage increase: sphere buoy with NSPn1 97
6.15 AEP: sphere buoy with NSPn3 ($n = 4$) in the nearshore region of Rio de Janeiro 98
6.16 AEP percentage increase: sphere buoy with NSPn3 99
6.17 CWR: sphere buoy with NSPn ($\gamma = 1.0$, $L = 2.5$ m and $n = 4$) for different sea states 100
6.18 CWR: sphere buoy with NSPn ($\alpha = 1.0$, $L = 2.5$ m and $n = 4$) for different sea states 101
6.19 CWR: sphere buoy with NSPn ($\alpha = 2.0$, $L = 2.5$ m and $n = 4$) for different sea states 101
6.20 C_d influence on AEP ($L = 2.5$ m, $n = 4$) 102
6.21 LnMd CWR using linear and nonlinear models ($H = 1.0,\ 2.0$ m) . . 103
6.22 LtCt CWR using linear and nonlinear models ($H = 1.0,\ 2.0$ m) 104
6.23 Optimal CWR and LD for different wave conditions 105
6.24 Peak period comparisons of different models in regular wave conditions 105
6.25 Peak CWR comparisons of different models in regular wave conditions 106
6.26 AEPs for four cases 107
6.27 Ratio of peak power to mean power for four cases 108

List of Tables

3.1 Analytical expressions of the nonlinear Froude-Krylov force for sphere 29
3.2 Nonlinear models' normalization CPU time 29
3.3 Regular wave conditions and optimal PTO damping 34
3.4 Mean power with irregular wave conditions 36
3.5 Irregular sea states and PTO damping 37

4.1 R^2 of hydrodynamic coefficients approximations 46
4.2 Regular wave conditions 48

5.1 Irregular wave conditions 66
5.2 Polynomial fittings of $J_0(kR\sqrt{1-x^2})$ and e^{kRx} 67
5.3 Mechanical compression spring parameters 75
5.4 Sea states selected in the nearshore region of Rio de Janeiro 79
5.5 AEP: sphere buoy with NSMc1 (LnMd1, $\text{AEP}_0 = 62.25\,\text{MWh}$) 81
5.6 AEP: sphere buoy with NSMc3 (LnMd3, $\text{AEP}_0 = 60.82\,\text{MWh}$) 82

6.1 NSPn main parameters 94
6.2 AEP: sphere buoy with NSPn1 (LnMd1, $\text{AEP}_0 = 62.25\,\text{MWh}$) 97
6.3 AEP: sphere buoy with NSPn3 (LnMd3, $\text{AEP}_0 = 60.82\,\text{MWh}$) 98
6.4 NSPn configurations 102

List of Symbols

$A(\omega)$	added mass, p. 18
A_d	projection area of instantaneous wetted surface onto waterplane, p. 30
$B(\omega)$	radiation damping, p. 18
B_{PTO}	linear PTO damping, p. 31
C_d	drag coefficient, p. 30
C_{WL}	linear hydrostatic restoring coefficient, p. 18
C_γ	coefficient of the geometry ratio to the critical value, p. 43
E	energy of the waves per unit area, p. 31
H	wave height, p. 9
H_S	significant wave height, p. 9
J	energy per unit time and unit width of the wave front, p. 31
$K_{\mathrm{I}}(t)$	radiation impulse response function, p. 18
R^2	coefficient of determination, p. 45
S	wave steepness, p. 47
S_P	average wave steepness, p. 65
$S_\zeta(\omega)$	wave power spectral density, p. 32
T	wave period, p. 8
T_L	latching duration, p. 8
T_P	peak period, p. 8
T_c	characteristic period, p. 8

T_e	energy period, p. 8
T_n	natural period, p. 8
T_{01}	mean period, p. 8
α	stiffness ratio, p. 41
$\ddot{z}(t)$	buoy vertical acceleration, p. 17
$\dot{z}(t)$	buoy vertical velocity, p. 18
γ	geometry ratio, p. 41
γ_{cr}	critical geometry ratio, p. 43
c_g	wave group velocity, p. 31
e_{NSMc}	potential energy of NSMc, p. 41
e_{NSPn}	potential energy of NSPn, p. 88
$f_{\mathrm{g}}(t)$	gravity force, p. 17
f_{D}	diffraction force, p. 19
f_{FK}	Froude-Krylov force, p. 19
f_{I}	incident wave force, p. 19
f_{NSMc}	NSMc restoring force, p. 40
f_{NSPn}	restoring force of NSPn, p. 85
$f_{\mathrm{PTO}}(t)$	reaction force from PTO system, p. 18
$f_{\mathrm{b}}(t)$	buoyancy force, p. 18
$f_{\mathrm{drag}}(t)$	drag force, p. 18
$f_{\mathrm{hydro}}(t)$	hydro-mechanic reaction force, p. 17
f_{h}	hydrostatic restoring force, p. 18
$f_{\mathrm{mach}}(t)$	machinery force, p. 17
$f_{\mathrm{rad}}(t)$	radiation force, p. 18
$f_{\mathrm{total}}(t)$	vertical external force acting on the buoy, p. 17

$f_{\mathrm{w}}(t)$	wave excitation force, p. 18
m	buoy mass, p. 17
m_n	the nth order moment of spectrum, p. 32
z_{f0}	NSMc displacement limit, p. 40

List of Abbreviations

AAP	Annual Average Absorbed Power, p. 36
AEP	Annual Energy Production, p. 6
BEM	Boundary Element Method, p. 18
CDOF	Compressible Degree of Freedom, p. 15
COV	Coefficient of Variation, p. 67
CWR	Capture Width Ratio, p. 31
DFO	Derivative-Free Optimization, p. 9
EOM	Equation of Motion, p. 17
FFT	Fast Fourier Transform, p. 49
HNS	Hydrodynamic Negative Stiffness, p. 14
IEA	International Energy Agency, p. 6
IVV	Immersed Varying Volume, p. 15
MPC	Model Predictive Control, p. 3
NSMc	NSS with mechanical compression springs, p. 6
NSPn	NSS with pneumatic cylinders, p. 6
NSS	Nonlinear Stiffness System, p. 4
OB	Oscillating-Body System, p. 2
OES	Ocean Energy Systems, p. 6
OWC	Oscillating Water Column, p. 2
PA	Point Absorber, p. 2

PF	Potential Flow, p. 18
PID	Proportion Integration Differentiation, p. 3
PI	Proportion Integration, p. 3
PSD	Power Spectrum Density, p. 66
PTO	Power Take-Off, p. 18
PTO	Power Take-Off system, p. 2
QZS	Quasi-Zero Stiffness, p. 43
RAO	Reponse Amplitude Operator, p. 34
RL	Reinforcement Learning, p. 3
WEC	Wave Energy Converter, p. 2

Chapter 1

Introduction

1.1 Overview

In 2018, the world electricity consumption was rated at 22,964 TWh with production reaching 26,590 TWh. In the global power generation matrix, since the end of 2000, the share of renewable energy sources has increased from 0.8% to 25.60%. The contribution from wind and solar energy sources has reached 7.47%, mostly due to the dramatic and continuous fall of their costs over recent years [1].

Ocean waves also can be thought, as a generous, sustainable and clean source of energy. They feature even higher density than wind and solar energies, and contain a tremendous amount of potential. The theoretical annual wave energy potential is estimated at around 29,500 TWh, even if one excludes regions where wave energy density is lower than 5 kW/m [2].

Nevertheless, the present research and development stage still cannot be considered sufficiently mature, as the technical potential related to the ocean wave energy is rather small – only about 146 TWh. It means that only almost 0.5% of the theoretical potential can be extracted from areas near coastlines with wave climate $> 30\,\mathrm{kW/m}$ and, also due to technological bottlenecks, wave energy converters still operate below 40% operational efficiency [3, 4].

In such a context, the wave energy conversion technology still presents great potential for possible developments to be worked on, looking forward to innovative and competitive solutions still to come.

Due to its location – in the ocean – wave energy conversion presents difficulties but also some unique advantages. One of these positive characteristics would be that it is suitable for power supplying to remote islands. Furthermore, it would be a rather promising choice as potential power supplies for many applications in the offshore industry, e.g., complementary power supplies in the oil&gas offshore industry and fish farm industry.

In the literature, there are many different types and concepts of Wave Energy Converters – WEC. Typically, based on its geometry, the WEC adopts the following classification: Terminator, Attenuator and Point Absorber (PA) [5].

On the other hand, depending on its physical concept, they can be classified as Oscillating Water Column (OWC), Oscillating-Body System(OB) and Overtopping Device [2]. In Figure 1.1, the schematic conceptual classification of WECs are described but not necessarily limited to the above-mentioned situations.

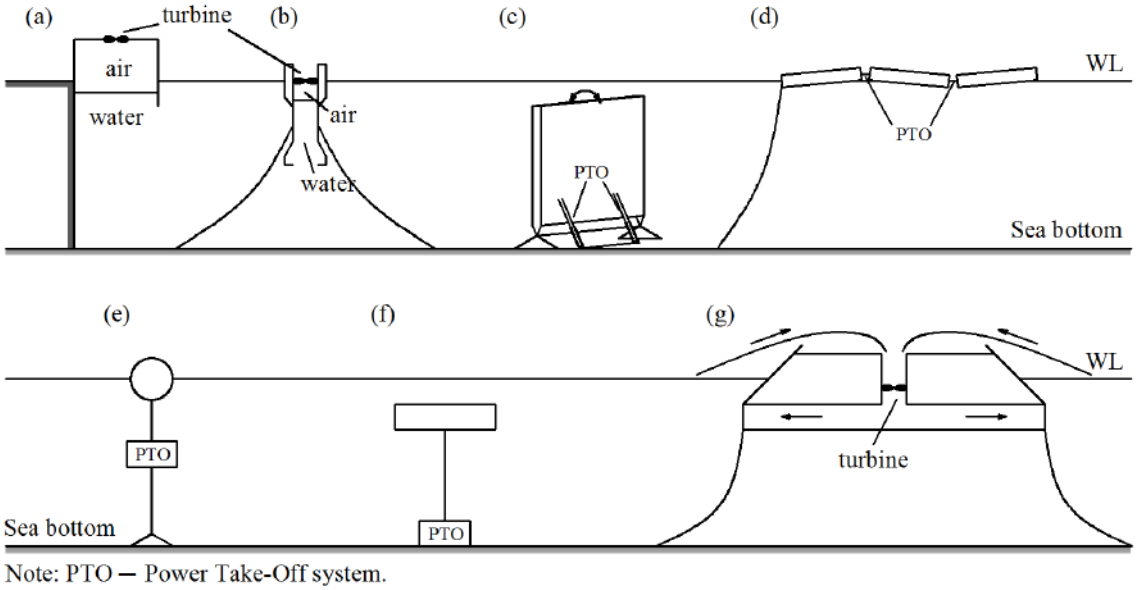

Figure 1.1: Schematic conceptual classification of wave energy converters (adapted from [6])

(a) Fixed OWC; (b) Floating OWC; (c) Terminator; (d) Attenuator;
(e) Point Absorber; (f) Submerged Pressure Differential; (g) Overtopping Device.

In the last two decades, the PA type WEC has been attracting a great deal of attention from the wave energy technological community. The simplicity of its geometry and mechanical apparatus, and relatively small dimensions lead to lower investments and maintenance costs. Further, the vertical axisymmetry allows for extracting energy from any wave propagation direction. Moreover, small bodies are also more convenient to work in arrays, as used in offshore parks. Such characteristics indicate PAs as a highly promising alternative to be considered as a competitive commercial solution to the electricity market in the coming future.

1.2 Motivation and objectives

Due to its small characteristic length, the PA's operational bandwidth is much narrower than other WEC concepts (e.g., terminator and attenuator devices). In that case, PA will be able to extract a significant amount of wave energy only from

wave components lying within a quite narrow band close to the resonance. Therefore, if its natural frequency is out of the range of the predominant sea wave frequency, it will cause an abrupt drop in efficiency. By considering real sea conditions, typical PA tends to operate mostly out of the resonance conditions.

To overcome the aforementioned costly drawbacks, one possible approach is to work with optimal control or sub-optimal control if the fully optimal control is not attainable [7]. The complex conjugate control [8], damping control [9–11], latching control [12–17], Model Predictive Control (MPC)/MPC-like control [7, 10, 18–22] and Proportion Integration (PI)/Proportion Integration Differentiation (PID) control [23–26], Reinforcement Learning (RL) [27, 28] represent some of the most widely studied schemes.

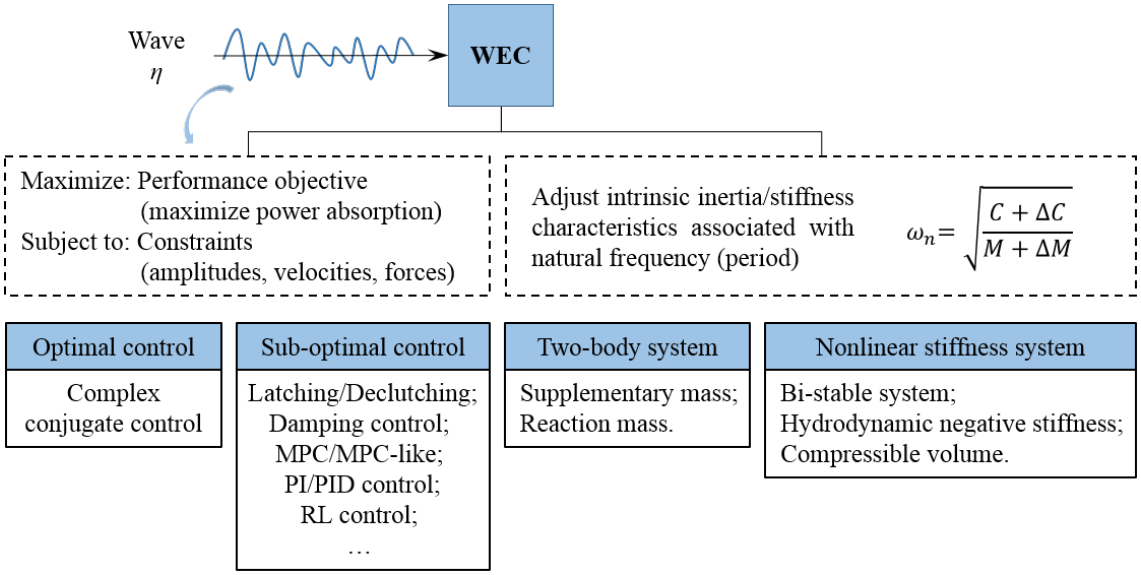

Figure 1.2: Possible approaches to improve wave energy conversion

Some of the control strategies, such as complex conjugate control, MPC/MPC-like control, PI/PID control, and RL, require an accurate prediction of wave excitation force which is one major obstacle for real applications. In addition, Bi-directional reactive power flow increases the complexity of the PTO system, as well as the cost. To avoid such difficulties, the focus has been transferred to the control strategy based on the non-reactive approach [29].

In the case of damping control [8], selecting the positive damping, no matter it is constant [9, 10] or time-varying [11], the reactive power flow disappears. One pre-calculates the optimal damping according to wave conditions and then updates online based on the estimation of wave conditions [25]. Thus such a simple approach is usually merged with other strategies to investigate the PTO damping influence for better integration. For instance, when applying latching control, the PTO damping should be updated online based on the optimal damping look-up

table pre-calculated.

Latching control does not feature reactive power flow inherently [29]. However, though the non-predictive approach [13–15] eliminates the demand of wave excitation force prediction, the determination of proper latching duration that affects the performance of latching control strictly, still requires the estimation of the deployment wave climate.

Another possible alternative approach changes the intrinsic inertial or stiffness characteristics that are associated with the natural frequency (period) of the system. A two-body system [30, 31] or a nonlinear stiffness system (NSS) [32, 33] can achieve such a goal. Among other possible engineering applications, the NSS has been widely applied in the vibration isolation problem and vibration energy harvesting, and has started attracting attention as a promising concept to be applied as a feasible, efficient, and simple solution for wave energy conversion [34, 35], while most of the two-body systems demand large supplement mass which inherently increases the cost of WEC construction.

Based on these above observations, the present thesis focuses on improving the understanding and evaluating the application of NSS concept on wave energy conversion.The main objectives of the investigations presented in the thesis may be summarized as:

- To derive the accurate and efficient nonlinear Froude-Krylov force model in analytical approach;
- To investigate novel characteristics of NSS concept with nonlinear Froude-Krylov force model;
- To establish the NSS practical constraint conditions;
- To investigate the alternative NSS solution featuring fewer constraints.

1.3 Outline of the thesis

To comply with the objectives listed in Section 1.2, the thesis content is structured as follows:

Chapter 2 – Literature review

A comprehensive review of the main aspects related to the novel approach to improve the performance of PA type WEC aims at presenting some of its historical backgrounds and recent outcomes including discussions about the reactive and non-reactive control strategies, and the approaches that can change the intrinsic inertial or stiffness characteristics associated with the natural frequency (period) of the dynamic system.

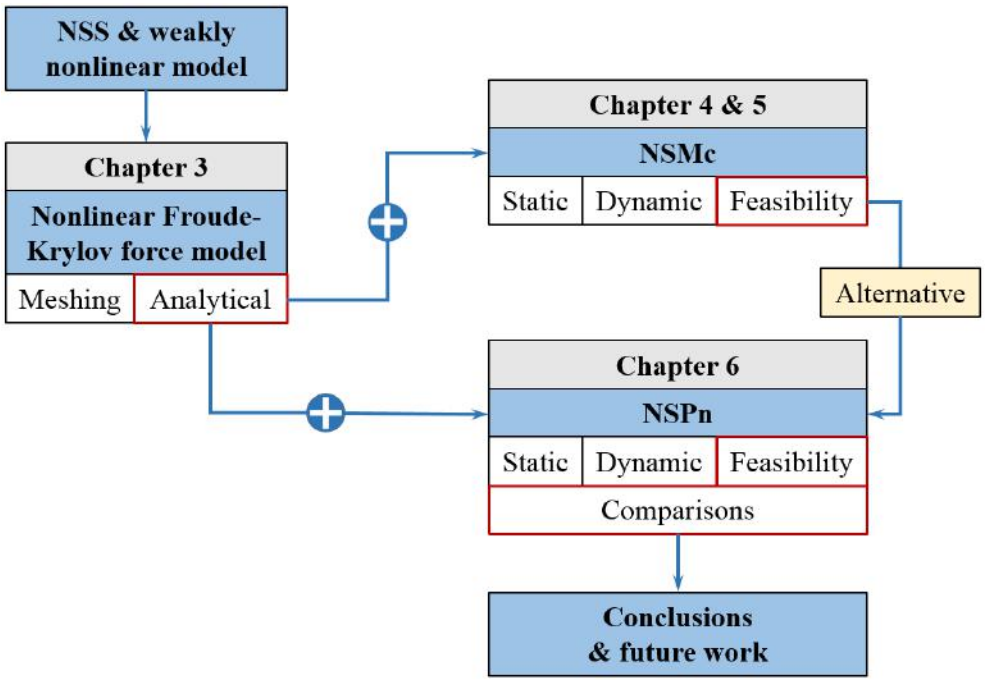

Figure 1.3: Thesis organization

Especially, the non-reactive latching control alternative deserves some deeper attention in the review since it is chosen to be compared with the following mentioned NSS due to its simple logic and high efficiency.

NSS applications in vibration isolation, vibration energy harvesting and so on bring some inspirations to be initially considered into wave energy conversion. But some other relevant researches on NSS engineering applications still need to be done.

Some authors have discussed the weakly nonlinear Froude-Krylov force model, provided by the non-uniform waterplane area of the PA buoy. Such a nonlinear characteristic will be investigated together with the NSS in this thesis.

Chapter 3 – Mathematical model

The fundamental mathematical model to deal with the ocean wave excited problems is based on Newton's second law. The well-known linear model adopts the linear potential flow theory to evaluate the hydrodynamic forces, and usually simplifies the PTO force with a linear damping term, where the state-space model is utilized to approximate the convolution integral that appears in the radiation force calculation.

In the weakly nonlinear model, only the nonlinearity of Froude-Krylov is considered due to the non-uniform waterplane area of the sphere through both the direct meshing and analytical approaches. In addition, the analytical approach is further improved to handle the regular wave and irregular wave situations more accurately and efficiently, especially for the latter one. Finally, the drag force correction is also mentioned as its effect deserves further investigation when the motion response is

amplified by NSS.

To verify the code set up based on the above theory, a code-to-code verification compares results to those from the International Energy Agency (IEA) Ocean Energy Systems (OES) Task 10 project [36], including the free-decay tests, regular wave situations, and irregular wave situations.

Chapter 4 – Nonlinear stiffness system in WEC

In this chapter, the mathematical model of NSS with mechanical compression springs (NSMc) is set up. The static analysis helps to better understand the NSMc system.

In the dynamic analysis, both situations with/without NSMc in linear and nonlinear approaches first validate the mathematical model. Then the unique motion characteristics of a sphere with NSMc under the regular wave conditions, allow for identifying the distinct motion behaviors. In addition, Chapter 4 simultaneously explores the influence of some relevant factors on motion behavior and power absorption.

Chapter 5 – NSMc in WEC: practical considerations

Continually, this chapter concentrates the investigation on the NSMc practical application. Thus it discusses the NSMc performance in irregular wave conditions, with the necessary validation first.

According to the design process of mechanical compression springs, the practical constraint conditions in designing the NSMc system are proposed. Hereafter, the theoretical annual energy production (AEP) in a given sea site is evaluated within the feasible NSMc configurations.

Chapter 6 – Alternative NSS in WEC

To overcome the strict practical limitations imposed by the mechanical characteristics of springs on the NSMc performance, Chapter 6 discusses an alternative NSS with pneumatic cylinders (NSPn) and sets up the corresponding novel model.

Following the static and dynamic analysis of the novel system, this chapter explores the practical feasibility of the pneumatic cylinder solution, which can explain the advantage of NSPn relative to NSMc. The further performance analysis on the influencing factors is conducted, together with the drag correction.

Finally, the chapter performs comprehensive comparisons between the lathing control method with constant latching duration and different NSPn configurations to evaluate their functions on improving the wave energy conversion.

Chapter 7 – Conclusions and future work

The final chapter resumes the main conclusions drawn during the thesis preparation and points out some meaningful work that exceeds its scope, indicating them as possible future investigations.

Chapter 2

Literature Review

An extensive and fruitful review of the control strategies for improving the wave energy conversion of WECs can be found in [7, 8, 18, 22, 37, 38]. Most of the optimal and sub-optimal control strategies depend on the accurate wave information, as well as generate reactive power flow in the PTO system. One exception is the latching/declutching control, which is non-reactive inherently [29].

Except for the aforementioned schemes, an alternative approach could be obtained by adjusting the intrinsic inertial or stiffness characteristics associated with the natural frequency (period) of the dynamic system. In a two-body system, a supplementary mass may reduce the natural frequency [30, 31], while the two-degree-of-freedom motion of the WEC buoy and the reaction mass may broaden the frequency range of the response [39–41] due to multiple resonance states. An additional bi-table system featuring negative stiffness reduces the natural frequency in a distinctive way [32, 42]. In the same way, hydrodynamic negative stiffness and compressible volume concepts can also decrease the resonance frequency[43–47].

The consequent discussions will cover the non-reactive latching and declutching control, two-body system and nonlinear stiffness system as their relatively simple logics do not require complex optimization computation and no reactive PTO flow exists.

2.1 Latching and declutching control

Latching control, as proposed originally by Budal and Falnes [12], has been applied to the pioneering wave-power buoy project in the 1980s [48, 49]. It works as a kind of discrete control strategy, therefore, different from the reactive control, which works as a continuous process. As shown in Figure 2.1, at the time t_1 when the buoy reaches its upmost position and velocity zero, a clamping mechanism keeps the buoy position fixed. Then it releases the buoy after a certain latching duration T_L at the time t_2. When it reaches the lowest position at the time t_3, the clamping

mechanism works again. In this case, the buoy velocity has always the same sign or in phase with the wave excitation force, implying that power will be transferred from the wave to the buoy. Hereafter, latching control is referred to as phase control.

To achieve the velocity and wave excitation force synchronization, the latching duration T_L is one key factor to determine the releasing time instance – t_2 or t_4. In regular wave conditions, the constant latching duration [15] can be defined as,

$$T_L = \frac{T - T_n}{2} \tag{2.1}$$

where: T – wave period;

T_n – oscillating buoy natural period.

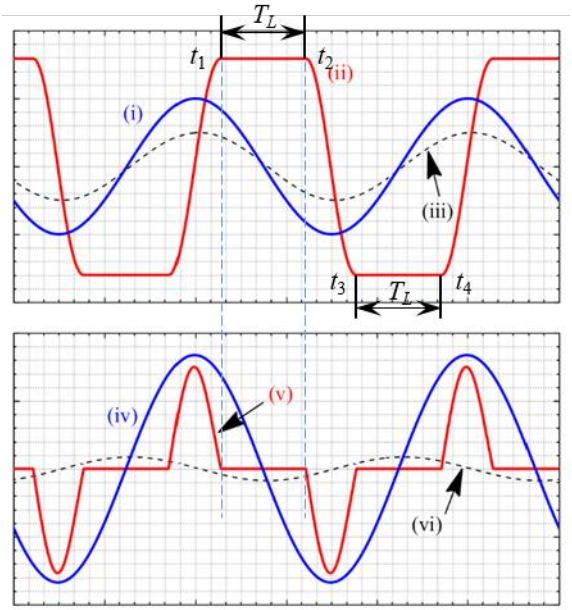

Figure 2.1: Illustration of latching control with constant latching duration

(i): wave elevation; (ii): displacement with latching; (iii): displacement without latching; (iv) wave excitation force; (v): velocity with latching; (vi): velocity without latching.

Note that, the latching control method works only if wave period (T) is longer than the buoy natural period (T_n). In irregular wave conditions, Sheng et al. [15] have proposed a simple expression of T_L through using the characteristic period T_c. It may be the energy period (T_e), mean wave period (T_{01}) or peak period (T_P).

$$T_L = \frac{T_c - T_n}{2} \tag{2.2}$$

Peñalba Retes et al. [50] have found that the constant latching duration strategy might not be the best strategy when using the weakly nonlinear Froude-Krylov force model. They consequently defined an adaptive latching strategy, allowing for adaptive changes in the latching duration to obtain the largest motion amplitude,

regardless of the hydrodynamic model (linear or nonlinear).

Alternatively, Falcão [13] proposed one threshold latching control and applied it to a PA with hydraulic PTO system. The PA remains fixed after its velocity reaches zero until the hydrodynamic force exceeds a pre-set threshold value. Such techniques do not require any prediction of wave information but utilize only the measurement of wave elevation as controller input. Then, Lopes et al. [14] transferred the force threshold into the wave elevation threshold (ζ_{th}) and adopted this type of control strategy to conduct experimental work featuring an OWC. In regular wave conditions, the wave elevation threshold latching is equivalent to the aforementioned constant duration latching. For the irregular wave, the threshold is calculated in the same way as for the regular wave using the same energy period and an equivalent power level. The expression of ζ_{th} is given by,

$$\zeta_{th} = \begin{cases} \dfrac{H}{2}\sin\left[\dfrac{\pi}{2}(1-\dfrac{T_n}{T})\right] & \text{regular wave} \\ \dfrac{H_S}{2\sqrt{2}}\sin\left[\dfrac{\pi}{2}(1-\dfrac{T_n}{T_e})\right] & \text{irregular wave} \end{cases} \tag{2.3}$$

where: H – wave height of a regular wave;

H_S – significant wave height of an irregular wave.

Due to the randomness of wave elevations in irregular waves, two latching strategies behave differently. The power output depends only moderately on the threshold value and loading damping. Consequently, it makes the threshold unlatching strategy a promising candidate for the development of a simple and high-yield controller for latching control operation in real-sea conditions [14].

Besides the above non-predictive strategies, there are some other predictive approaches to conduct latching control. In such an approach, not only one powerful and accurate mechanical or electromagnetic clamping mechanism needs to execute the latching and releasing commands, but also it requires the prediction of wave excitation force. Budal and Falnes [48, 49] indicated that the unlatching should take place $T_n/4$ before the maximum force occurs. Thus, the wave should be predicted at least at time $T_n/4$ in advance. This prediction can be done by measuring the local wave pressure or by means of Kalman filter technique. According to the similar strategy of determining the unlatching time, Babarit et al. [16] proposed a predictive latching control aiming at keeping the velocity and excitation force in phase, together with the other two strategies – maximizing the power absorption and maximizing the heave amplitude. Feng and Kerrigan [51] proposed a latching control algorithm to maximize power absorption in irregular wave conditions using the Derivative-Free Optimization (DFO) method that featured relatively low computational burden and significant improvement in energy absorption. Their al-

gorithm considered two receding horizon closed-loop strategies: the non-predictive one took the past wave information to estimate the optimal latching duration; the predictive one defined the optimal time by predicting the future waves.

When applying the latching control on a two-body point absorber, Falcão et al. [52] found out that the substantial increase in the energy absorption of a single-body converter did not occur in the two-body buoy case, except for the very impractical large value of the mass of the submerged body against which the floater was reacting. The similar conclusion was also drawn by Eidsmoen [53].

In 2011, Todalshaug et al. [18] conducted comparisons of more real-time control strategies for a heaving buoy in a set of irregular wave conditions and addressed that though less power was produced, with latching control, the peak-to-average power ratio was less than half of that with the reactive control – MPC. In their earlier work [54], the comparisons in regular waves also depicted the similar result.

Besides the need for a very powerful mechanical or electromagnetic clamping mechanism, the predictive approach requires the prediction of wave excitation force.

On the contrary, declutching control is suitable for the case when the WEC resonant period is longer than the wave period. Babarit et al. [17] implemented the declutching control on a PA with hydraulic PTO system using a simple by-pass valve and draw the conclusion that declutching control can lead a higher energy absorption in both regular and irregular waves. However, as it is more common that the predominant wave period is longer than the PA type WEC natural period, the latching control is more widely implemented than the declutching control.

2.2 Two-body WEC

To avoid expensive and vulnerable control system and clamping mechanism, one alternative strategy would be a passive system to change the frequency response of the PA so as to be in resonance with the dominant sea states at the chosen location. According to the well-known un-damped natural frequency (ω_n) expression,

$$\omega_n = \sqrt{\frac{C}{m + m_a}} \tag{2.4}$$

where: C – system stiffness;

m, m_a – mass and added mass (system inertia).

one way of shifting the frequency response of the dynamic system is by increasing the inertia of the moving parts. Engström et al. [30] studied the influence of the submerged depth on the power capture as shown in Figure 2.2 (a). They found that in order to achieve good power absorption for a two-body system, the lower body should be placed at a sufficient depth. In that case, both the excitation force on

and radiation from the lower body are very low so that the lower body can act as a passive energy storage mechanism that adds additional inertia into the system. Using the Taguchi method, Al Shami et al. [31] distinguished the effects of seven different parameters and discovered that: (i) the shape (cylinder vs. sphere) of the lower body had the largest effect on both the power absorption and bandwidth; (ii) the volume of the lower body affected the resonant frequency most heavily. Thus, the lower body is the most important factor to improve the two-body WEC system performance.

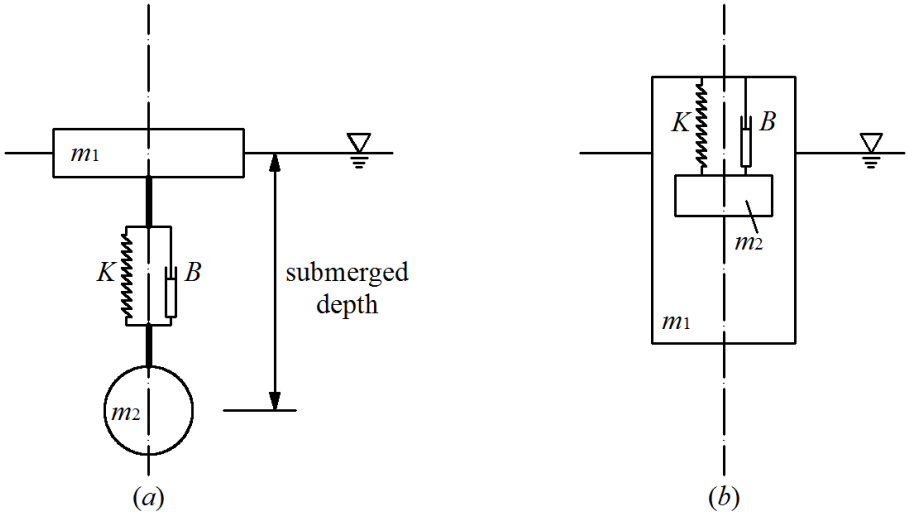

Figure 2.2: Schematics of two-body WECs

The other type of reaction mass strategy was investigated by Kode [39], French [40] and Chen et al. [41]. As shown in Figure 2.2 (b), only one body is floating in the water. Another reaction mass is placed inside and connected with the floating body through a spring and/or a damper. Owing to the coupled effects between the two sets of mass-spring-damper, the response of motions and power feature double response peaks. The corresponding resonance frequencies form a range covering each one of the single-body resonance frequencies. Herein, varying the internal mass and spring can broaden the bandwidth, and adjusting the damping can achieve the optimal power capture.

2.3 Nonlinear stiffness system

On the contrary to the shifting of the frequency response by changing the inertia of the moving buoy, another approach is to decrease the stiffness of the dynamic system by adding one "negative stiffness".

The bi-stable system is such a classical system that provides nonlinear restoring force through some special configurations of mechanical compression springs, pneu-

matic actuators, buckling beams, or magnets, etc. It exhibits two statically stable configurations and one unstable state. Sometimes it is also called by snap-through mechanism or negative stiffness system. In many engineering applications, the characteristic of snap-through from one equilibrium to another is a problem, because it may cause instability and affect the performance of the overall system. Recently, however, researchers have reconsidered it and started investigating the potential benefits related to the NSS, not limited to the bi-stable system [35].

Benefiting from the resonance frequency reduction, the bi-stable system has been widely applied in seismic protection of buildings [55, 56] and vibration isolation [57, 58]. On the other hand, when the excitation frequency is less than the natural frequency, the bi-stable system can assist the vibration energy harvester absorbing more power [59]. In addition, involving the nonlinear stiffness characteristic may broaden the frequency response bandwidth effectively which is beneficial for harvesting different types of excitations [34, 60]. Higher outputs can be obtained from a spring-assisted adaptive bi-stable energy harvester, compared to those from conventional bi-stable energy harvester, due to its unique adaptive potential characteristic [61].

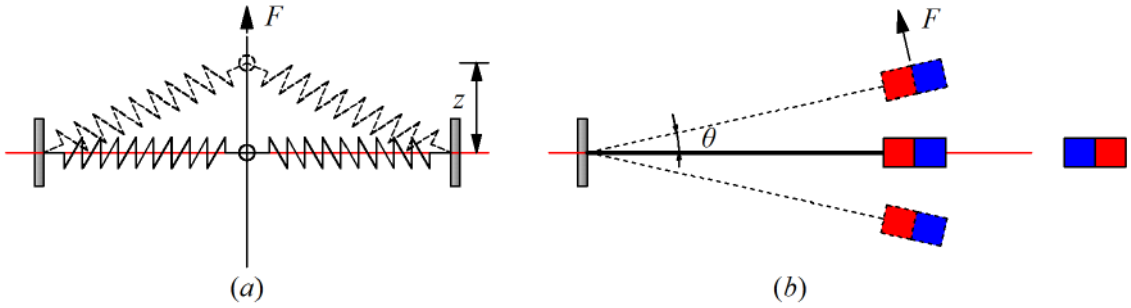

Figure 2.3: Schematics of NSS

Over recent years, NSS has also attracted increasing attention from researchers on wave energy conversion technology because its natural frequency-shifting characteristic may increase the efficiency of a PA type WEC with a lower natural period. The bandwidth broadening characteristic is particularly beneficial for the application in random sea conditions. Both numerical and experimental investigations have been carried out to explore the implementation of NSS in PA.

Zhang et al. [32, 62] proposed a nonlinear snap-through PTO system consisting of two symmetrically oblique springs and featuring a bi-stable mechanism. Through extensive analysis and comparisons in both regular and irregular waves, the authors have found that the nonlinear WEC could capture a larger amount of power for lower geometry parameter γ under low peak frequency condition. Moreover, the increase of wave amplitude contributed less to the power than for the linear WEC. However, one drawback of the conventional bi-stable mechanism is that it is difficult

to overcome the potential barrier under relatively small-amplitude wave excitations. Consequently, they continued to develop a novel adaptive bi-stable mechanism [63, 64] by adopting two additional auxiliary springs that could adjust the potential function automatically to lower the potential barrier near the unstable equilibrium position. Hence the "adaptive" feature helped to solve the low energy absorption problem of conventional bi-stable wave energy converter. In addition, the adaptive bi-stable WEC had a wider frequency bandwidth with suitable system parameters that could overcome the low-efficiency drawback of traditional linear PAs due to off-resonance operation in realistic sea states.

Almost in the same period, Todalshaug patented a wave energy converter with a negative stiffness device [33]. The device could feature either mechanical springs or pneumatic cylinders. The pneumatic configuration was then patented as a "WaveSpring" technique and used in the CorPower buoy prototype [65]. To verify such an innovative concept, the CorPower conducted a 1/16 scale model test [42]. The experimental results have shown that the WEC could be tuned to provide both resonant behavior and broad response bandwidth. Continually, they completed the prior dry testing and ocean deployment using a 1/2 scale WEC, through which the industrial solution of the "WaveSpring" concept was verified.

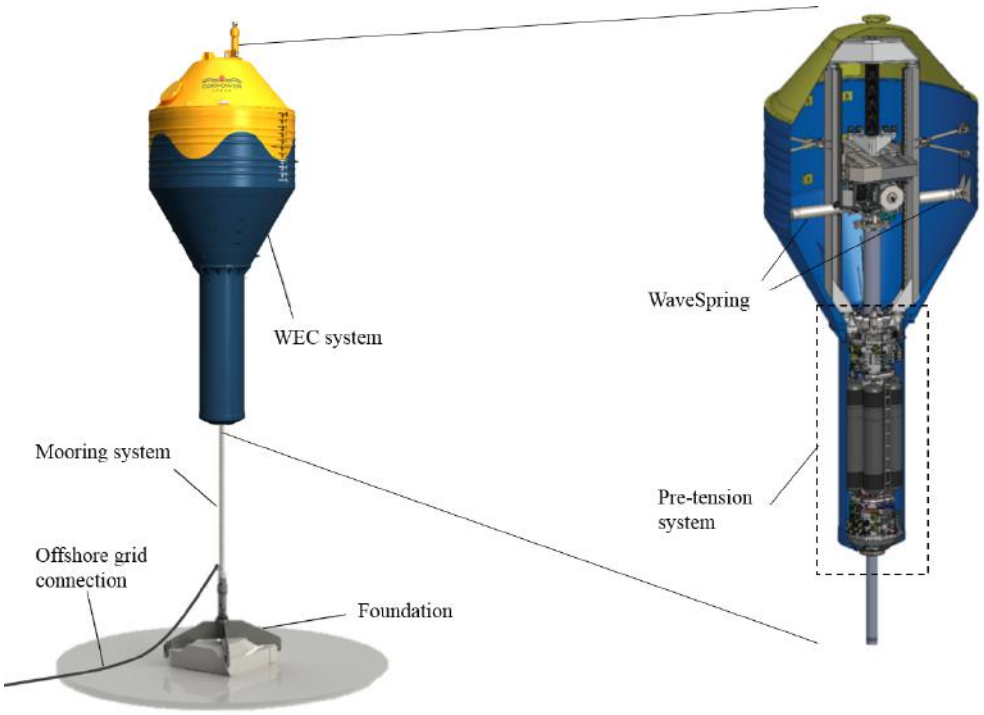

Figure 2.4: CorPower buoy (adapted from [65])

Since then, much research has extended the application of a bi-stable snap-through mechanism to the pitching and surging WECs [66–69]. Younesian and Alam [70], and Li et al. [71] adopted the application of a multi-stable mechanism

through more complex geometric configurations and demonstrated similar benefits on the wave energy conversion.

Through the above review of NSS implementations in WEC, it can be observed that all the concepts are still at an early stage of development: either under numerical simulation or small scale tests, except for the "WaveSpring" of CorPower buoy but without much published detail about its performance. Most of the applications feature mechanical compression springs. To gain more significant improvement for WEC with NSS, the geometry parameter γ in terms of spring lengths should be assigned as a quite small value, as mentioned by Zhang et al. [32, 62], requiring both long free length (exceeding several meters) and extremely large compressible length. It is difficult to satisfy such geometry characteristics in the practical design of mechanical compression springs, not to mention that high stiffness should be satisfied simultaneously. Other factors, such as the buckling due to longer lengths and fatigue load due to wave excitations, may also introduce some negative effects on the NSS performance with mechanical compression springs. Theoretically, it would be possible to design even one but the dimensions (e.g., nominal diameter, wire diameter, etc.) and mass would be too big, scaling up the investment and installation costs. As shown in [69], there exists a successful implementation, of an 1/20 model scale, but in the prototype scale, the corresponding stiffness is not feasible. It is difficult to find suitable springs in the prototype scale. Such a practical limitation gives grounds for the necessity to build up a scientific methodology to identify the restrictions and propose the potential solutions for the implementation of NSS.

Within the author's knowledge, there has not existed any research featuring the feasibility of NSS application in WEC, especially considering large scale devices. The present thesis focuses on such a subject, pursuing an engineering approach to explore the benefits and evaluate NSS performance in ocean wave energy conversion.

There have been studies addressing the replacement of mechanical springs for the application of magnets to play the role of the bi-stable mechanism – see Harne et al. [72], Xiao et al. [73], and Zhang et al. [74]. An alternative multi-stable chain concept was developed for a mobile WEC with a small dimension compared with the dimension of a conventional WEC deployed in the ocean [72]. Considering the interaction between the two magnets, it weakens dramatically when their distance apart is large. The effective stroke may be restricted seriously by the magnetizations and magnets dimensions.

Unlike the mechanical springs, pneumatic cylinders or magnet arrangements, the WETFEET project [43–45]: features another alternative, namely, negative stiffness concepts applied on the OWC spar buoys:

- Hydrodynamic Negative Stiffness (HNS);

- Immersed Varying Volume (IVV).

Instead of controlling the PTO mechanism, these alternative methods act directly on the hydrodynamic properties of the buoy. For instance, the HNS method applied on the floating OWC involves widening the floater internal chamber, and filling the space with seawater on the downward cycle, and transferring the water back to the sea on the upward cycle. By doing so, the buoyancy is reduced along the downward cycle because less seawater is displaced, and increased on the upward cycle.

A similar compressible volume concept may also feature lower stiffness on a rigid body, as proposed by Kurniawan et al. [46, 47] – Compressible Degree Of Freedom (CDOF), which features a lower stiffness than a rigid body. However, the auxiliary compressible volume storage units would increase the CAPEX and OPEX costs, potentially reducing the aforementioned benefits gained by CDOF as mentioned by Bacelli et al. [75].

Inspired by the above concepts associated with the hydrodynamic characteristics of the WEC, a PA with a non-uniform waterplane area, such as a sphere, is able to achieve the objective of changing the natural period directly, that deserves further investigation.

2.4 Nonlinear Froude-Krylov force

According to the idea of adopting a non-uniform waterplane PA to change the natural period of WEC, as inspired by the HNS and compressible volume concepts shown in the above review, the corresponding nonlinear hydrodynamic characteristics should then be considered carefully as well.

Gilloteaux et al. [76, 77] have applied the nonlinear Froude-Krylov force model to predict large-amplitude motion of a WEC through developing an automatic remeshing routine. The instantaneous wetted surface is represented by an appropriate number of panels. The instantaneous free surface and the new WEC position define the changing wetted surface at each time step. The wetted panels are updated simultaneously. Then Mérigaud et al. [78] used the same method to conduct the comparisons between the linear model and two nonlinear models. They concluded that there was a clear tendency showing that the linear model overestimated the buoy motion and, consequently, overestimated the power production. Simultaneously, the Froude-Krylov force was identified as the principal nonlinearity source.

Peñalba Retes et al. [50] simplified the nonlinear model, considering only the linear terms of the radiation and diffraction forces. They used the remeshing approach to calculate the instantaneous Froude-Krylov. The nonlinear effects were amplified if the control strategy was applied, especially, in the case of the buoy with

a non-uniform waterplane area. Moreover, nonlinearity also affects the design of the control strategy significantly, such as the latching control with constant latching duration.

Important to notice that the remeshing approach demands extremely high computational effort. The WEC-Sim [79], an open-source code for WEC simulations, utilizes a weakly nonlinear Froude-Krylov force model with a fine mesh prepared in advance, but the processing time is still considerable.

To overcome the meshing approach inefficiencies, Giorgi and Ringwood [80–83] came up with the analytical approach for some simple axisymmetric body, like sphere and cylinder, systematically. Cong et al. [84] derived the analytical expression of nonlinear Froude-Krylov force in finite water depth.

All the work above has been developed for regular wave conditions. In the irregular waves, the computation efforts also depend on the number of frequency components considered in the sea state representation. Usually, to generate one irregular wave record correctly, several hundred or more than one thousand frequencies are required. Thus, Mérigaud and Ringwood [85] used the Taylor expansion to separate the frequency-dependent terms from the displacement. it means that a significantly time-consuming calculation can be prepared in advance outside of the time updating loop

Practically, the Taylor series can only give an accurate approximation around the expansion point. Out of the range, the residual error will be quite large. Thus the analytical approach demands an accurate approximation method of some special functions, especially when the motion is large or the corresponding frequency is high. Such a subject is another focus of this thesis.

2.5 Summary

A comprehensive review of the approaches that can achieve the goal of increasing wave energy conversion efficiency discussed the relevant reactive and non-reactive control strategies and the methods of changing the intrinsic inertial or stiffness characteristics associated with the natural frequency (period) of the dynamic system. It highlights that the feasibility problem of the NSS concept deserves further investigation, as well as the proposal for better alternatives.

As one supplement of the NSS approach, the buoy with nonlinear hydrostatic stiffness due to its non-uniform waterplane area will be adopted according to the above investigation. The relevant subjects of the nonlinear Froude-Krylov force model in the numerical simulation were also indicated based on the review conducted in this chapter.

Chapter 3

Mathematical Model

This chapter introduces the fundamental mathematical model of the problem discussed in the thesis, including the linear model based on the linear potential flow theory adopting the Cummins equation [86], and the nonlinear model considering the Froude-Krylov force induced by the instantaneous wet surface. In addition, the external drag force incorporates some degree of correction.

An in-house code, developed to solve the above model, validates its results in comparisons with the results published by the International Energy Agency (IEA) Ocean Energy Systems (OES) Task 10 project [36]. The verification process includes different numerical evaluations, i.e., the heaving decay test, WEC response in regular wave conditions, and power absorption in irregular wave conditions.

3.1 Equation of motion

The single-degree-of-freedom equation of motion (EOM) of a floating buoy in waves is set up according to Newton's second law – Eq. 3.1:

$$m \cdot \ddot{z}(t) = f_{\text{total}}(t) \tag{3.1}$$

where: m – floating buoy mass;

$\ddot{z}(t)$ – buoy vertical acceleration at time instant t;

$f_{\text{total}}(t)$ – total vertical external force acting on the buoy.

In the wave energy application, the $f_{\text{total}}(t)$ usually consists of gravity force – f_{g}, hydro-mechanic reaction force – $f_{\text{hydro}}(t)$, and machinery force – $f_{\text{mach}}(t)$.

$$\begin{aligned} f_{\text{total}}(t) &= f_{\text{g}} + f_{\text{hydro}}(t) + f_{\text{mach}}(t) \\ &= f_{\text{g}} + f_{\text{b}}(t) + f_{\text{rad}}(t) + f_{\text{w}}(t) + f_{\text{drag}}(t) + f_{\text{PTO}}(t) \end{aligned} \tag{3.2}$$

where, $f_{\text{hydro}}(t)$ is the integral of fluid pressure on the wetted surface, including both

static and dynamic components. The static component indicates the buoyancy – $f_{\mathrm{b}}(t)$; the dynamic component can be decomposed into radiation force – $f_{\mathrm{rad}}(t)$ and wave excitation force – $f_{\mathrm{w}}(t)$.

The Potential Flow (PF) theory evaluates these force components and additional correction corporates the viscous drag effect. Such a correction may be reasonable, though viscous influences are not quite significant in some practical cases [87]. Morison equation[79, 88] is one alternative to calculate the drag force – $f_{\mathrm{drag}}(t)$.

$f_{\mathrm{mach}}(t)$ is predominantly associated with the reaction force from the so-called Power Take-Off (PTO) system – $f_{\mathrm{PTO}}(t)$. According to the different principles of the PTO system, its mathematical model may vary widely. Sometimes, if some control strategies are adopted to enhance the WEC's wave energy conversion performance, the corresponding acting force could be treated separately or incorporated into the $f_{\mathrm{PTO}}(t)$ accordingly.

3.1.1 Linear model

The well-known linear model gives an efficient approach to deal with the ocean wave excited problems, being largely discussed in the technical literature [26, 88, 89].

$$\begin{aligned} m \cdot \ddot{z}(t) &= f_{\mathrm{rad}}(t) + f_{\mathrm{h}}(t) + f_{\mathrm{w}}(t) + f_{\mathrm{PTO}}(t) \\ &= -A_{\infty} \cdot \ddot{z}(t) - \int_0^t K_I(t-\tau) \cdot \dot{z}(t) \cdot d\tau - C_{WL} \cdot z(t) + f_{\mathrm{w}}(t) + f_{\mathrm{PTO}}(t) \end{aligned} \tag{3.3}$$

where: A_{∞} – infinite-frequency added mass;

$K_I(t)$ – Radiation Impulse Response Function (RIRF) in time domain;

$\dot{z}(t)$ – buoy vertical velocity at time instant t;

$z(t)$ – buoy vertical displacement at time instant t;

C_{WL} – linear hydrostatic restoring coefficient.

The gravity force f_{g} and linear buoyancy force $f_{\mathrm{b}}(t)$ of buoy are the linear hydrostatic restoring force – $f_{\mathrm{h}}(t)$ components. In the "memory effect" term which appears in Cummins' equation [86], $K_{\mathrm{I}}(t)$ calculates the radiation force $f_{\mathrm{rad}}(t)$, that is related with the hydrodynamic coefficients – added mass $A(\omega)$ and radiation damping $B(\omega)$. The popular Boundary Element Method (BEM) [90–92] obtains $A(\omega)$ and $B(\omega)$. For some simple geometries, such as the sphere [93] and cylinder [94], some specific analytical approaches provide those hydrodynamic coefficients.

Due to the inefficiencies and inconveniences involved in the use of the direct integral method to calculate $K_{\mathrm{I}}(t)$ with $A(\omega)$ or/and $B(\omega)$, an alternative approach based on the state-space model [95, 96] provides a better choice.

The linear wave excitation force $f_{\mathrm{w}}(t)$ is separated into the incident wave component $f_{\mathrm{I}}(t)$, also named as Froude-Krylov force $f_{\mathrm{FK}}(t)$; and the part due to the diffraction wave – $f_{\mathrm{D}}(t)$.

The dynamic of WEC may incorporate different kinds of nonlinear effects, such as, from the buoy non-uniform waterplane area generating the nonlinear Froude-Krylov force; the nonlinear drag correction due to the viscous effect, and so on. This chapter focuses more on the nonlinear model as discussed in the following.

3.1.2 Nonlinear model

For the heave point absorber, one relevant nonlinear component comes from the Froude-Krylov effect [78]. The vertical sidewall and the fixed body assumptions used to calculate the Froude-Krylov effect are not suitable in some cases, for instance:

- buoy featuring non-uniform waterplane area;
- buoy response motion with large amplitude;
- under high wave steepness conditions.

The weakly nonlinear model, in the case of the Froude-Krylov force being the main component of the hydrodynamic force for a heaving PA [78], accounts only for the nonlinear Froude-Krylov force over the instantaneous wetted surface associated with the water surface elevation, body position, and geometry of the floating body. This section assumes that the nonlinear Froude-Krylov force consists of both nonlinear hydrostatic restoring force – $f_{\mathrm{FKst}}(t)$ and nonlinear dynamic part – $f_{\mathrm{FKdy}}(t)$. The remaining $f_{\mathrm{rad}}(t)$ and $f_{\mathrm{D}}(t)$ are still solved by the PF theory.

$$\begin{aligned} m \cdot \ddot{z}(t) &= f_{\mathrm{rad}}(t) + f_{\mathrm{h}}(t) + f_{\mathrm{w}}(t) + f_{\mathrm{PTO}}(t) + f_{\mathrm{drag}}(t) \\ &= -A_{\infty} \cdot \ddot{z}(t) - \int_0^t K_I(t-\tau) \cdot \dot{z}(t) \cdot d\tau + f_{\mathrm{D}}(t) + f_{\mathrm{PTO}}(t) \\ &\quad + f_{\mathrm{FKst}}(t) + f_{\mathrm{FKdy}}(t) + f_{\mathrm{drag}}(t) \end{aligned} \tag{3.4}$$

Nonlinear Froude-Krylov force

Two different approaches, i.e., meshing and analytical approaches may be applied in the nonlinear Froude-Krylov force calculation.

A. Meshing approach

The buoy surface is discretized with fine meshes. As the blue gridded region shown in Figure 3.1 (b), the instantaneous wetted surface $S(t)$ is the collection of meshes satisfying:

$$z_i(t) = z_{\text{cent}i} + z_{\text{g}}(t) \leq \eta(x_i; t) \tag{3.5}$$

where: $z_i(t)$ – the ith element vertical position;

$z_{\text{cent}i}$ – vertical coordinate of the ith element centroid of area on the mean wetted surface, as shown in Figure 3.1 (a);

$z_{\text{g}}(t)$ – buoy vertical displacement;

$\eta(x_i; t)$ – wave elevation at the ith element with the horizontal coordinate x_i with respect to the mean water level.

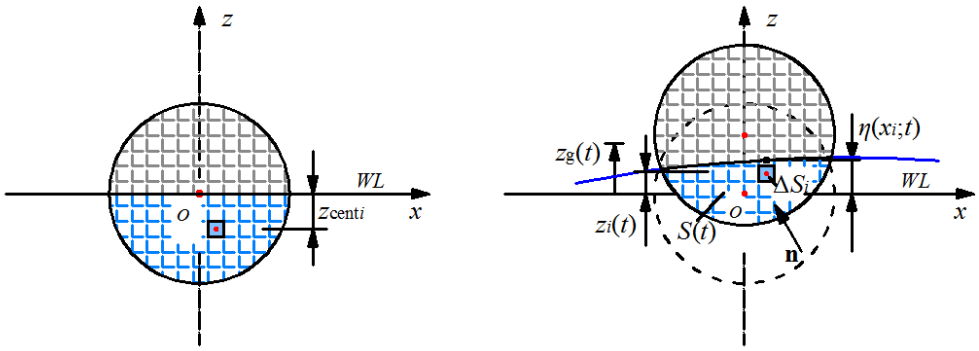

(a) mean wetted surface (b) instantaneous wetted surface

Figure 3.1: Schematics of wetted surface

According to the linear Airy wave theory, the complex velocity potential associated with propagating incident wave in deep water can be expressed as [91]:

$$\Phi_I(x, y, z; t) = -\frac{ig\eta_a}{\omega} e^{kz} e^{ik(x\cos\chi + y\sin\chi) + i\varepsilon} e^{-i\omega t} \tag{3.6}$$

where: (x, y, z) – position vector in fixed reference coordinate;

η_a – wave amplitude;

k – wave number;

χ – wave propagation direction;

ε – wave phase (in rad).

Note that one can set the wave propagation direction as the x direction for an axisymmetric body. Thus, while χ is equal to zero, the wave elevation $\eta(x; t)$ is

$$\eta(x; t) = \text{Re}\left\{-\frac{1}{g}\frac{\partial \Phi_I}{\partial t}|_{z=0}\right\} = \eta_a \cos(\omega t - kx - \varepsilon) \tag{3.7}$$

Furthermore, according to the Bernoulli's equation, the static pressure on the instantaneous wetted surface is:

$$p_{\text{st}} = -\rho g z \tag{3.8}$$

and adding the gravity force, the static part of nonlinear Froude-Krylov force is:

$$f_{\mathrm{FKst}}(t) = f_{\mathrm{g}}(t) + \iint_{S(t)} p_{\mathrm{st}} n_z dS \approx f_{\mathrm{g}}(t) + \sum_{i=1}^{N_m} -\rho g z_i n_{zi} \triangle S_i \tag{3.9}$$

where: n_{zi} – the ith element vertical component of vector normal $\mathbf{n}$;

$\triangle S_i$ – the ith element area;

N_m – the number of elements.

Similarly, the dynamic pressure on the instantaneous wetted surface is

$$p_{\mathrm{dy}} = \mathrm{Re}\left\{-\rho \frac{\partial \Phi_I}{\partial t}\right\} = \rho g \eta_a e^{kz} \cos(\omega t - kx - \varepsilon) \tag{3.10}$$

in order to make the pressure on the free surface equal to zero, Wheeler stretching approximation is adopted with $z' = z - \eta$ substituting z in Eq. 3.10. Then, the dynamic term of the Froude-Krylov force can be expressed as:

$$\begin{aligned} f_{\mathrm{FKdy}}(t) &= \iint_{S(t)} \rho g \eta_a e^{k(z-\eta)} \cos(\omega t - kx - \alpha) n_z dS \\ &\approx \sum_{i=1}^{N_m} \rho g \eta_a e^{k(z_i-\eta)} \cos(\omega t - kx_i - \alpha) n_{zi} \triangle S_i \end{aligned} \tag{3.11}$$

The above derivations hold for monochromatic waves. Under irregular wave conditions, the linear wave superposition theory can also be adopted as that in the linear model. The present work defines it through the nonlinear Froude-Krylov force meshing approach.

B. Analytical approach

The actualization of wetted surface elements requires the real-time wave elevation and buoy displacement, imposing extensive calculations. Therefore, the nonlinear model requires greater computational efforts compared with the linear model. Moreover, as the z_i changes at each time step, the pressure on the wetted elements in the whole frequency range needs to be updated correspondingly. Not to mention the remeshing approach proposed by Gilloteaux [76, 77], Mérigaud et al. [78] and Retes et al. [50] that updates the mesh automatically.

To overcome the disadvantages of inefficiency of meshing approach, Giorgi and Ringwood [80–83], Mérigaud and Ringwood [85], Cong et al. [84] came up with analytical approaches for some axisymmetric bodies, such as sphere and cylinder.

B.1. Static part

Figure 3.2 shows the sphere constrained to move in the vertical direction. In the cylindrical coordinate, (r, θ, ζ), the origin o – fixed on the still water level, with ζ axis pointing upward,

$$\begin{cases} x = r\cos\theta \\ y = r\sin\theta \\ z = \zeta \end{cases} \tag{3.12}$$

The radius $r(\zeta)$, presented in Figure 3.2 (b), changes with the buoy motion as,

$$r(\zeta) = \sqrt{R^2 - (z_g - \zeta)^2} \tag{3.13}$$

the corresponding derivative is,

$$dr(\zeta) = \frac{z_g - \zeta}{\sqrt{R^2 - (z_g - \zeta)^2}} d\zeta \tag{3.14}$$

where: R – sphere radius.

Simultaneously, the vertical projection of the instantaneous wet surface is expressed in the cylindrical coordinate as follows,

$$n_z dS = n_z r d\theta dl = r d\theta dr = (z_g - \zeta) d\zeta d\theta \tag{3.15}$$

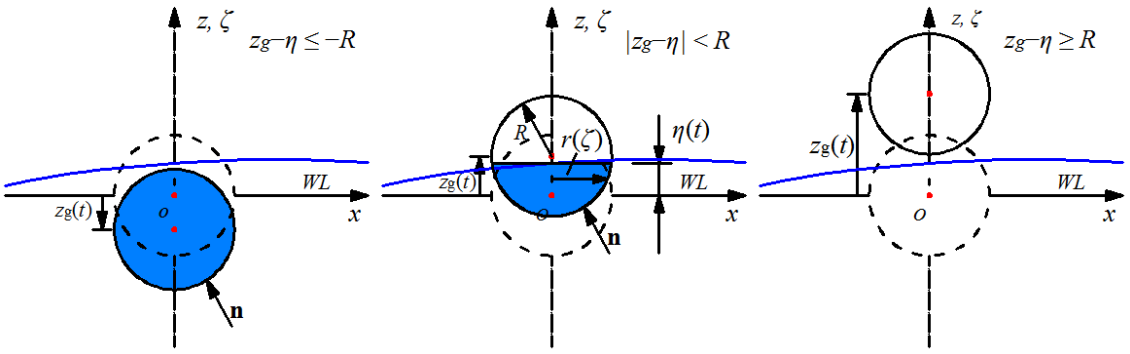

(a) completely immersed in water (b) normal situation (c) completely above water

Figure 3.2: Schematics of a heaving sphere under 3 different situations

Then, in the normal situation ($|z_g - \eta| < R$), ζ satisfies the following condition,

$$\zeta \in [z_g - d_0, \eta] \tag{3.16}$$

the full expression of $f_{\mathrm{FKst}}(t)$ in the cylindrical coordinate is,

$$\begin{aligned} f_{\mathrm{FKst}}(t) &= f_{\mathrm{g}} + \int_0^{2\pi} \int_{z_g - R}^{\eta} -\rho g \zeta (z_g - \zeta) d\zeta d\theta \\ &= \rho g \pi \left[-R^2(z_g - \eta) + \frac{1}{3}(z_g - \eta)^3 - \eta\left(R^2 - (z_g - \eta)^2\right) \right] \end{aligned} \tag{3.17}$$

where, η – wave elevation at $x = 0$, instead of the real elevation changing with the position across the sphere. Such a simplification is due to the very small change of wave elevation that forms the instantaneous wet surface changes for a point absorber.

Besides, as shown in Figure 3.2 (a), the sphere is totally submerged into the water ($z_g - \eta \leq -R$ or $z_g + R \leq \eta$). There will be no waterline, thus

$$f_{\mathrm{FKst}}(t) = f_{\mathrm{g}} + \frac{4}{3}\pi\rho g R^3 = \frac{2}{3}\pi\rho g R^3 \tag{3.18}$$

When the sphere is totally out of the water ($z_g - \eta \geq R$ or $z_g - R \geq \eta$), as shown in Figure 3.2 (c), only the gravity force f_{g} is exerted on the buoy, thus

$$f_{\mathrm{FKst}}(t) = -\frac{2}{3}\pi\rho g R^3 \tag{3.19}$$

For convenience of expression, it unifies all three above equations,

$$f_{\mathrm{FKst}}(t) = f_{\mathrm{g}} + \rho g \pi \left[\frac{2}{3}R^3 - R^2 Z + \frac{1}{3}Z^3 - \eta(R^2 - Z^2)\right] \tag{3.20}$$

where: $Z = \mathrm{sign}(z_g - \eta) \cdot \min(|z_g - \eta|, R)$, $\mathrm{sign}(\cdot)$ is the Sign function,

$$\mathrm{sign}(x) = \begin{cases} 1 & x > 0 \\ 0 & x = 0 \\ -1 & x < 0 \end{cases} \tag{3.21}$$

and $\min(A, B)$ is the minimum value function.

B.2. Dynamic part

Similarly, in the normal situation ($|z_g - \eta| < R$), as shown in Figure 3.2 (b), the dynamic part of Froude-Krylov force is,

$$\begin{aligned} f_{\mathrm{FKdy}}(t) &= \int_0^{2\pi} \int_{z_g - R}^{\eta} \rho g \eta_a e^{k(\zeta - \eta)} \cos(\omega t - kx - \alpha)(z_g - \zeta) d\zeta d\theta \\ &= \int_{z_g - R}^{\eta} \rho g \eta_a e^{k(\zeta - \eta)} (z_g - \zeta) \int_0^{2\pi} \cos(\omega t - kr\cos\theta - \alpha) d\theta d\zeta \end{aligned} \tag{3.22}$$

Through simple derivation, the internal integral can be expressed with the first kind zero-order Bessel function J_0 [97],

$$\int_0^{2\pi} \cos(\omega t - kr\cos\theta - \alpha) d\theta$$

$$= \int_0^{2\pi} \left[\cos(\omega t - \alpha)\cos(kr\cos\theta) + \sin(\omega t - \alpha)\sin(kr\cos\theta)\right] d\theta$$

$$= 2\pi J_0(kr)\cos(\omega t - \alpha) \tag{3.23}$$

Here, substituting Eq. 3.13, the new series expression of $J_0(kr)$ is proposed,

$$J_0\left(kR\sqrt{1-(\frac{z_g-\zeta}{R})^2}\right) \approx \sum_{n=0}^{N_J} c_n \left(\frac{z_g-\zeta}{R}\right)^n \tag{3.24}$$

where: c_n – coefficients obtained through polynomial fitting $J_0(kR\sqrt{1-x^2})$ within $-1 < x < 1$.

In such an approach, the small parameters assumption the Taylor expansion can be avoided as $x = (z_g - \zeta)/R$ satisfies the above condition automatically,

$$z_g - R < \zeta < \eta < z_g + R \tag{3.25}$$

However, c_n should be calculated accordingly for different kR values. By the integration by parts, the dynamic part of nonlinear Froude-Krylov force is derived as,

$$f_{\mathrm{FKdy}}(t) = 2\pi\rho g\eta_a \cos(\omega t - \alpha) \sum_{n=0}^{N_J} c_n \int_{z_g-R}^{\eta} e^{k(\zeta-\eta)}(z_g-\zeta)\left(\frac{z_g-\zeta}{R}\right)^n d\zeta$$

$$= 2\pi\rho g\eta_a \cos(\omega t - \alpha) \sum_{n=0}^{N_J} c_n \left[-\frac{(n+1)!}{k^{n+2}R^n}\sum_{m=0}^{n+1}\frac{k^m(z_g-\zeta)^m}{m!}e^{k(\zeta-\eta)}\Big|_{z_g-R}^{\eta}\right]$$

$$= -2\pi\rho g\eta_a \cos(\omega t - \alpha) \sum_{n=0}^{N_J} c_n \left[-\frac{(n+1)!}{k^{n+2}R^n}\sum_{m=0}^{n+1}\frac{k^m R^m}{m!}e^{-kR}e^{k(z_g-\eta)}\right]$$

$$+ 2\pi\rho g\eta_a \cos(\omega t - \alpha) \sum_{n=0}^{N_J} c_n \left[-\frac{(n+1)!}{k^{n+2}R^n}\sum_{m=0}^{n+1}\frac{k^m}{m!}(z_g-\eta)^m\right] \tag{3.26}$$

To simplify the expression, some variables are adopted,

$$C^{z_g-R}(t) = -2\pi\rho g\eta_a \cos(\omega t - \alpha) \sum_{n=0}^{N_J} c_n \left[-\frac{(n+1)!}{k^{n+2}R^n} \sum_{m=0}^{n+1} \frac{k^m R^m}{m!} e^{-kR} \right] \tag{3.27}$$

$$C_0^{\eta}(t) = +2\pi\rho g\eta_a \cos(\omega t - \alpha) \sum_{n=0}^{N_J} c_n \left[-\frac{(n+1)!}{k^{n+2}R^n} \right] \tag{3.28}$$

$$C_m^{\eta}(t) = +2\pi\rho g\eta_a \cos(\omega t - \alpha) \sum_{n=m-1}^{N_J} c_n \left[-\frac{(n+1)!}{k^{n+2}R^n} \frac{k^m}{m!} \right], \ (m \geq 1) \tag{3.29}$$

Thus,

$$f_{\mathrm{FKdy}}(t) = C^{z_g-R}(t) e^{k(z_g-\eta)} + \sum_{m=0}^{N_J+1} C_m^{\eta}(t)(z_g-\eta)^m \tag{3.30}$$

Note that the $C^{z_g-R}(t)$, $C_0^{\eta}(t)$ and $C_m^{\eta}(t)$ are only related with the wave elevation $\eta(t)$, wave number k and polynomial fitting coefficient c_n. Thus they can be prepared in advance before solving the EOM and then substituted into $f_{\mathrm{FKdy}}(t)$ at each time step.

Considering that the above expression is written in terms of each single frequency, in other words, it is an expression to describe the dynamic part of the nonlinear Froude-Krylov force in regular wave condition.

As wave number k and real-time displacement z_g are still coupled in the exponential term $e^{k(z_g-\eta)}$, the summation of a set of frequency components in the case of irregular wave conditions consumes considerable computational efforts. Thus, one approximation of the exponential term is adopted with the adaptive polynomial fitting as that defined by the Bessel function,

$$\begin{aligned} e^{kR\left(\frac{z_g-\eta}{R}\right)} &= e_0 + \frac{e_1}{R}(z_g-\eta) + \frac{e_2}{R^2}(z_g-\eta)^2 + \cdots + \frac{e_l}{R^l}(z_g-\eta)^l + \cdots \\ &\approx \sum_{l=0}^{N_E} \frac{e_l}{R^l}(z_g-\eta)^l \end{aligned} \tag{3.31}$$

Then, substituting it into Eq. 3.30, and defining

$$C_l^{z_g-R}(t) = C^{z_g-R}(t)\frac{e_l}{R^l} \tag{3.32}$$

One can obtain the expression in terms of the ith wave frequency component,

$$f^i_{\mathrm{FKdy}}(t) = \sum_{l=0}^{N_E} C_{li}^{z_g-R}(t)(z_g-\eta)^l + \sum_{m=0}^{N_J+1} C_{mi}^{\eta}(t)(z_g-\eta)^m \tag{3.33}$$

Considering two similar power terms on the right hand side, Eq. 3.33 can be further expressed as,

$$f_{\mathrm{FKdy}}(t) = \sum_{i=1}^{N_\omega} f^i_{\mathrm{FKdy}}(t) = \sum_{p=0}^{N} C_{p1}(t)(z_g-\eta)^p \tag{3.34}$$

$$N = \max(N_J+1, N_E) \tag{3.35}$$

$$C_{p1}(t) = \begin{cases} \sum_{i=1}^{N_\omega} \left[C_{li}^{z_g-R}(t) + C_{mi}^{\eta}(t)\right] & p = l = m \le \min(N_J+1, N_E) \\ \sum_{i=1}^{N_\omega} \left[C_{li}^{z_g-R}(t)\right] & N_J+1 < p = l \le N_E \\ \sum_{i=1}^{N_\omega} \left[C_{mi}^{\eta}(t)\right] & N_E < p = m \le N_J+1 \end{cases} \tag{3.36}$$

Note that the superscript and subscript i indicate the corresponding variables in terms of the ith frequency component. Through the above arrangements, and using the superposition principle, the dynamic part of the nonlinear Froude-Krylov force $f_{\mathrm{FKdy}}(t)$ in irregular wave conditions is obtained. At this point, it is possible to separate the frequency-dependent term $C_{p1}(t)$ from the real-time displacement z_g. Thus $C_{p1}(t)$ can be pre-calculated so that the computational efforts in irregular wave conditions are dramatically reduced.

When the sphere is totally submerged into the water ($z_g-\eta \le -R$ or $z_g+R \le \eta$), the upper limit of the integration in Eqs. 3.22 and 3.26 – η, is replaced with z_g+R, thus

$$\begin{aligned} f_{\mathrm{FKdy}}(t) &= 2\pi\rho g\eta_a \cos(\omega t-\alpha) \sum_{n=0}^{N_J} c_n \int_{z_g-R}^{z_g+R} e^{k(\zeta-\eta)}(z_g-\zeta)\left(\frac{z_g-\zeta}{R}\right)^n d\zeta \\ &= 2\pi\rho g\eta_a \cos(\omega t-\alpha) \sum_{n=0}^{N_J} c_n \left[-\frac{(n+1)!}{k^{n+2}R^n}\sum_{m=0}^{n+1}\frac{k^m(z_g-\zeta)^m}{m!}e^{k(\zeta-\eta)}\Big|_{z_g-R}^{z_g+R}\right] \\ &= -2\pi\rho g\eta_a \cos(\omega t-\alpha) \sum_{n=0}^{N_J} c_n \left[-\frac{(n+1)!}{k^{n+2}R^n}\sum_{m=0}^{n+1}\frac{k^m R^m}{m!}e^{-kR}e^{k(z_g-\eta)}\right] \\ &\quad + 2\pi\rho g\eta_a \cos(\omega t-\alpha) \sum_{n=0}^{N_J} c_n \left[-\frac{(n+1)!}{k^{n+2}R^n}\sum_{m=0}^{n+1}\frac{k^m(-R)^m}{m!}e^{+kR}e^{k(z_g-\eta)}\right] \end{aligned} \tag{3.37}$$

Similarly, through defining an additional variable,

$$C^{z_g+R}(t) = 2\pi\rho g\eta_a \cos(\omega t - \alpha) \sum_{n=0}^{N_J} c_n \left[-\frac{(n+1)!}{k^{n+2}R^n} \sum_{m=0}^{n+1} \frac{k^m(-R)^m}{m!} e^{+kR} \right] \tag{3.38}$$

together with Eq. 3.27, the new expression of Eq. 3.37 is,

$$f_{\mathrm{FKdy}}(t) = \left[C^{z_g-R}(t) + C^{z_g+R}(t) \right] e^{k(z_g-\eta)} \tag{3.39}$$

Then, adopting the polynomial approximation of exponential term, a new coefficient is defined as,

$$C_l^{z_g+R}(t) = C^{z_g+R}(t)\frac{e_l}{R^l} \tag{3.40}$$

In irregular waves, the ith wave frequency component expression is

$$f_{\mathrm{FKdy}}^i(t) = \left[C_{li}^{z_g-R}(t) + C_{li}^{z_g+R}(t) \right] (z_g - \eta)^l \tag{3.41}$$

the expression of the superposition of different frequency components is,

$$f_{\mathrm{FKdy}}(t) = \sum_{i=1}^{N_\omega} f_{\mathrm{FKdy}}^i(t) = \sum_{l=0}^{N} C_{l2}(t)(z_g - \eta)^l \tag{3.42}$$

$$N = N_E \tag{3.43}$$

$$C_{l2}(t) = \sum_{i=1}^{N_\omega} \left[C_{li}^{z_g-R}(t) + C_{li}^{z_g+R}(t) \right] \tag{3.44}$$

Finally, when the sphere is totally out of the wave, there is no wet surface, so

$$f_{\mathrm{FKdy}}(t) = 0 \tag{3.45}$$

Other authors [85] approximate the relevant exponential function with the Taylor expansion to decouple the wave number and real-time displacement terms,

$$e^{k(z_g-\eta)} \approx \sum_{n=0}^{N} \frac{1}{n!} k^n (z_g - \eta)^n \tag{3.46}$$

Figure 3.3 depicts the corresponding 4th order and 5th order Taylor expansions with different kR values. It is possible to observe that when $x > 0$, the higher order expansion gives better accuracy; when $x < 0$, both the two expansions cannot approximate the function correctly.

However, through adjusting the number of truncated terms depending on the kR values for both exponential function e^{kRx} and Bessel function $J_0(kR\sqrt{1-x^2})$, the present adaptive polynomial fitting technique can ensure better adaptability even

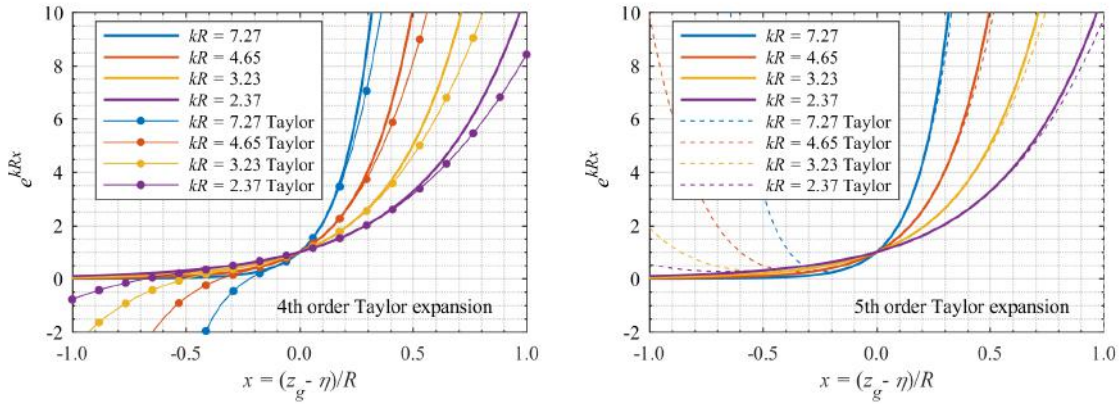

(a) (b)

Figure 3.3: Taylor expansions of e^{kRx} with different kR values

for higher wave steepness conditions as shown in Figure 3.4.

Note that, the above kR values are selected according to the frequencies considered in the irregular wave representation. Chapter 5 presents further details.

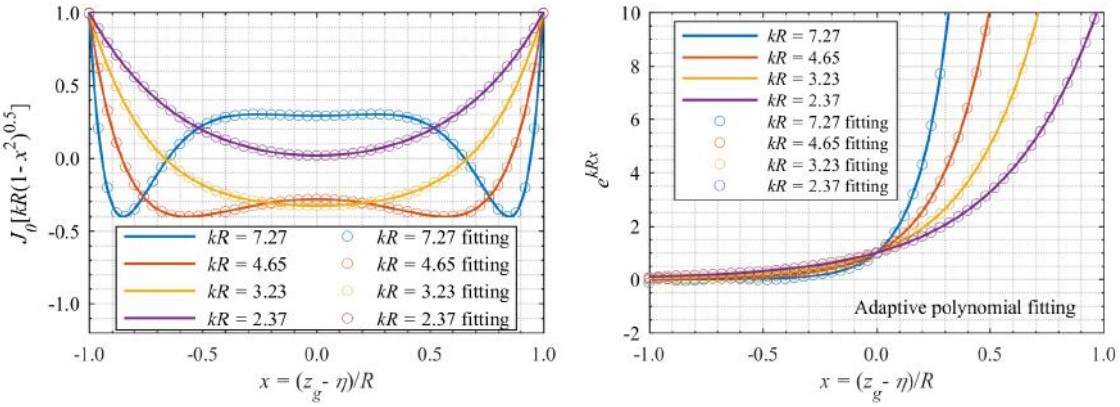

(a) (b)

Figure 3.4: Polynomial fittings of $J_0(kR\sqrt{1-x^2})$ and e^{kRx} with different kR values

Table 3.1 summarizes sphere results obtained for the nonlinear static and dynamic Froude-Krylov force as fully described above.

Table 3.2 compares the normalized computational time of both linear and nonlinear Froude-Krylov force models for a sphere (diameter $D = 5.0$m, discretized surface mesh with 1344 triangular elements) in both regular and irregular wave conditions (500 frequency components used to generate the irregular wave). The meshing approach takes into account the sphere symmetry to reduce the computational efforts. All the simulations are performed by a desktop computer with a processor Intel(R) Core(TM) i7-4790 CPU @ 3.60 Hz.

Note that nonlinear models' CPU time is normalized by the linear model's CPU

Table 3.1: Analytical expressions of the nonlinear Froude-Krylov force for sphere

Static part	Regular/Irregular wave
	$f_{\mathrm{FKst}}(t) = f_{\mathrm{g}} + \rho g \pi \left[\frac{2}{3}R^3 - R^2 Z + \frac{1}{3}Z^3 - \zeta(R^2 - Z^2)\right]$
	where: $Z = \mathrm{sign}(z_g - \eta) \cdot \min(\lvert z_g - \eta \rvert, R)$
Dynamic part	Regular wave
	$\lvert z_g - \eta \rvert < R$
	$f_{\mathrm{FKdy}}(t) = C^{z_g - R}(t) e^{k(z_g - \eta)} + \sum_{m=0}^{N_J+1} C_m^{\eta}(t)(z_g - \eta)^m$
	$z_g - \eta \leq -R$
	$f_{\mathrm{FKdy}}(t) = [C^{z_g - R}(t) + C^{z_g + R}(t)] e^{k(z_g - \eta)}$
	$z_g - \eta \geq R$
	$f_{\mathrm{FKdy}}(t) = 0$
	Irregular wave
	$\lvert z_g - \eta \rvert < R$
	$f_{\mathrm{FKdy}}(t) = \sum_{p=0}^{N} C_{p1}(t)(z_g - \eta)^p$
	$z_g - \eta \leq -R$
	$f_{\mathrm{FKdy}}(t) = \sum_{l=0}^{N} C_{l2}(t)(z_g - \eta)^l$
	$z_g - \eta \geq R$
	$f_{\mathrm{FKdy}}(t) = 0$

Table 3.2: Nonlinear models' normalization CPU time

	Linear	Nonlinear (meshing)	Nonlinear (analytical)
Regular wave	1.0	55.8	1.8
Irregular wave	1.0	150.6	3.8

time. The averaged CPU time taken for the regular wave situation is 0.022 s, while it takes 0.051 s for the irregular wave condition. Moreover, the above comparisons have shown that the analytical approach features higher efficiency than the meshing approach. Such an advantage is more evident for the irregular wave case.

Drag force

Drag force acting on the floating buoy mainly originates from the vortex shedding flow [88]. In general, $f_{\mathrm{drag}}(t)$ increases by a quadratic factor of the relative fluid velocity and is included in the equation of motion by means of a Morison-like term as [98]:

$$f_{\mathrm{drag}}(t) = -\frac{1}{2}\rho C_d A_d \left|\dot{z} - V_0\right| (\dot{z} - V_0) \tag{3.47}$$

where: C_d – drag coefficient;

A_d – projection area of instantaneous wet surface onto water plane;

V_0 – vertical component of undisturbed flow velocity.

C_d is usually derived through minimizing the error between the model simulation and test data in the least-square approach. Such tests contain: free-decay test [99], forced oscillation test and wave excited oscillation test [98] in physical wave tank or/and numerical wave tank. Giorgi et al. [98] have indicated that the estimated drag coefficient obtained through least-square was actually a descriptor of all the nonlinearities not modeled, modeling errors and other possible inaccuracies. Thus, C_d is an equivalent drag coefficient which can fill the gap between the mathematical model and physical/CFD test, other than limited to the viscous effect only. The authors, through the sensitivity studies, also stated that it was preferable to choose a larger drag coefficient, since overestimations caused lower errors than underestimations. Babarit et al. [100]conducted sensitive analysis of the wave energy absorption varying C_d from one quarter to twice their nominal values.

The focus of the present work is not on the nature of drag/viscous effect. The drag force correction used intends to increase modeling accuracy. Hence, it is possible to estimate a nominal C_d value based on the data available in the literature for some simple geometries, such as the sphere, following the necessary sensitive analysis as proposed by [98, 100].

Note that A_d changes if the buoy features a non-uniform waterplane area. When the buoy is completely out of the water, A_d and f_{drag} are obviously null; if the buoy is fully submerged, A_d reaches its maximum value [80].

$$A_d = \begin{cases} \pi R^2 & z(t) - \eta < 0 \\ \pi \left[R^2 - (z(t) - \eta)^2\right] & 0 \leq z(t) - \eta < R \\ 0 & z(t) - \eta \geq R \end{cases} \tag{3.48}$$

Additionally, in wave conditions, the vertical component of the fluid particle velocity usually replaces V_0 in Eq. 3.47.

3.1.3 Performance evaluation

For a WEC, the PTO is one system that transforms the energy absorbed by the primary converter, such as the OWC chamber or a PA buoy vertical motion, into usable electricity. Such a system can be categorized into air turbine, hydro turbine, hydraulic system, direct mechanical drive system and direct electrical drive system [88].

Each one of them behaves in a complicated way due to its practical interdisciplinary applications. To work with a simplified model before a real PTO system is defined/designed, a very common approach adopts the linearized damping to describe the PTO characteristics equivalently. In that case, the force is proportional to the velocity,

$$f_{\mathrm{PTO}}(t) = -B_{PTO} \cdot \dot{z}(t) \tag{3.49}$$

where: B_{PTO} – linearized PTO damping.

Consequently, the mean power absorbed by the PTO in one long period of time gives the ideal performance evaluation,

$$P_m = -\frac{1}{T}\int_0^T f_{\mathrm{PTO}} \cdot \dot{z}(t)dt \tag{3.50}$$

Note that, the PTO force works as a coupled load with the WEC buoy dynamic as well.

Usually, the Capture Width Ratio (CWR) is another non-dimensional parameter which depicts the WEC performance,

$$\mathrm{CWR} = \frac{P_m}{J \cdot D} \tag{3.51}$$

where: D – characteristic WEC dimension (usually the diameter in the water plane);
J – wave energy transport [W/m] (energy per unit time and unit width of the wave front) [89]. For a progressive, plane, harmonic wave with the wave height H and period T, in deep water [101]

$$c_g = \frac{gT}{4\pi} \tag{3.52}$$

$$E = \frac{1}{8}\rho g H^2 \tag{3.53}$$

$$J = c_g \cdot E = \frac{\rho g^2}{32\pi} \cdot H^2 T \tag{3.54}$$

where: c_g – wave group velocity, that is exactly half the phase velocity;
E – energy of the waves per unit area, including both kinetic energy and potential energy.

In irregular waves, using the linear wave superposition assumption, the average wave energy transport for a sea state is expressed as [88, 102],

$$J = \rho g \int_0^\infty c_g S_\zeta(\omega)d\omega = \frac{\rho g^2}{64\pi} \cdot H_S^2 T_e \tag{3.55}$$

where: $S_\zeta(\omega)$ – wave power spectral density;
H_S – significant wave height ($H_S = \sqrt{m_0}$);
T_e – energy period ($T_e = m_{-1}/m_0$);
m_n – the nth order moment of spectrum:

$$m_n = \int_0^\infty S_\zeta(\omega)\omega^n d\omega \tag{3.56}$$

In many sea site data, the peak period T_P is given, instead of T_e, to represent the wave characteristic period, the relationships between these two parameters for different wave spectrum are given,

- for Pierson-Moskowitz spectrum, $T_e = 0.8577T_P$ [103];
- for JONSWAP spectrum with peak shape parameter $\gamma = 3.3$, $T_e = 0.9T_P$ [104].

3.2 Code-to-code verification

Based on the previous mathematical model, one in-house code has been developed to simulate and analyze the WEC. To verify the code, a series of numerical tests are conducted and their results are compared to the data from International Energy Agency (IEA) Ocean Energy Systems (OES) Task 10 project [105, 106].

The IEA OES Task 10 project is aimed at assessing the codes to be used in WEC analysis. It focuses on the accuracy and code validation process of the codes by comparing code to code and code to experimental results [36]. The first phase investigates a 10 m diameter floating sphere. The sphere is restrained to the heave motion only, initially with its origin located on the mean water level and the resonance period around 4.4 s.

Most of the project participant codes use the Cummins equation with/without the weakly nonlinear model. These codes simulate free decay test, responses in regular wave conditions and power absorption in irregular wave conditions numerically. The following sub-sections presents and discuss the results and comparisons featuring each case of the referenced cases.

3.2.1 Free-decay test

Three free decay tests featured three different initial vertical displacements of the buoy: 1 m, 3 m, 5 m. The numerical simulations considered both linear and weakly nonlinear model using the meshing approach. Figure 3.5 presents the displacements for all three cases.

The results for $z_0 = 1\,\mathrm{m}$ indicate good agreement with the in-house code results. There is no significant difference between the linear (WEC LIN) and nonlinear (WEC NLIN) models. When it goes to the case with $z_0 = 3\,\mathrm{m}$, a heave response phase lag starts appearing between the two models. There is an even noticeable difference at $z_0 = 5\,\mathrm{m}$. The results also show good consistency with those from NREL SNL (LIN & NLIN), one participant of the IEA OES Task 10 project. The sphere waterplane area changes much for larger amplitude motion due to its geometric nonlinearity. The hydrostatic restoring force taking into account the instantaneous wetted surface in the weakly nonlinear model behaves in a quite different way from that of the linear model.

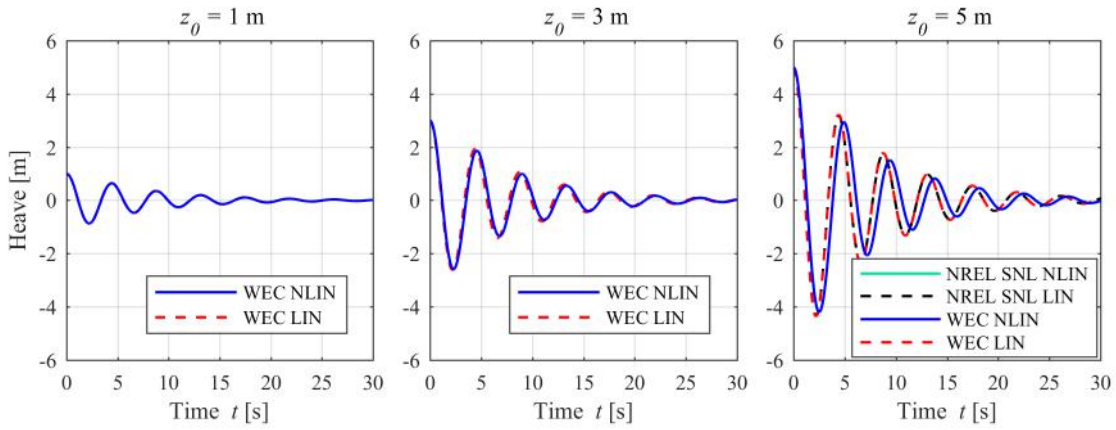

Figure 3.5: Free decay response in heave

The free decay test comparisons allow for validating the hydrostatic restoring forces using both linear and weakly nonlinear model codes.

3.2.2 Regular wave situations

This section analyzes both heave response and mean power in a broad range of wave periods (T) – from 3.0s to 11.0s. For each period, simulations include three different levels of wave steepness (S) values. In deep water, the wave steepness is defined as:

$$S = \frac{H}{gT^2} \tag{3.57}$$

Based on the linear theory, the optimal PTO damping B_{PTO} for each wave period is [89]:

$$B_{PTO} = B(\omega)\sqrt{1 + \left(\frac{C_{WL} - \omega^2(m + A(\omega))}{\omega B(\omega)}\right)^2} \tag{3.58}$$

where: C_{WL} – linear hydrostatic restoring coefficient (sphere: $C_{WL} = \rho g \pi D^2/4$).

Table 3.3 lists the relevant wave conditions involved in the problem, and corresponding optimal PTO damping.

Table 3.3: Regular wave conditions and optimal PTO damping

T [s]	f [Hz]	λ [m]	H_1 [m] $S = 0.005$	H_2 [m] $S = 0.002$	H_3 [m] $S = 0.01$	Optimal B_{PTO} [kNs/m]
3.0	0.333	14.052	0.044	0.177	0.883	398.736
4.0	0.250	24.981	0.078	0.314	1.570	118.150
4.4	0.227	30.227	0.095	0.380	1.899	90.081
5.0	0.200	39.033	0.123	0.491	2.453	161.049
6.0	0.167	56.207	0.177	0.706	3.532	322.292
7.0	0.143	76.504	0.240	0.961	4.807	479.669
8.0	0.125	99.924	0.314	1.256	6.278	633.980
9.0	0.111	126.466	0.397	1.589	7.946	784.083
10.0	0.100	156.131	0.491	1.962	9.810	932.118
11.0	0.091	188.919	0.594	2.374	11.870	1077.123

Note: f – wave frequency; λ – wave length.

Since it is rather difficult to determine the heaving amplitude directly from using the weakly nonlinear model, the heave RAO for each regular wave case was defined as:

$$\text{RAO} = \sqrt{m_{\text{peak}}/\zeta_{\text{peak}}} \tag{3.59}$$

where: m_{peak} – the first order peak of the heave motion power spectral density;

ζ_{peak} – the first order peak of the wave elevation power spectral density.

In Figure 3.6, for the configuration without PTO damping, comparing all different code results no major differences are observed for three steepnesses among different codes. It is easier to understand the phenomenon for the first two lower steepnesses. However, for the larger steepness, only a small decrease in the peak appears with the weakly nonlinear model. For the free-floating sphere, short waves are not strong enough to excite large heave motion. In long waves, the sphere behaves like a wave follower, which mitigates the nonlinearities induced by the instantaneous wetted surface.

The heave RAO adopting the optimal PTO damping still behaves in the same way as for the first two lower wave steepnesses with both linear and nonlinear models (see Figure 3.7). For the larger steepness case illustrated in the third sub-graph in Figure 3.7, the WEC NLIN code predicts a smaller RAO starting from $T = 6\,\text{s}$. The

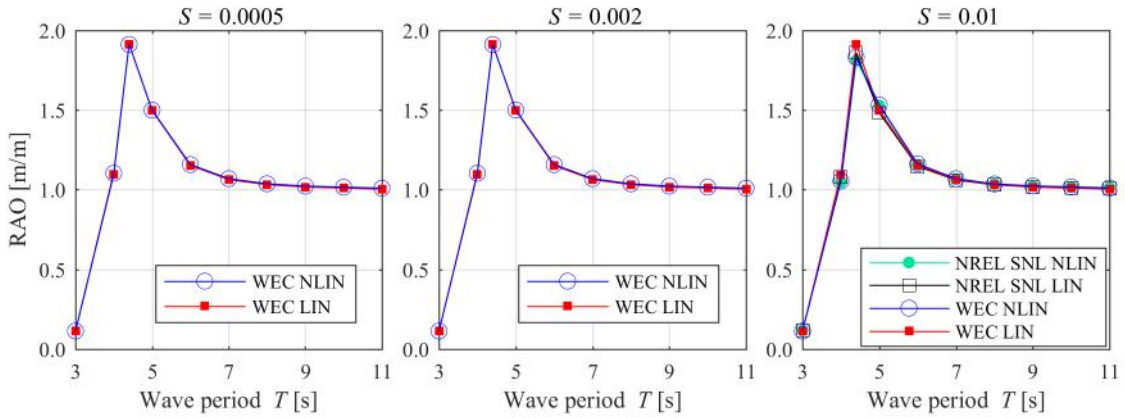

Figure 3.6: Heave RAO, no PTO damping

present reduction is caused by the nonlinearity of both static and dynamic parts of the Froude-Krylov force that comes into effect when wave height increases in comparison with the sphere diameter. The similar patterns appear in the simulations conducted by NREL SNL NLIN from the IEA OES Task 10 project as well.

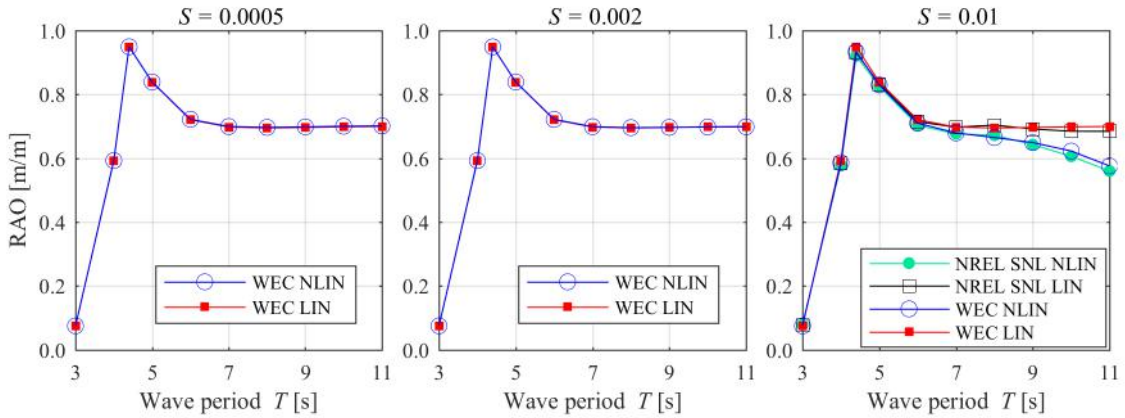

Figure 3.7: Heave RAO with optimal PTO damping

In Figure 3.8, comparing the mean power normalized by wave height squared (H^2) for optimal B_{PTO}, both linear and nonlinear codes present similar variation trends as observed for the heave response in Figure 3.7. Especially, in the weakly nonlinear model prediction, there is a drastic drop after $T = 7$ s for the steepness $S = 0.01$.

In summary, the curve tendencies and key points of both heave motion and power absorption responses calculated by linear and nonlinear models present good consistency with the reference results of the IEA OES Task 10 project.

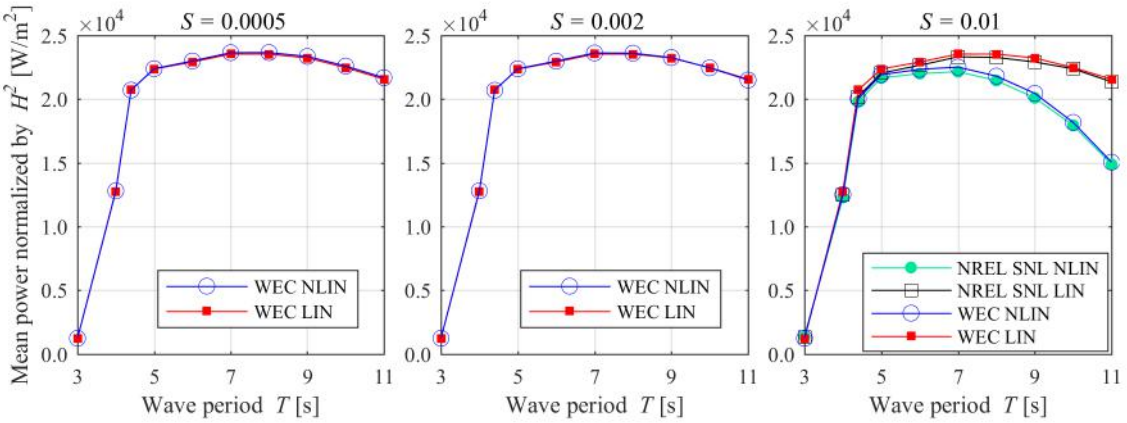

Figure 3.8: Normalized mean power with optimal PTO damping

3.2.3 Irregular wave situations

This section analyzes three groups of typical irregular waves. Table 3.4 summarizes the corresponding optimal B_{PTO}. Note that the prescribed B_{PTO} computed from Eq. 3.58 are not the exact optimal value for the selected wave conditions. However, they could provide realistic, close-to-optimal damping for the sphere motion [105]. The discussion adopts the Bretschneider spectrum.

Table 3.4: Mean power with irregular wave conditions (adapted from [105])

T_P [s]	H_S [m]	S [−]	Optimal B_{PTO} [kNs/m]	P_m [kW] WEC LIN	P_m [kW] WEC NLIN	Differences
4.0	0.5	0.0026	90.081	1.174	1.177	0.171%
6.2	1.0	0.0026	354.083	7.438	7.451	0.259%
15.4	11.0	0.0047	1688.247	1139.607	802.203	29.607%

Note: WEC LIN – code with linear model; WEC NLIN – code with weakly nonlinear model.

Table 3.4 presents the mean power P_m obtained with both linear model (WEC LIN) and nonlinear model (WEC NLIN), and the corresponding relative differences are also presented. For the lower steepness cases, the differences are quite limited. However, for the larger steepness one, the WEC NLIN predicts a drop of P_m around 30% relative to that of WEC LIN. The bar plotting in Figure 3.9 features a consistent mean power level compared to that of codes in IEA OES Task 10 validating the WEC LIN and WEC NLIN results in irregular waves.

Table 3.5 presents the annual average absorbed power (AAP) calculated by using six sea states and corresponding weight factors at a selected North Sea location [60].

Figure 3.10 presents the AAP compared with the IEA OES Task 10 project. The reduction predicted by the WEC NLIN is smaller than the drop appearing in

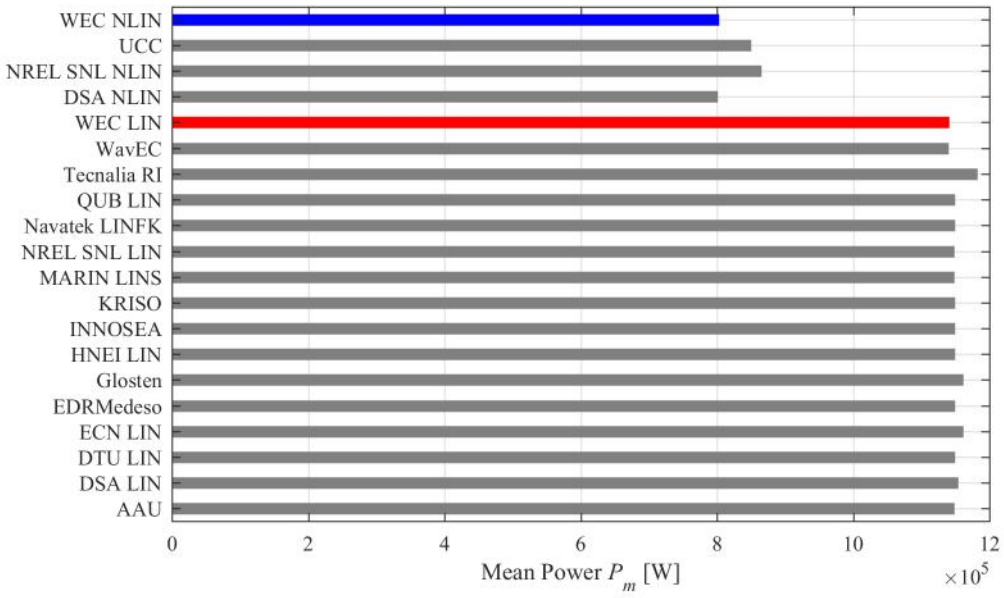

Figure 3.9: Mean power for the irregular wave case, with $H_S = 11.0\,\text{m}$, $T_P = 15.4\,\text{s}$, optimal PTO damping (adapted from [105])

Table 3.5: Irregular sea states and PTO damping (adapted from [106])

H_S [m]	T_P [s]	S_P [−]	Weight [%]	Optimal B_{PTO} [kNs/m]
1	6.6260	0.002322	36.95	424
2	7.5020	0.003622	31.43	558
3	8.3780	0.004357	16.96	690
4	9.2540	0.004761	7.23	819
5	10.1300	0.004967	2.91	947
6.1	11.0936	0.005053	1.41	1090

Note: S_P – average wave steepness in irregular wave conditions.

Figure 3.9. The reason is the lower steepness sea states observed in the majority of the selected sea sites which mitigates the effect of large steepness waves on the reduction predicted by the nonlinear model.

3.3 Summary

The chapter discussed the fundamental mathematical models for both linear and weakly nonlinear models. Especially, this chapter fully described the analytical expressions of the nonlinear Froude-Krylov force (static and dynamic part) for a sphere.

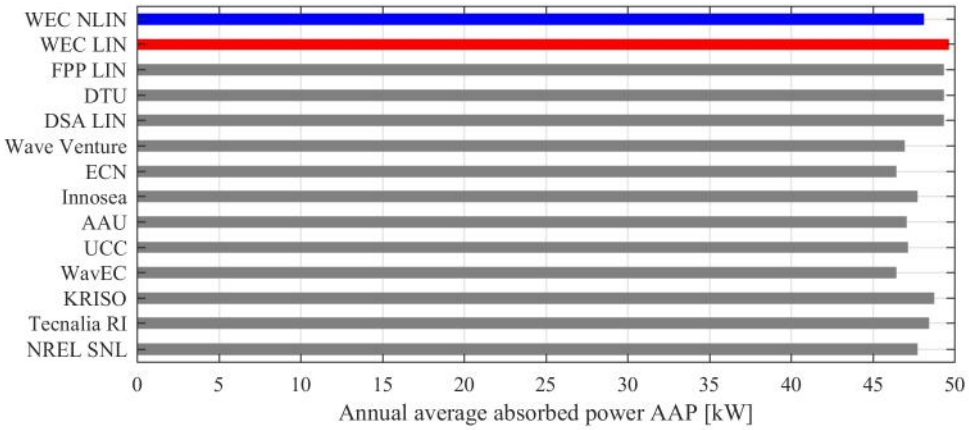

Figure 3.10: Annual average absorbed power AAP, with optimal PTO damping (adapted from [106])

Comparisons between results obtained by an in-house code developed for the linear (WEC LIN) and nonlinear (WEC NLIN) models and as obtained by other codes available in the IEA OES Task 10 project featuring a floating heaving sphere presented good consistencies in the free decay test simulations, regular wave situations and irregular wave situations. The present verification is an important procedure for the accreditation of the results carried out in the following chapters.

Chapter 4

Nonlinear Stiffness System (NSS) in WEC

Nonlinear stiffness system (NSS) can supply additional nonlinear stiffness, preferably negative stiffness, to the original system through some special configurations of mechanical springs, pneumatic cylinders, cantilever beams, magnets, etc. The present chapter investigates a classical NSS with mechanical compression springs (NSMc), including the static analysis which defines three types of system behaviors; the dynamics in regular wave conditions for different system configurations; and the effects of wave height and PTO damping.

4.1 NSS with mechanical compression springs (NSMc)

4.1.1 Description

The classical NSS comprises several mechanical compression springs, supports, and strut. The springs, configured symmetrically, satisfy the requirement of no net horizontal force. In the schematic illustration shown in Figure 4.1, there are only two symmetrical springs. One end of the spring hinges from a support structure fixed or anchored on the sea bottom. The other end hinges from the strut connected to the WEC buoy (sphere in present discussion) following the buoy heave motion, as shown in Figure 4.2. Except for the WEC's heave motion, the other degree-of-freedom motion is restricted.

At the equilibrium position, the springs lie on the horizontal plane where the maximum compressions occur. The total forces are zero in both horizontal and vertical directions. When the buoy leaves out from the equilibrium position assuming either a positive or negative displacement, the springs incline resulting in

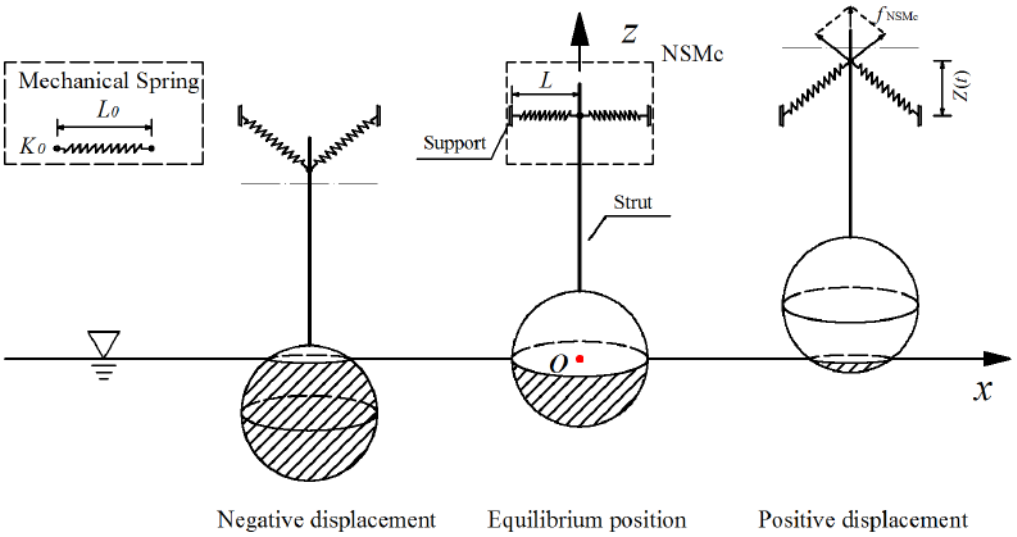

Figure 4.1: Schematic view of NSS with mechanical compression springs (NSMc)

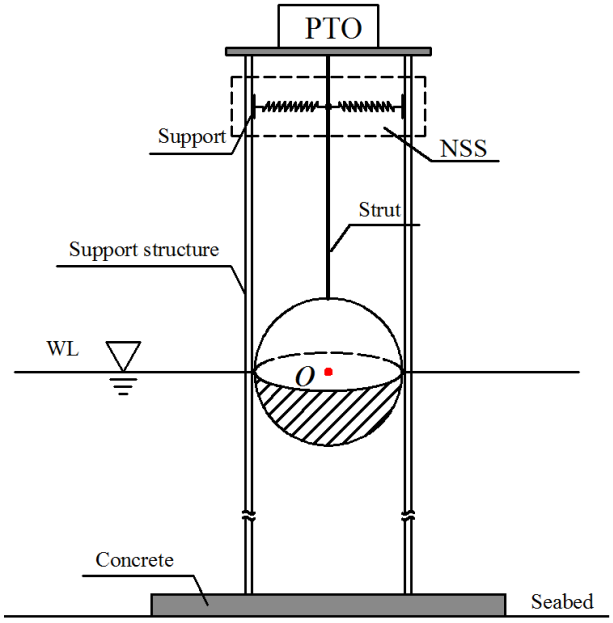

Figure 4.2: Schematic view of PA type WEC with the NSS

a net vertical force acting on the buoy. In addition, the force direction follows the buoy displacement, meaning that the NSMc behaves as a spring pushing the buoy away from the equilibrium. Such a characteristic behavior is the opposite of the hydrostatic restoring force, which pulls the buoy back to the equilibrium. Thus, the special spring geometry configuration supplies an additional "negative stiffness" to the buoy dynamic system.

Figure 4.1 also presents some relevant parameters considered in the analysis. To develop the "negative stiffness" characteristic, the free length (L_0) of the unstressed spring should be longer than the horizontal distance (L) between support and strut. Before the length of the compressed spring recovers to its free length, the NSMc

always supplies some "negative stiffness".

The expression below defines a corresponding limit of the buoy heave displacement,

$$z_{f0} = \pm\sqrt{L_0^2 - L^2} \tag{4.1}$$

Note that stretching one mechanical compression spring is rather difficult. Thus, in practice, NSMc cannot work normally if the buoy exceeds the above limit – Eq. 4.1, as a further discussion described in the following section.

By considering n springs, the NSMc characteristic stiffness (nK_0) will be the summation of all the spring stiffness (K_0), equivalent to the total stiffness of n paralleled springs.

4.1.2 Mathematical model

Based on simple geometry derivation, one can obtain the expression of f_{NSMc} acting on the buoy,

$$f_{\mathrm{NSMc}}(z) = \begin{cases} -nK_0 \cdot z(t) \cdot \left(1 - \dfrac{L_0}{\sqrt{z^2 + L^2}}\right) & |z| \le \sqrt{L_0^2 - L^2} \\ 0 & |z| > \sqrt{L_0^2 - L^2} \end{cases} \tag{4.2}$$

For the sake of simplicity, the term t variable will no longer be used in the following descriptions without causing any additional confusion.

The second expression on the right-hand side corresponds exactly to the practical restriction imposed by mechanical compression springs, as mentioned in the previous section. Consequently, based on the expression of the force, the integral of f_{NSMc} describes the NSMc potential energy [107],

$$\begin{aligned} e_{\mathrm{NSMc}}(z) &= -\int_0^z f_{\mathrm{NSMc}}(\zeta)d\zeta + e_{\mathrm{NSMc}}(0) \\ &= \begin{cases} \dfrac{1}{2}nK_0 \cdot \left(\sqrt{z^2 + L^2} - L_0\right)^2 & |z| \le \sqrt{L_0^2 - L^2} \\ 0 & |z| > \sqrt{L_0^2 - L^2} \end{cases} \end{aligned} \tag{4.3}$$

Here, only the elastic potential energy is taken into account as the NSMc gravity force is small compared with f_{NSMc}. Obviously, the highest potential energy appears at the position $z = 0$. It decreasing gradually until the excursion reaches the limit z_{f0}.

Additionally, for convenience, one may define two non-dimensional parameters

as follows:

$$\text{Stiffness ratio: } \alpha = \frac{C_{WL}}{nK_0} \tag{4.4}$$

$$\text{Geometry ratio: } \gamma = \frac{L}{L_0} \quad \text{(always less than 1.0)} \tag{4.5}$$

The stiffness ratio describes the level of NSMc stiffness, while the geometry ratio measures the compressible length of each spring.

Figure 4.3 depicts one possible example of NSMc static characteristics. The blue solid and red dashed curves correspond to f_{NSMc} and e_{NSMc} values respectively. The additional black dotted curves describe the characteristics without displacement restriction. In the region between the peak and trough of the force curve, the slope is positive, imposing "negative stiffness". At the limiting position z_{f0}, f_{NSMc} is zero and the corresponding e_{NSMc} reaches its troughs, working like two wells. In nonlinear dynamics, they are called "potential wells" and the corresponding system is said to behave like a bi-stable system [35].

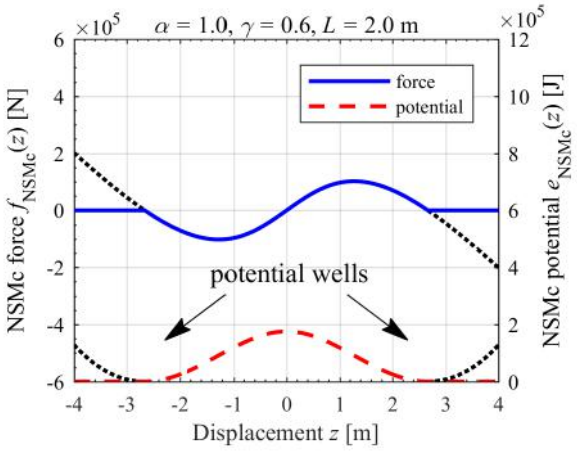

Figure 4.3: NSMc force and potential energy ($\alpha = 1.0$, $\gamma = 0.6$, $L = 2.0\,\text{m}$)

The next section investigates the static characteristics of the combined system to provide a further understanding of the NSMc complex characteristics and its influence on the buoy dynamic system.

4.2 Static characteristic analysis

First, this section analyzes the sphere hydrostatic characteristics. The nonlinear model evaluates the static restoring force f_{hs} and potential energy e_{hs}. Figure 4.4 describes the corresponding characteristic curves of a sphere (diameter $D = 5.0\,\text{m}$) using the linear hydrostatic force (black dash-dot curve) as the reference. Different

from the NSMc case, only one "potential well" would appear in the potential energy curve.

$$f_{\mathrm{hs}}(z) = \begin{cases} -mg & z \geq +D/2 \\ -\dfrac{\rho g \pi D^2}{4}\left(1 - \dfrac{4z^2}{3D^2}\right) \cdot z & |z| < D/2 \\ mg & z \leq -D/2 \end{cases} \tag{4.6}$$

$$e_{\mathrm{hs}}(z) = \begin{cases} mg\left(z - \dfrac{D}{2}\right) + \dfrac{5\rho g \pi D^4}{192} & z \geq +D/2 \\ \dfrac{1}{2}\dfrac{\rho g \pi D^2}{4} \cdot z^2 \cdot \left(1 - \dfrac{2z^2}{3D^2}\right) & |z| < D/2 \\ -mg\left(z + \dfrac{D}{2}\right) + \dfrac{5\rho g \pi D^4}{192} & z \leq -D/2 \end{cases} \tag{4.7}$$

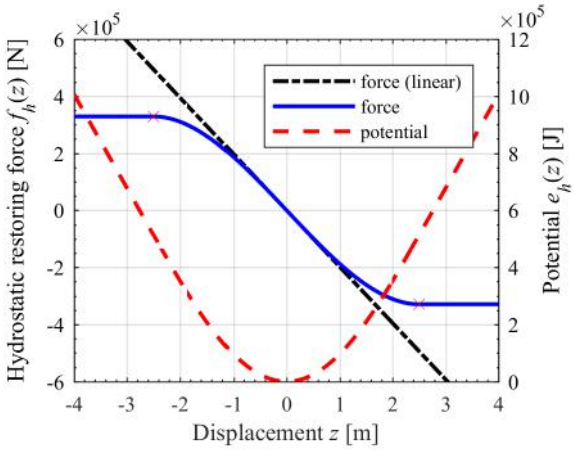

Figure 4.4: Sphere hydrostatic restoring force and potential energy

Figures 4.5 and 4.6 present the corresponding static characteristics, combining NSMc and WEC buoy individual characteristics. The blue dash-dot curves describe the sphere nonlinear hydrostatic force; the blue solid curves depict the static force of the combined system; the red dashed curves show the corresponding potential energy. The corresponding subgraphs (left, middle and right) define three types of possible behaviors: bi-stable, Quasi-Zero Stiffness (QZS), and mono-stable characteristics depending on different NSMc configurations defined by α, γ and L. To illustrate the information in Figures 4.5 and 4.6, one may define the critical value

γ_{cr} and the corresponding ratio C_γ,

$$\gamma_{cr} = \frac{1}{1+\alpha} \tag{4.8}$$

$$C_\gamma = \frac{\gamma}{\gamma_{cr}} = \gamma(1+\alpha) \tag{4.9}$$

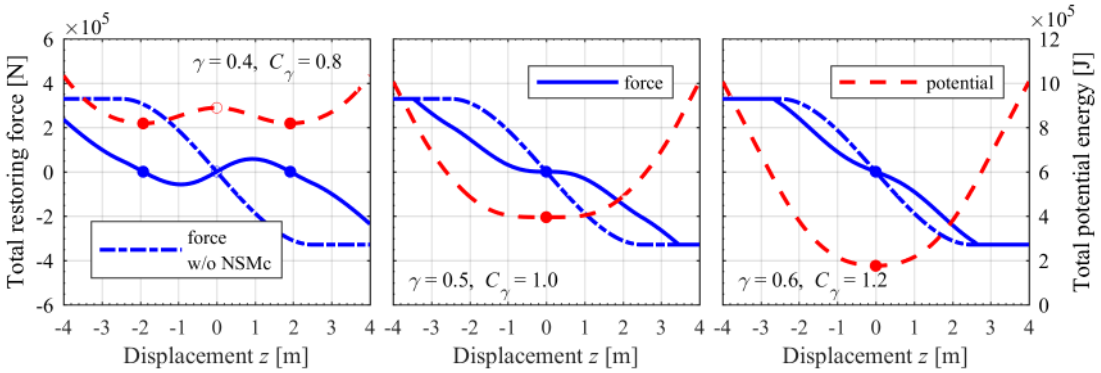

Figure 4.5: Sphere static characteristics with NSMc ($\alpha = 1.0$, $L = 2.0$ m)

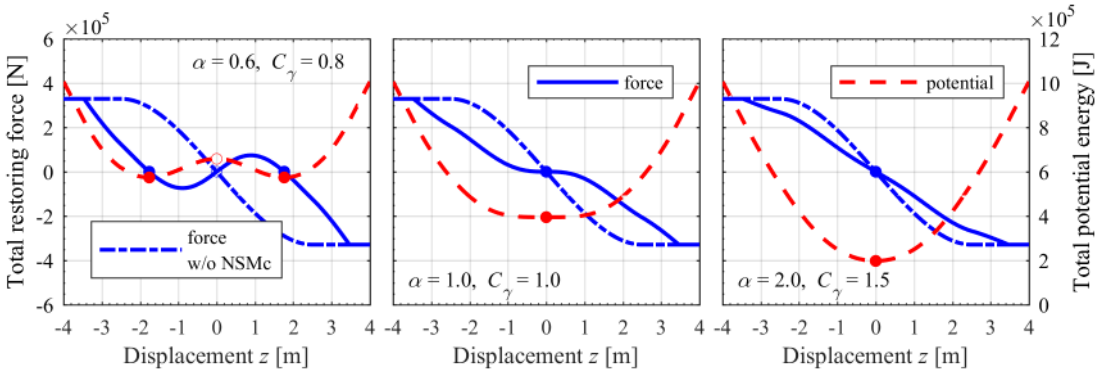

Figure 4.6: Sphere static characteristics with NSMc ($\gamma = 0.5$, $L = 2.0$ m)

- Bi-stable (Figures 4.5 and 4.6, left subgraphs, with $C_\gamma < 1$)
  The potential energy curve features three extreme points: one maximum and the other two minimum points. The solid dots illustrate the positions and characteristics corresponding to the minimum potential energy. If the system is displaced at an arbitrarily small distance away from the minimum potential energy positions, the force restores the buoy to its equilibrium. Such a system is, therefore, stable.

  In contrast, if a small perturbation occurs at the local extremum potential position (circle makers, in Figures 4.5 and 4.6), the force drives the system even further away from its equilibrium. Such a system is, therefore, unstable

[108]. That is the reason why the system containing two "potential wells" is named bi-stable.

In the case of a sphere, due to the nonlinearity of its hydrostatic potential energy, there are no analytical expressions relating to its positions with the two minimum points. On the other hand, with linear hydrostatic potential energy, it would not be difficult to obtain such analytical solutions for the positions [109]. However, depending on the relation between force and potential energy, the positions corresponding to the extreme points of the potential energy are the zeros of the static force function. They can be defined graphically as shown in Figures 4.5 and 4.6.

- QZS (Figures 4.5 and 4.6, middle subgraphs, with $C_\gamma = 1$)
  One local minimum point appears at the equilibrium position of the potential energy curve. However, the corresponding potential energy second derivative is zero. Therefore, it presents a different characteristic from the bi-stable system (greater than zero) discussed earlier; and also different from the mono-stable system (less than zero) to be discussed next. In this case, the single minimum defines a neutral stable state. Furthermore, the potential energy second derivative defines the system stiffness which is equal to zero at $z = 0$, in the present case. Thus, QZS identifies the characteristic of this type of system.

- Mono-stable (Figures 4.5 and 4.6, right subgraphs, with $C_\gamma > 1$)
  If only one stable point appears at the origin and the corresponding stiffness is positive, the system will be mono-stable.

The above analysis would impose a convenient way to consider the ratio C_γ to distinguish the system behavior. Fixing α and increasing γ, the force of the combined system approaches the single buoy dynamic system (as shown in Figure 4.5); and vice versa (as shown in Figure 4.6). In other words, the greater the α the lower the stiffness; as well as the larger γ corresponds to the smaller compressible length, weakening the role of the NSMc effect. Thus, the characteristic of the combined system tends to approach the single buoy dynamic behavior.

The additional negative stiffness supplied by NSMc reduces the stiffness (force curves slope) in the region around the equilibrium position ($z = 0$). The negative stiffness even appears in the bi-stable combined system. Together with the sphere hydrostatic nonlinearity due to its non-uniform waterplane area, it would be possible to add to these two kinds of nonlinearities as they both act to decrease the system stiffness. Such a configuration may benefit the point absorber efficiency to extract

energy from ocean waves. The next section discusses and investigates these effects under regular wave conditions.

4.3 Response in regular wave

The present section evaluates the dynamic performance for both cases: the system working without NSMc and the combined system respectively.

4.3.1 Case without NSMc

Figure 4.7 presents the sphere linear hydrodynamic characteristics (sphere: $D = 5.0$ m). The sphere surface discretized into 1344 triangles, as shown in Figure 4.7 (a), allows for the nonlinear Froude-Krylov force calculation adopting the meshing approach mentioned in Chapter 3. In the following sections, the analytical approach validated by the meshing approach is also used to calculate the nonlinear Froude-Krylov force.

In Figure 4.7 (b), the hydrodynamic coefficients derived from the Hulme [93] non-dimensional data using asymptotic expression show the added mass $A(\omega)$ and damping coefficient $B(\omega)$ values; while FDI method [110] calculates the constant coefficient matrices $\boldsymbol{A}_R$, $\boldsymbol{B}_R$, $\boldsymbol{C}_R$ for the use by the state-space model. Table 4.1 presents the coefficient of determinations (R^2) of $A(\omega)$ and $B(\omega)$ obtained by a fourth-order model (note: accuracy increases if R^2 approaches unity [111]).

Table 4.1: R^2 of hydrodynamic coefficients approximations

$R^2(A)$	0.999982193365857
$R^2(B)$	0.999946466287517

In addition, the RIRF also compares to the result obtained by the direct Filon's integral approach [97] as shown in Figure 4.7 (c). The two comparisons confirm the good accuracy of the state-space model.

Finally, Figure 4.7 (d) depicts the amplitude and phase shift responses of the linear wave excitation force adopted from the data published by Chen [112] with the BEM.

The buoy undamped natural period, based on the well-known expression,

$$T_n = 2\pi\sqrt{\frac{m + A_\infty}{C_{WL}}} \tag{4.10}$$

for the sphere ($D = 5.0$ m) will be 3.2 s.

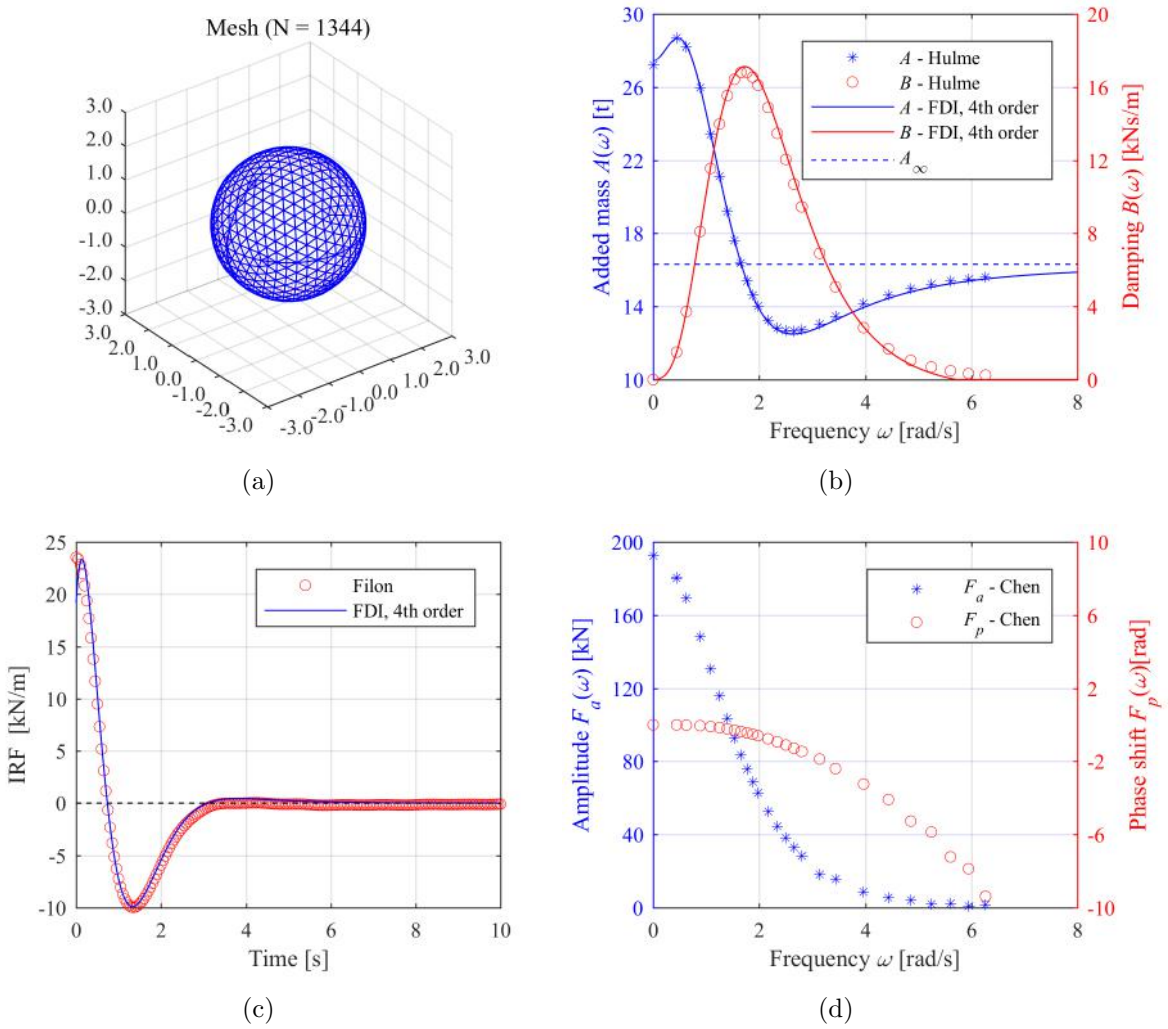

Figure 4.7: Sphere ($D = 5.0$ m) hydrodynamic characteristics

To avoid strongly nonlinear wave acting on the buoy, the wave heights are restricted in according to the wave steepness (S)

$$S = 2\pi \frac{H}{gT^2} \tag{4.11}$$

given in Table 4.2. Here, $S = 0.018$ is the limit value for the linear wave theory[81]. Note that the wave steepness definition in Eq. 3.57 lacks one term of 2π compared with the present definition. Simultaneously, following the conversion, the largest wave steepnesses for both regular and irregular wave conditions appearing in the IEA OES Task 10 project exceed the corresponding $S = 0.025$. Thus, when investigating the nonlinear Froude-Krylov force, higher steepness ($S = 0.025$) is allowed to verify the analytical approach accuracy.

Figure 4.8 to Figure 4.10, present the CWR$-B_{PTO}$ patterns and the corresponding differences obtained by distinct approaches under the wave steepness defined in Table 4.2:

Table 4.2: Regular wave conditions

	$T[s]$	2.0	3.0	3.2	3.5	5.0	7.0
$S = 0.010$	H[m]	0.06	0.14	0.16	0.19	0.39	0.77
$S = 0.018$	H[m]	0.11	0.25	0.29	0.34	0.70	1.38
$S = 0.025$	H[m]	0.16	0.35	0.40	0.48	0.98	1.91

- linear (FD) – linear model in frequency-domain;
- linear (TD) – linear model in time-domain;
- nonlinear (meshing) – using the meshing approach to calculate the nonlinear Froude-Krylov force in time-domain;
- nonlinear (analytical) – using the analytical approach to calculate the nonlinear Froude-Krylov force in time-domain.

In these figures, the curves depicting the linear (FD) and linear (TD) results present quite good agreements, confirming the adequate accuracy of the adopted basic time-domain model.

Additionally, the figures feature the relative difference (Diff_1) between the linear (TD) and nonlinear (analytical) models, and the relative difference (Diff_2) between the nonlinear (meshing) and nonlinear (analytical) models.

$$\text{Diff}_1 = \frac{\text{CWR}_{\text{linear}} - \text{CWR}_{\text{nonlinear}}}{\text{CWR}_{\text{linear}}} \times 100\% \tag{4.12}$$

$$\text{Diff}_2 = \frac{\text{CWR}_{\text{meshing}} - \text{CWR}_{\text{analytical}}}{\text{CWR}_{\text{meshing}}} \times 100\% \tag{4.13}$$

The improved analytical approach to calculate the nonlinear Froude-Krylov force in regular wave conditions also shows differences not greater than 2% if compared with the reliable meshing approach results (blue solid curves, from Figure 4.8 to Figure 4.10). Increasing the wave steepness, the differences between linear and nonlinear approaches (red dashed curves, from Figure 4.8 to Figure 4.10) become more significant, within the whole wave period range. It means that that the sphere nonlinear Froude-Krylov force plays an important role even for a relatively steep wave. Simultaneously, larger differences in longer waves, as well as higher waves, feature greater nonlinear effects even for the same wave steepness.

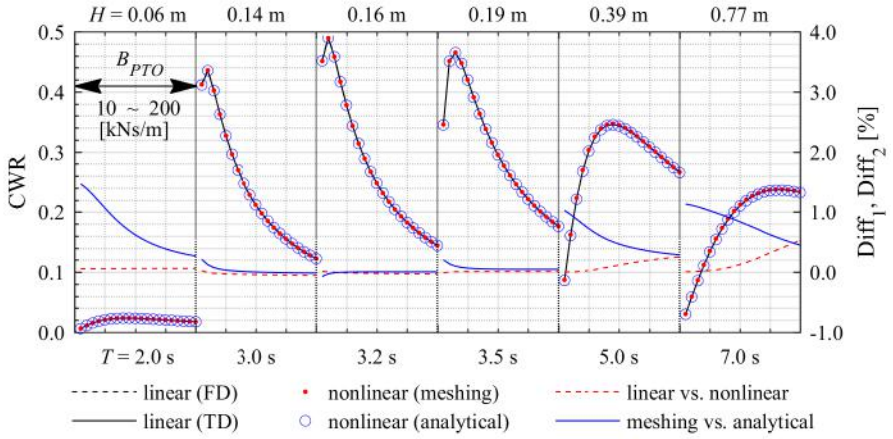

Figure 4.8: CWR calculated by different approaches ($S = 0.010$)

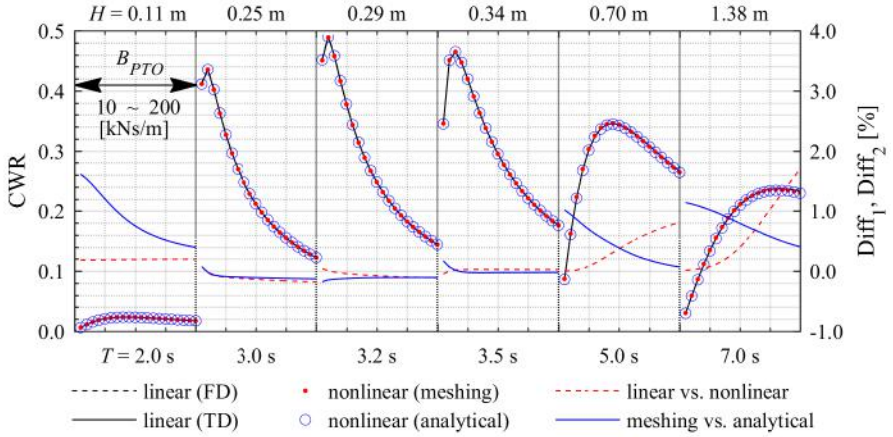

Figure 4.9: CWR calculated by different approaches ($S = 0.018$)

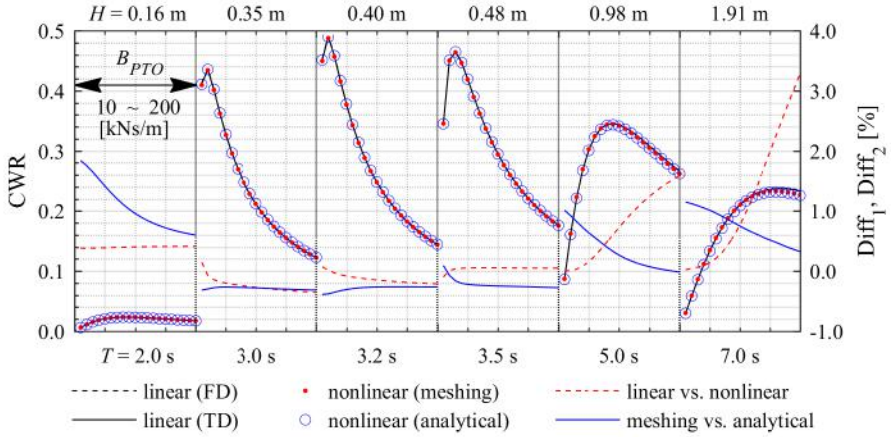

Figure 4.10: CWR calculated by different approaches ($S = 0.025$)

On the other hand, there exists one optimal B_{PTO} for each wave condition, that becomes larger as the wave period increases but does not change much with the wave steepness.

To better understand the difference between the linear and nonlinear models, Figures 4.11 and 4.12 present the buoy displacement, phase portraits and amplitude spectrum corresponding to three different wave steepnesses for the case with $B_{PTO} = 170$ kNs/m, wave period $T = 7.0$ s ($f = 0.143$ Hz) respectively. Note that the amplitude spectrum use a logarithm scale to distinguish different frequency components that appear in the spectrum obviously.

The displacement responses present well defined periodic orbits, and all the phase portraits (v velocity versus z displacement) describe regular rings around $z = 0$ and $v = 0$ (in the present section without NSMc). However, using the nonlinear approach, two additional amplitude peaks appear in the spectral curves (see Figure 4.12) about two orders of magnitude smaller than the primary amplitude at the regular wave frequency. They correspond twice and three times wave frequencies respectively. Thus, the response in a regular wave condition is no longer exactly "regular". In other words, in the case of a non-uniform waterplane buoy, it would be necessary to consider the nonlinear model.

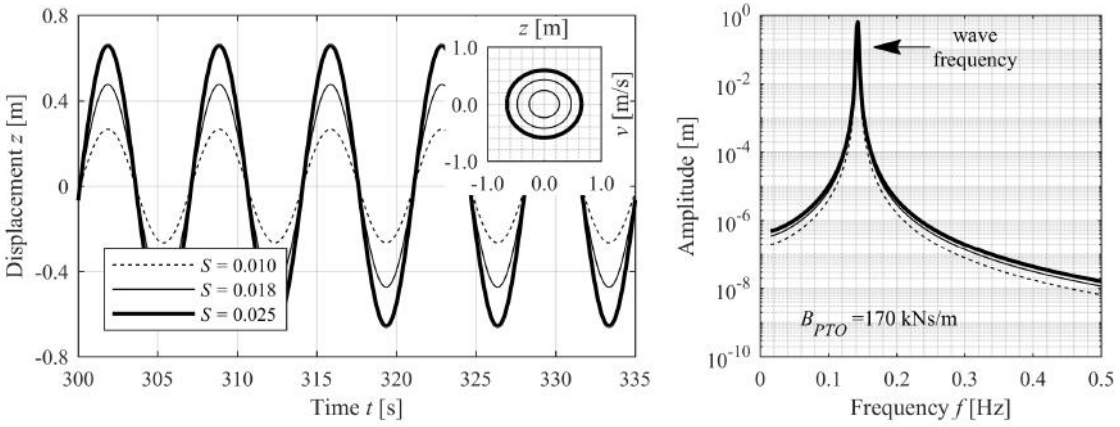

Figure 4.11: Linear model results ($T = 7.0$ s): displacements, phase portraits, and spectrum

It should be noticed that the Fast Fourier Transform (FFT) (using the Hanning window) used to calculate the spectrum, may incorporate some minor numerical errors on the magnitudes, but they would not affect multiple peak frequencies shown in Figure 4.12.

For the sake of convenience, Figures 4.13 and 4.14 present comparisons of the sphere CWR response curves featuring the model without NSMc under different wave heights. From these figures, it is possible to see that the peak response increases for the sphere without NSMc if B_{PTO} increases from 10 kNs/m to 30 kNs/m, and continually decreases for higher B_{PTO}. Simultaneously, the period corresponding to the CWR peak is always shifted further ahead if B_{PTO} increases.

The areas between $T = 3$ s and $T = 5$ s in Figures 4.13 and 4.14, show that if

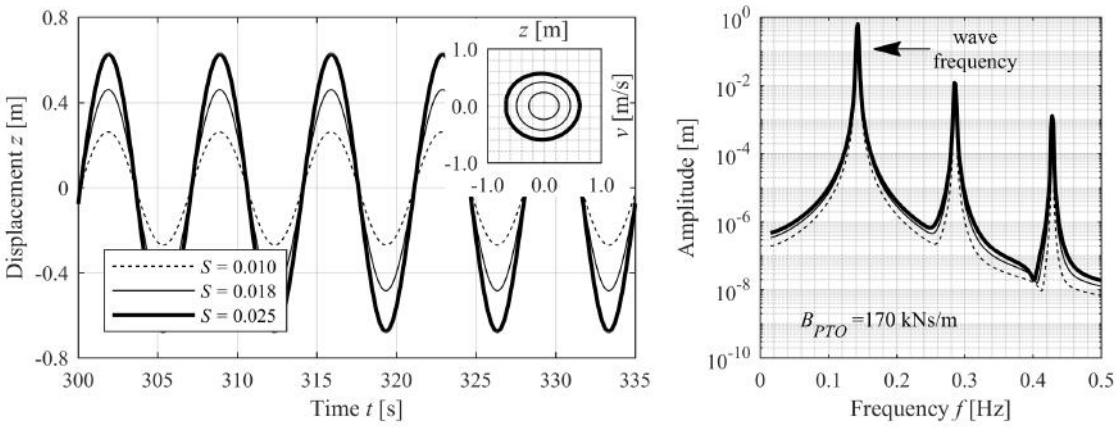

Figure 4.12: Analytical nonlinear model model results ($T = 7.0$ s): displacements, phase portraits, and spectrum

the wave height increases, the CWR response from the linear model (green dash-dot curves) does not change much. But the nonlinear model in the meshing approach makes the response curve shift to larger periods (red solid curves). Still, more importantly, the differences between meshing and analytical approaches become more significant, indicating that the analytical approach is not so accurate for wave height higher than $H = 2.0$ m and wave period T close to the natural period of 3.2 s. Note that the resonant wave condition for the linear model features higher steepness mostly due to its small natural period.

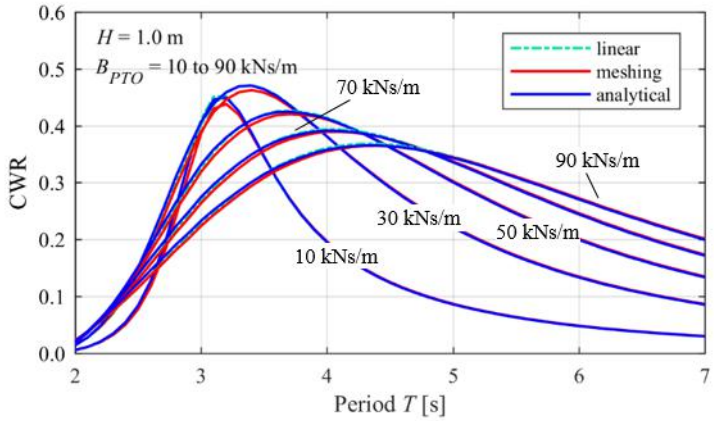

Figure 4.13: Sphere CWR without NSMc ($H = 1.0$ m)

4.3.2 Case with NSMc

Section 4.2, showed that through the combination of the heaving sphere and NSMc, it would be possible to build a different dynamic system presenting either bi-stable, QZS or mono-stable characteristics, depending on the configuration defined by (α,

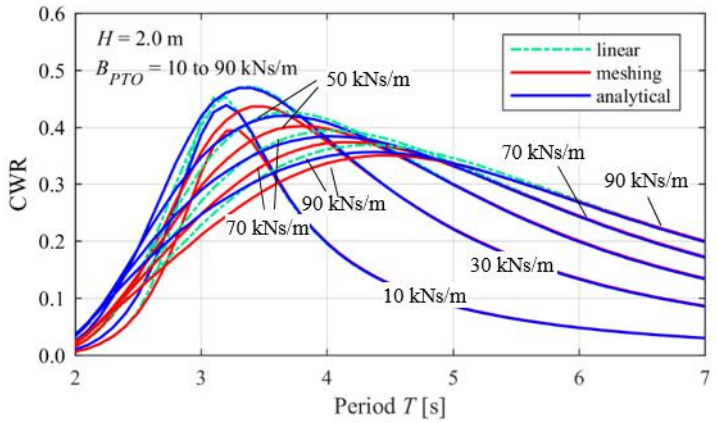

Figure 4.14: Sphere CWR without NSMc ($H = 2.0$ m)

γ) parameters. The following discussions feature the possible configurations of the sphere buoy with NSMc.

Bi-stable configuration

To define a bi-stable system, one may select the parameters: $\alpha = 1.0$, $\gamma = 0.4$, and $L = 2.0$ m as $C_\gamma = 0.8 < 1.0$.

Firstly, Figure 4.15 shows the CWR response considering a relatively small B_{PTO} (10kNs/m) case. The results correspond to the different approaches discussed above: linear, nonlinear (meshing) and nonlinear (analytical). Each item in Figure 4.15 describes results for 50 sets of different initial conditions (z_0, v_0). For the most of the cases, the agreement confirms the good quality of the analytical approach (empty blue circles) to be used in further NSMc investigations.

The linear approach with NSMc (green dots, in Figure 4.15) shows that the period corresponding to the CWR peak equals $T = 5.8$ s, which is much higher than the original natural period ($T = 3.2$ s). However, in the nonlinear approach results, two branches appear in the curves: one with a local maximum value around the natural period; and the other branch very close to the linear solution. Responses are now more complex than without NSMc, but the results obtained for all sets of different initial conditions converge to fall around only three values at most.

To better understand such a response behavior, the next discussion features details for a selection of typical cases. The cases P_1, P_2 and P_3 correspond to wave period $T = 3.1$ s, while P_4, P_5 and P_6 adopt $T = 10.1$ s.

In Figures 4.16 and 4.17, the two blue dashed lines, describe two stable equilibrium positions (at $z = \pm 1.92$ m) of the bi-stable dynamic behavior. The displacements are always periodic: the motions of P_1, P_2, P_3, P_5 and P_6 are all around either stable equilibrium position (usually called "intra-well" motion in nonlinear dynam-

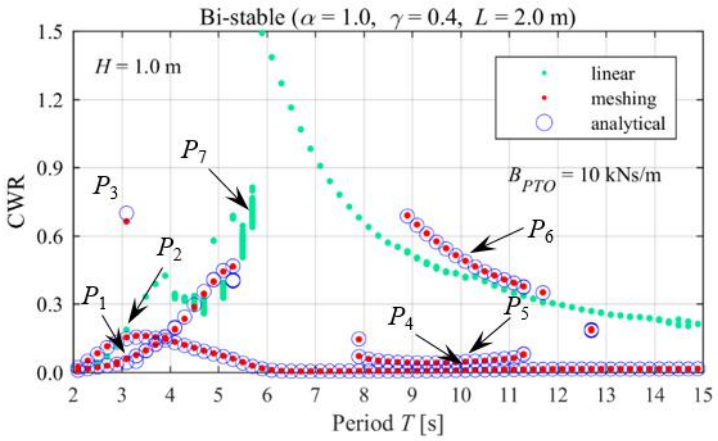

Figure 4.15: Sphere CWR with NSMc: bi-stable configuration ($H = 1.0\,\text{m}$, $B_{PTO} = 10\,\text{kNs/m}$)

ics). Such a phenomenon is physically similar to a ball trapped in a well with a high potential obstacle hard to overcome. Thus, the displacement amplitude will be also small. In the case of P_3 (black thick solid curve in Figure 4.16), the amplitude seems to be bigger than the others, not only due to additional frequency components, but also the wave excites half of the wave frequency component response (as shown in the spectral curve in Figure 4.16).

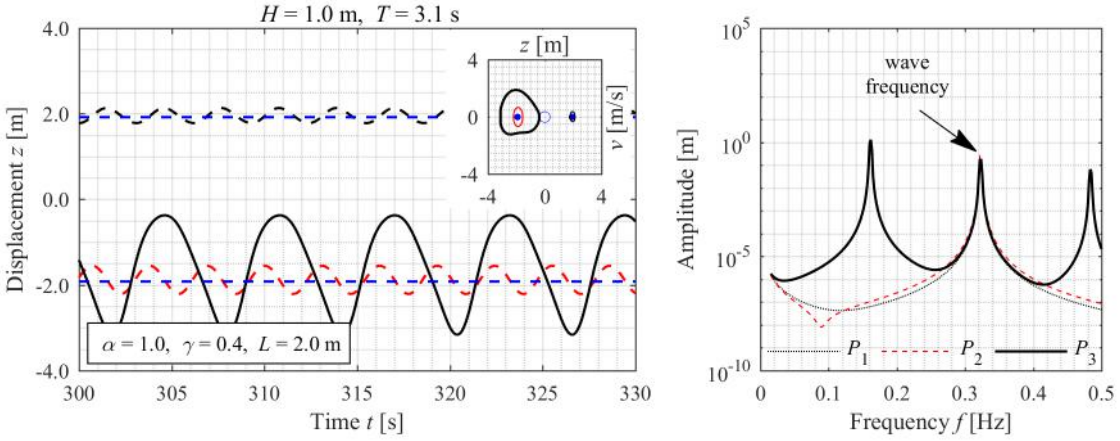

Figure 4.16: Analytical nonlinear model results ($T = 3.1$ s, $B_{PTO} = 10$ kNs/m): displacements, phase portraits, and spectrum

For the P_6 case (black thick solid curve in Figure 4.17), the phase portrait covers both two existing stable equilibrium positions. It means that the motion overcomes the potential barrier from one potential well to the other one, making the corresponding amplitude much larger. Such a type of motion is defined as an "inter-well" type of motion accordingly. In that case, a powerful wave will be able to supply enough energy to make the buoy to overcome the potential well obstacle relative to the other "intra-well" points which may happen in some specific initial conditions.

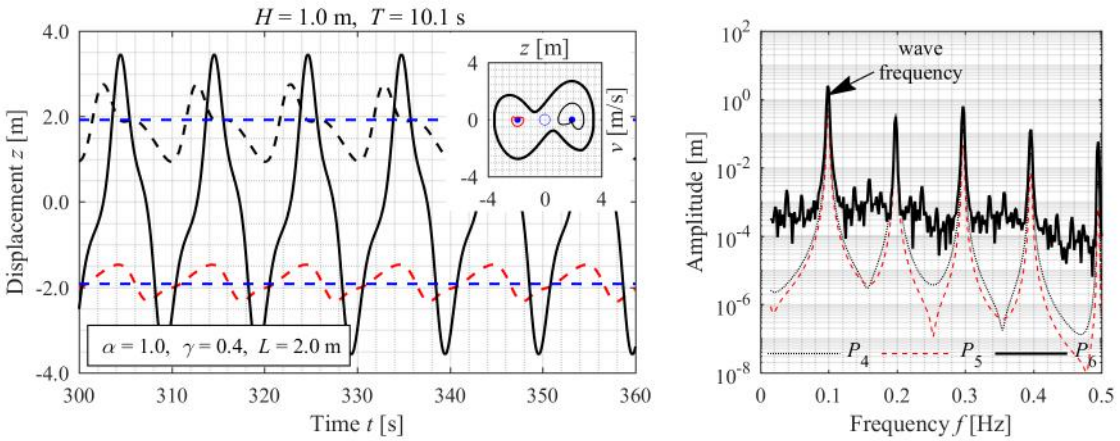

Figure 4.17: Analytical nonlinear model results (T = 10.1 s, B_{PTO} = 10 kNs/m): displacements, phase portraits, and spectrum

Between T = 4.1 s and T = 5.7 s, a special case occurs and needs to be further considered: the "chaotic" motion with the linear model – P_7, as shown in Figure 4.18. Sometimes the buoy motion is trapped within one potential well or goes across the potential well obstacle. Such a motion is a random combination of the "intra-well" and "inter-well" motions. It could happen even in regular wave conditions, and it is rather difficult to be predicted.

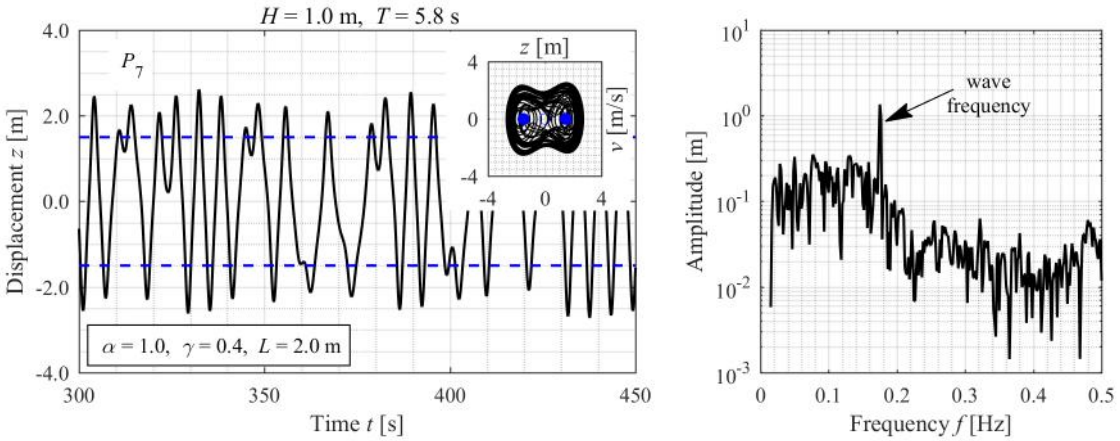

Figure 4.18: Linear model results (T = 5.8 s, B_{PTO} = 10 kNs/m): displacement, phase portrait, and spectrum

Surprisingly, the "chaotic" motion did not appear in the nonlinear model. It could be attributed to the joint action of two different types of nonlinearities: the nonlinear Froude-Krylov force and NSMc effect, which increases the difficulties to escape from the potential well.

The nonlinear model CWR with NSMc becomes more regular (as shown in Figure 4.19) for large B_{PTO} ($>$ 30 kNs/m). In such a case, there is no special point P_3 as shown in Figure 4.15. The large damping effect imposed some more difficulties.

Furthermore, around the stable equilibrium points (in Figures 4.20 and 4.21) the buoy can only experience small amplitude "intra-well" motions. On the other hand, the transition region of the linear model shifts the responses to longer wave period ranges.

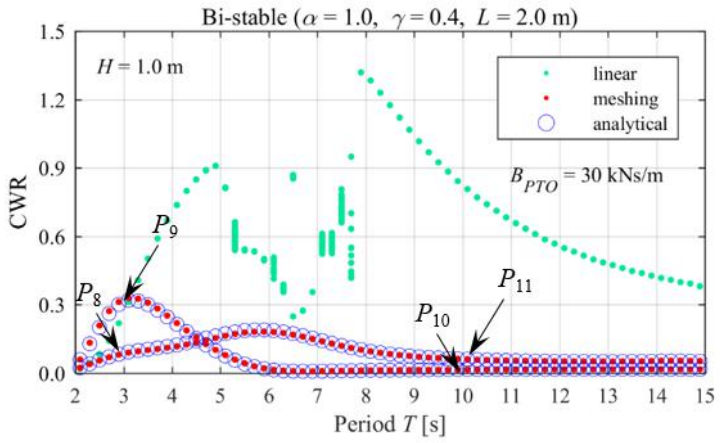

Figure 4.19: Sphere CWR with NSMc: bi-stable configuration ($H = 1.0\,\text{m}$, $B_{PTO} = 30\,\text{kNs/m}$)

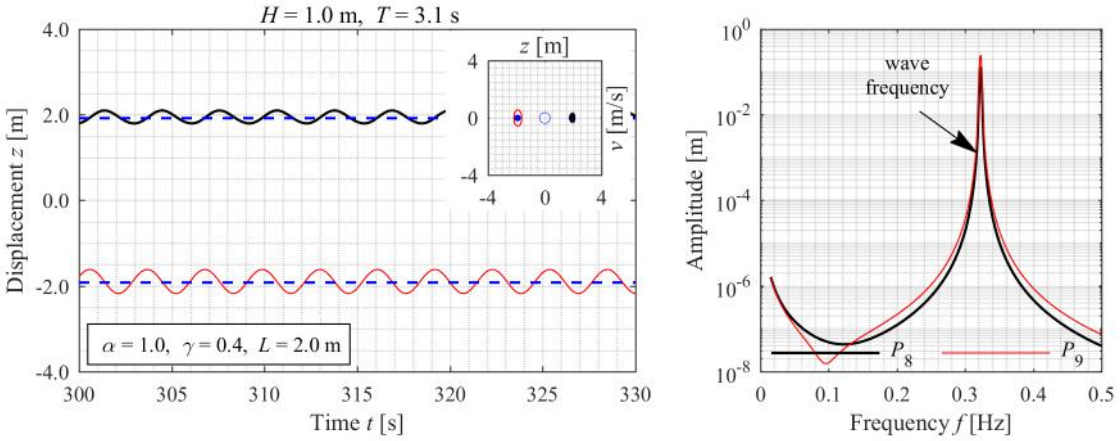

Figure 4.20: Analytical nonlinear model results ($H = 1.0\,\text{m}$, $T = 3.1\,\text{s}$, $B_{PTO} = 30\,\text{kNs/m}$): displacements, phase portraits, and spectrum

The continuous increase of wave height up to $H = 2.0\,\text{m}$, improved the convergence of the linear model in the region with high CWR values (as in the case P_{15}, Figure 4.22). However, larger errors between meshing and analytical approaches appear in the short wave region where the wave steepness is high.

Despite the higher wave height increases the probability of occurrence of the "inter-well" motion, most of the motion behaves as they are in the "intra-well" mode.

As the buoy moves around stable equilibrium positions for the "intra-well" cases, the hydrodynamic characteristics evaluated at the fixed position ($z = 0$) are no

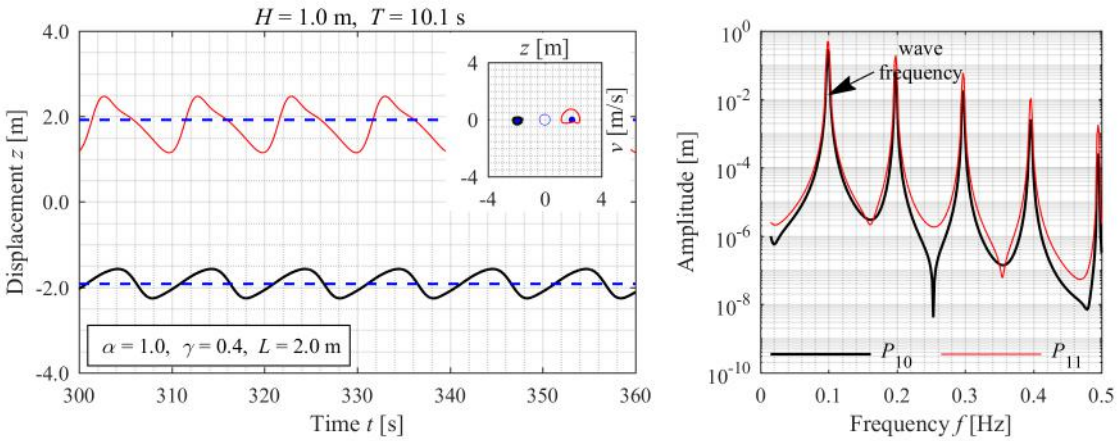

Figure 4.21: Analytical nonlinear model results ($H = 1.0\,\text{m}$, $T = 10.1\,\text{s}$, $B_{PTO} = 30\,\text{kNs/m}$): displacements, phase portraits, and spectrum

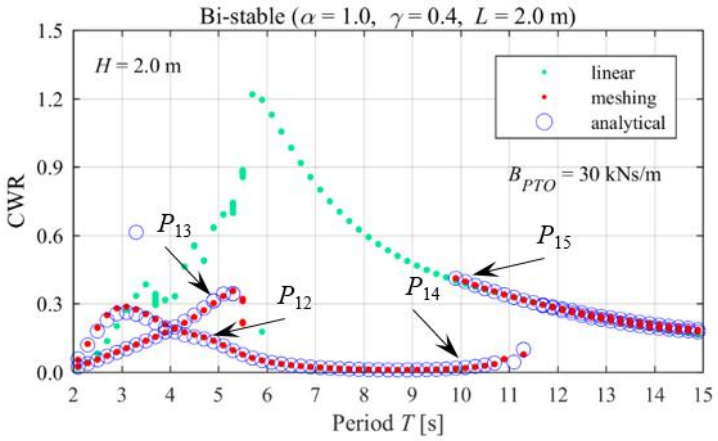

Figure 4.22: Sphere CWR with NSMc: bi-stable configuration ($H = 2.0\,\text{m}$, $B_{PTO} = 30\,\text{kNs/m}$)

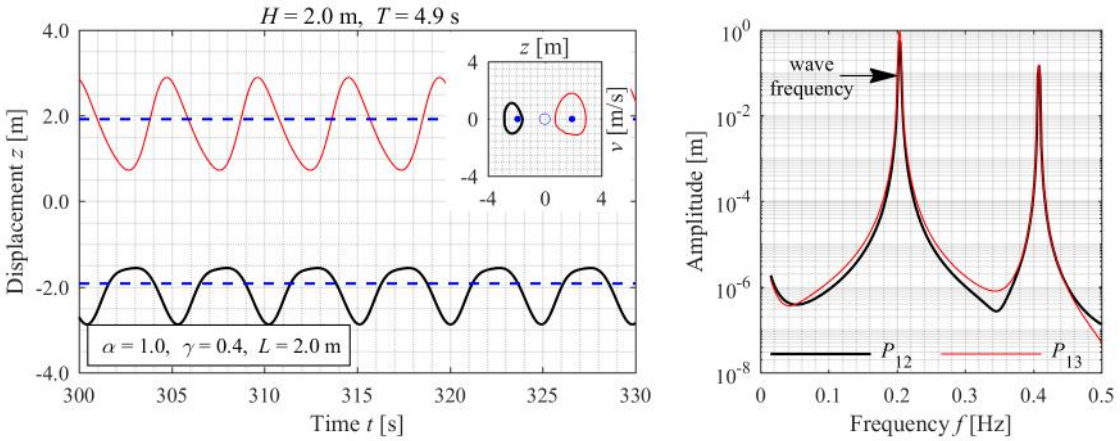

Figure 4.23: Analytical nonlinear model results ($H = 2.0\,\text{m}$, $T = 4.9\,\text{s}$, $B_{PTO} = 30\,\text{kNs/m}$): displacements, phase portraits, and spectrum

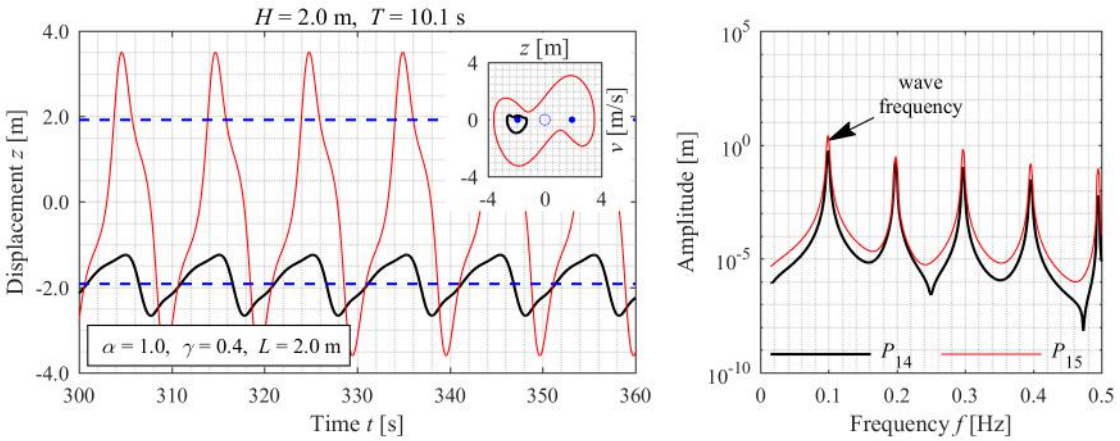

Figure 4.24: Analytical nonlinear model results ($H = 2.0$ m, $T = 10.1$ s, $B_{PTO} = 30$ kNs/m): displacements, phase portraits, and spectrum

longer valid. Not to mention that there exist two or more different motion behaviors for one wave condition.

More importantly, the present bi-stable configuration simulated with the nonlinear Froude-Krylov force model does not show any significant improvements when compared with the model without NSMc also simulated using the the nonlinear approach (see Figures 4.13 and 4.14). It imposes that such bi-stable configurations are not an as attractive choice for WEC applications even considering additional nonlinear Froude-Krylov force. Thus, the attention should move towards the other two types of systems as discussed in the following sections.

QZS configuration

The QZS configuration is imposed by defining the parameters: $\alpha = 1.0$, $\gamma = 0.5$ and $L = 2.0$ m. Figure 4.25 presents the corresponding CWR results. They are more regular than those obtained for the bi-stable system, especially, for the nonlinear model with a relatively small B_{PTO} (10 kNs/m). At the same time, the responses calculated by the nonlinear model (red dots and blue circles) are also closer to the linear model responses (green dots). Therefore, it would be more suitable to compare the influence of the nonlinear model versus the linear model than the bi-stable situation.

Due to the non-uniform waterplane area of the sphere, the nonlinear static restoring force pushes the CWR peak period further away from its natural period than the linear model; while the corresponding peak value becomes a little smaller.

In Figure 4.25, there is an evident change of CWR as obtained from the linear model at $T = 5.2$ s and from the nonlinear model at $T = 5.8$ s. Such a "jump" phenomenon breaks the CWR curve into a low-energy branch (left) and a high-energy branch (right). To check the corresponding motion behavior, two points

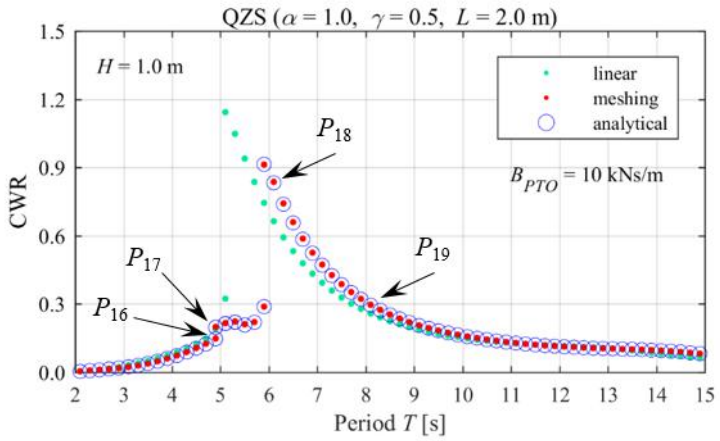

Figure 4.25: Sphere CWR with NSMc: QZS configuration ($H = 1.0$ m, $B_{PTO} = 10$ kNs/m)

on each branch are selected for further investigation as shown from Figure 4.26 to Figure 4.28.

For P_{16} and P_{17} (see Figure 4.26), the displacement and amplitude spectrum show that the period of motion will be twice the wave period. Such a motion is defined as period-2 motion, while the motion periods of P_{18} (see Figure 4.27) and P_{19} (see Figure 4.28), namely period-1 motion, are both equal to the wave period. From the phase portraits, diagram, the period-1 motion features a relatively broader range of motion if compared to the period-2 motion; correspondingly, the CWR is much larger as well.

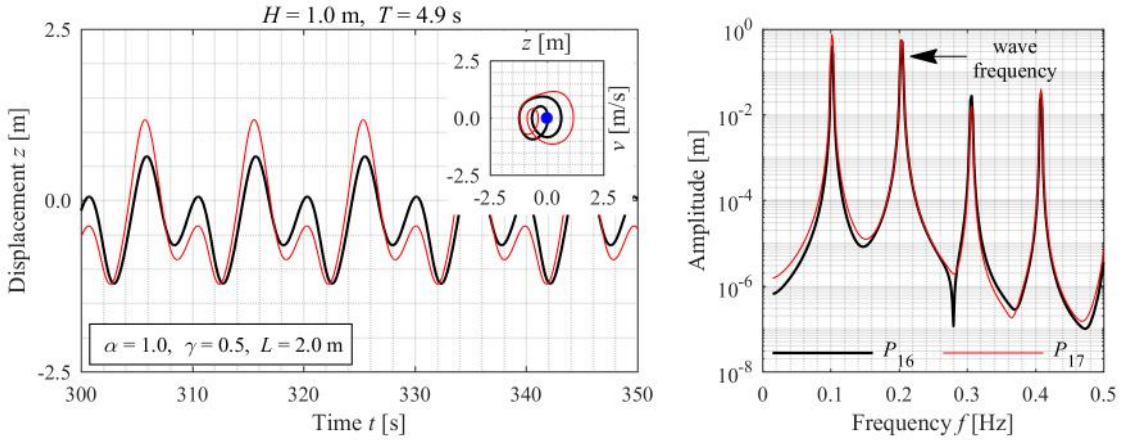

Figure 4.26: Analytical nonlinear model results ($H = 1.0$ m, $T = 4.9$ s, $B_{PTO} = 10$ kNs/m): displacements, phase portraits, and spectrum

Furthermore, one similar period-3 motion is observed on the lower branch for $H = 2.0$ m (see Figure 4.30). In the present QZS analysis, fewer multiple solutions appear, simultaneously, around $T = 5.2$ s.

On the other hand, continuously B_{PTO} increasing (from 30 to 90 kNs/m with

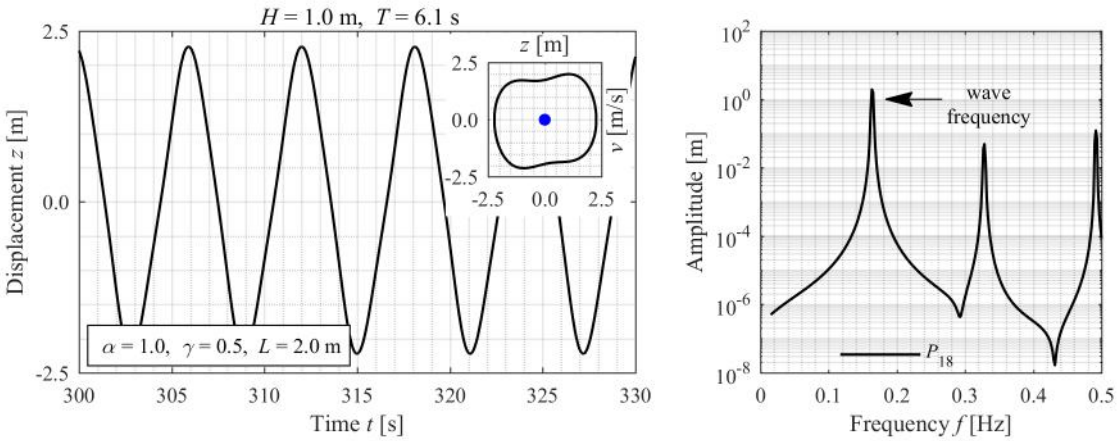

Figure 4.27: Analytical nonlinear model results ($H = 1.0$ m, $T = 6.1$ s, $B_{PTO} = 10$ kNs/m): displacement, phase portrait, and spectrum

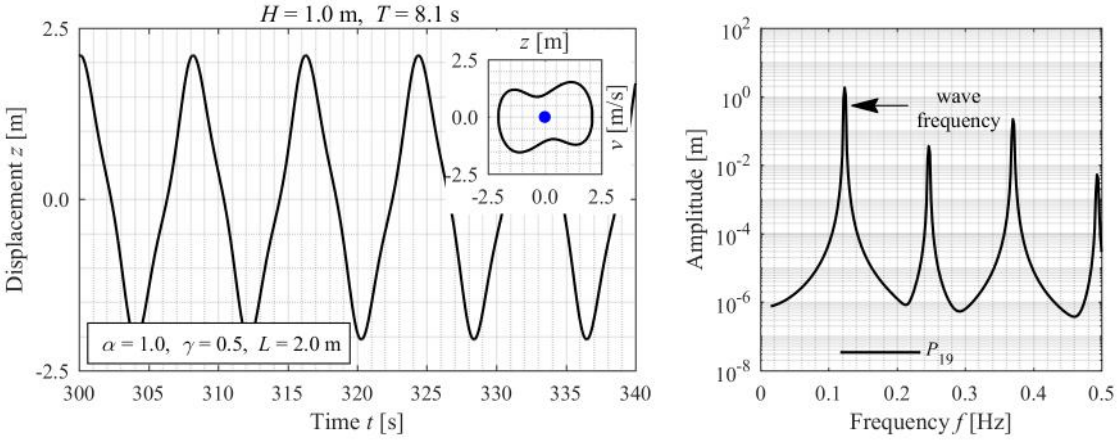

Figure 4.28: Analytical nonlinear model results ($H = 1.0$ m, $T = 8.1$ s, $B_{PTO} = 10$ kNs/m): displacement, phase portrait, and spectrum

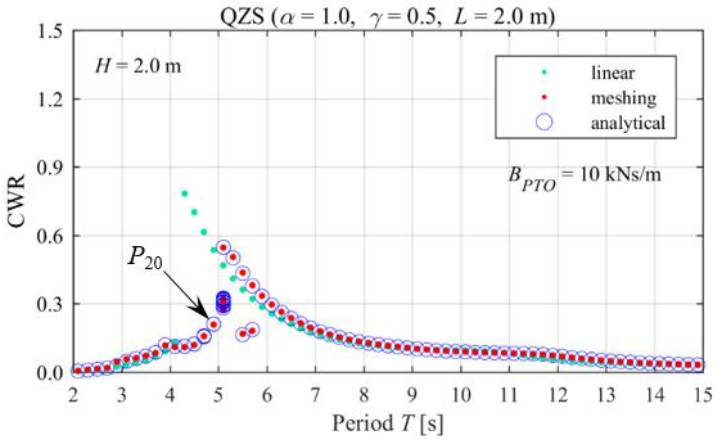

Figure 4.29: Sphere CWR with NSMc: QZS configuration ($H = 2.0$ m, $B_{PTO} = 10$ kNs/m)

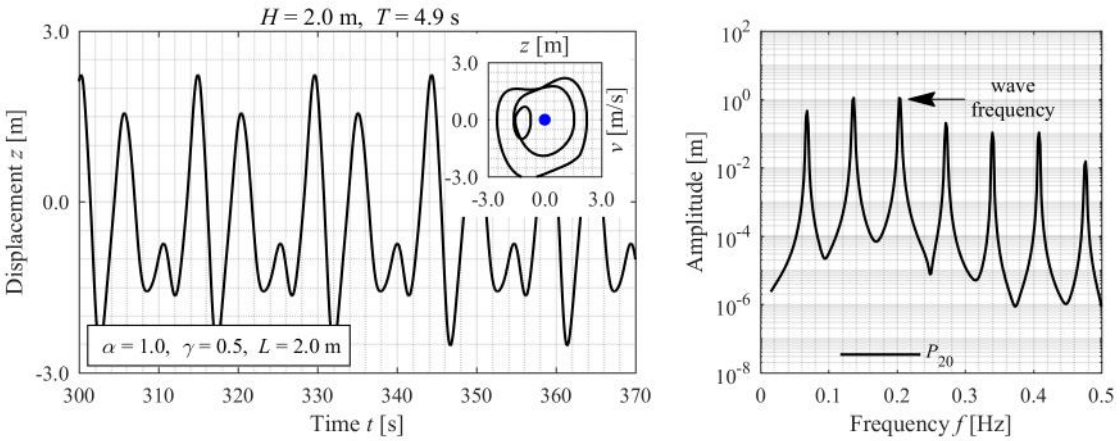

Figure 4.30: Analytical nonlinear approach results ($H = 2.0$ m, $T = 4.9$ s, $B_{PTO} = 10$ kNs/m): displacement, phase portrait and spectrum

20 kNs/m interval), the corresponding CWR curves becomes single-valued (see Figures 4.31 and 4.32), meaning that the random choice of initial conditions does not affect the motion behavior. Due to the consistency observed between meshing and analytical approaches, only the analytical approach results of the nonlinear model are presented (blue solid curves).

The corresponding CWR peak reaches the highest value at $B_{PTO} = 30$ kNs/m. Consequently, CWR decreases gradually as B_{PTO} increases, while broadening the bandwidth and the CWR peak period becomes longer. Such characteristics are very beneficial for small PA working in wave conditions with longer periods than its own natural period. Additionally, the CWR in the downward branch calculated by the nonlinear model is a little higher than that from the linear model. Due to the nonlinear Froude-Krylov force, the period of the optimal CWR peak value increases if compared to those calculated by the linear model, whereas is not significant for the previously discussed bi-stable configuration.

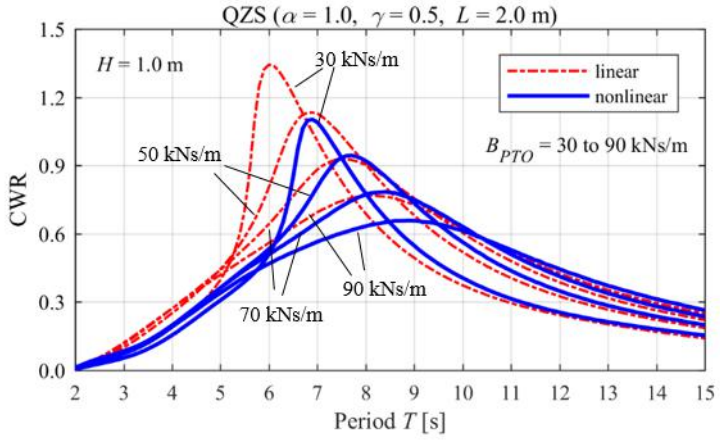

Figure 4.31: Sphere CWR with NSMc: QZS configuration ($H = 1.0$ m)

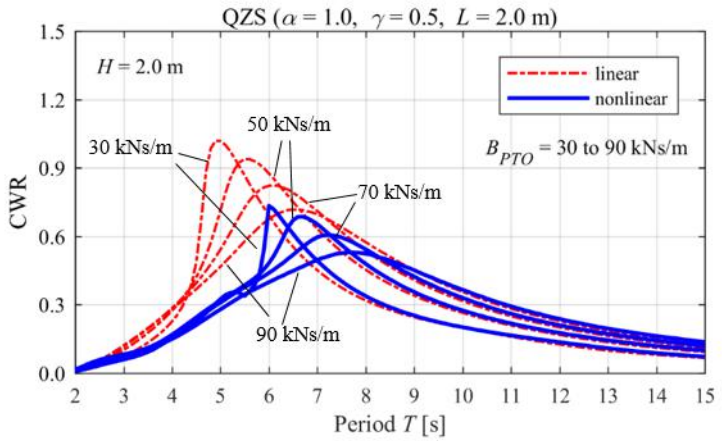

Figure 4.32: Sphere CWR with NSMc: QZS configuration ($H = 2.0$ m)

For the QZS configuration, increasing the wave height lowers the optimal CWR and shortens the corresponding period. It means that the QZS configuration plays a better role for the relatively small wave height, as the peak CWR value and corresponding period shown in Figure 4.33.

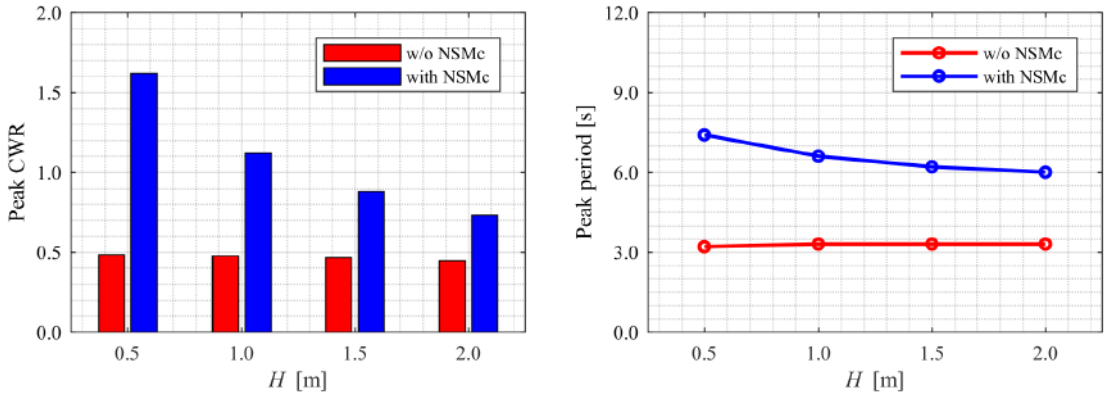

(a) (b)

Figure 4.33: NSMc effects on the peak CWR and period for different wave heights: QZS configuration

The QZS configuration shows some practical advantages as it broadens the response bandwidth, pushes the resonant response to longer wave ranges and improves the final optimal response. The next section presents a similar analysis featuring the mono-stable behavior.

Mono-stable configuration

Increasing the geometry ratio to $\gamma = 0.6$ adjusts a mono-stable configuration ($\alpha = 1.0$, $\gamma = 0.6$ and $L = 2.0$ m) is obtained. The CWR patterns are quite similar to the QZS configuration. Therefore, only Figure 4.34 will be necessary to describe its

most relevant characteristics. The mono-stable configuration reduces the differences in the results between linear and nonlinear models. In addition, the CWR peak from the nonlinear model decreases, moving towards longer waves. However, the final performance is still better than for the buoy without NSMc in long wave conditions.

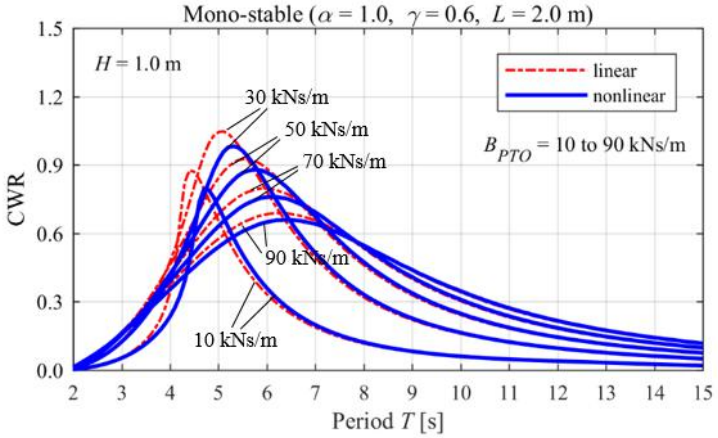

Figure 4.34: Sphere CWR with NSMc: mono-stable configuration I ($H = 1.0$ m)

For another mono-stable configuration ($\alpha = 1.1$, $\gamma = 0.5$ and $L = 2.0$ m) which leads to $C_\gamma = 1.05$, being smaller than for the previous configuration, the CWR patterns (in Figure 4.35) are much closer to the QZS configuration under the same wave height. From those observations, one may draw the following conclusions for the mono-stable configuration:

- the smaller is C_γ, the closer to the QZS performance it behaves;
- increasing C_γ weakens the role of NSMc.

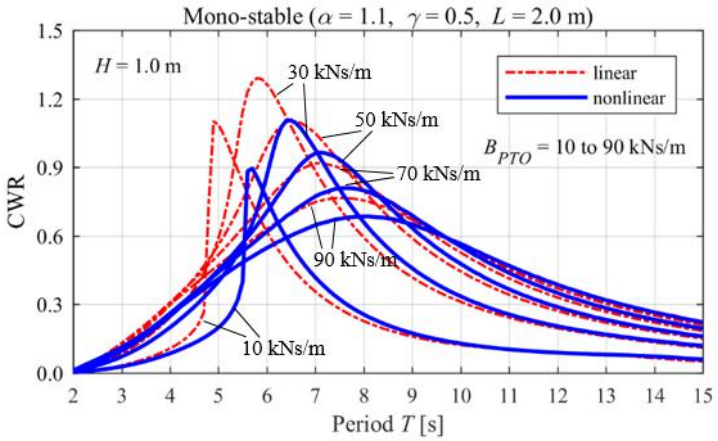

Figure 4.35: Sphere CWR with NSMc: mono-stable configuration II ($H = 1.0$ m)

4.4 Summary

The present chapter discussed the fundamental characteristics of the classical NSS with mechanical compression springs (NSMc) and investigated comprehensively its complex dynamic behavior. The NSMc model set up considered the additional constraint of the effective excursion. The static analysis explored the specific characteristics involved in bi-stable, QZS and mono-stable configurations. Further motion investigations considering different configurations attempted to bring some light on the advantages and specific benefits from applying NSMc into the WEC buoy dynamics, such as:

- increasing the resonance period;
- broadening the frequency response bandwidth;
- improving the optimal wave energy capturing performance.

Compared with the bi-stable system, the QZS and mono-stable configurations performed much better motion stability and wave energy capturing characteristics, becoming potential choices for the applications in wave energy conversion. In the next chapter, deeper discussions focus on the QZS and mono-stable configurations.

Comparisons with each other showed the relative merits and accuracy related to the linear and nonlinear model results. Especially, the results obtained by applying the very efficient analytical approach showed a great deal of consistency if compared to the more reliable meshing approach, when waves are too steep. The nonlinear model indeed presented significant differences with respect to the linear model, such as,

- motion behavior of the bi-stable configuration presented difficulties to escape from the potential wells;
- optimal CWR decreased, however, the corresponding wave period increased.

The research in the present chapter attempted to establish solid foundations for further investigations to be developed in the following chapters.

Chapter 5

NSMc in WEC: Practical Considerations

Based on the analysis of the combined system of the WEC buoy and NSMc in Chapter 4, NSMc presents three distinct types of special behaviors. Especially, the QZS and mono-stable configurations can broaden the response bandwidth and increase the natural period in a relatively stable way. It follows that the performance of the combined system could be well explored in irregular wave conditions. This chapter also investigates important aspects related to the feasibility of NSMc based on some practical considerations of the physical characteristics of the mechanical compression springs.

5.1 Irregular wave conditions

This section introduces the characteristics related to the irregular wave spectrum adopted in the present analysis. In irregular wave conditions, the analytical approach used to calculate the nonlinear Froude-Krylov force deserves further special considerations.

5.1.1 spectrum

In according to the DNV-RP-C205 standard [113], the following expression describes the well-known JONSWAP sea spectrum,

$$S_J(\omega) = A_\gamma S_{PM}(\omega)\gamma^{\exp\left(-\frac{1}{2}(\frac{\omega-\omega_P}{\sigma\omega_P})^2\right)} \tag{5.1}$$

$$S_{PM}(\omega) = \frac{5}{16}H_S^2\omega_P^4\omega^{-5}\exp\left(-\frac{5}{4}(\frac{\omega}{\omega_P})^{-4}\right) \tag{5.2}$$

where: $S_J(\omega)$ – JONSWAP spectrum;

$S_{PM}(\omega)$ – Pierson-Moskowitz spectrum;

γ – non-dimensional peak shape parameter (Note: γ represents the peak shape parameter only in the present sub-section), with average value $\gamma = 3.3$;

σ – spectral width parameter, with average values:

$$\sigma = \begin{cases} 0.07 & \omega \leq \omega_P \\ \\ 0.09 & \omega > \omega_P \end{cases} \tag{5.3}$$

A_γ – normalizing factor, defined as:

$$A_\gamma = 1 - 0.287 \ln(\gamma) \tag{5.4}$$

The JONSWAP spectrum based on the averaged parameters is expected to provide a reasonable representation if,

$$3.6 < \frac{T_P}{\sqrt{H_S}} < 5.0 \tag{5.5}$$

$$\text{or} \quad 0.02562 < S_P = 2\pi \frac{H_S}{g T_P^2} < 0.04942 \tag{5.6}$$

where: S_P – average wave steepness in irregular wave conditions.
And outside of this interval, if,

$$\frac{T_P}{\sqrt{H_S}} \geq 5.0 \tag{5.7}$$

$$\text{or} \quad S_P = 2\pi \frac{H_S}{g T_P^2} \leq 0.02562 \tag{5.8}$$

the JONSWAP spectrum reduces to the Pierson-Moskowitz spectrum with $\gamma = 1.0$. Thus, the Pierson-Moskowitz spectrum is considered as one special case of the JONSWAP spectrum.

The JONSWAP spectrum discretized by $N_\omega = 500$ equidistant frequencies, ranging from $0.4\omega_P$ to $3.4\omega_P$, defines the times series representing the irregular wave records. The cut-off frequency in the high-frequency side truncates only less than 1% of the total energy covered by the spectrum. To avoid the undesirable period $2\pi/\triangle\omega$, the representative circular frequency is defined as [114]:

$$\omega_i = \hat{\omega}_i - 0.5 \triangle\omega \cdot \text{rand} \tag{5.9}$$

where: $\hat{\omega}_i$ – intermediate circular frequency at each frequency interval;

rand – one of the random numbers uniformly distributed in the range between 0 and 1.

Table 5.1 lists all irregular wave conditions considered for the corresponding three different average steepness $S_P = 0.010, 0.018, 0.025$.

Table 5.1: Irregular wave conditions

	T_P [s]	4.0	5.0	6.0	7.0	8.0	9.0	10.0	11.0	12.0
$S_P = 0.010$	H_S [m]	0.25	0.39	0.56	0.77	1.00	1.26	1.56	1.89	2.25
$S_P = 0.018$	H_S [m]	0.45	0.70	1.01	1.38	1.80	2.28	2.81	3.40	4.05
$S_P = 0.025$	H_S [m]	0.62	0.98	1.41	1.91	2.50	3.16	3.90	4.72	5.62

As shown in Figure 5.1, the irregular wave condition, $H_S = 2.5\,\text{m}$ and $T_P = 8.0\,\text{s}$, with a given target Power Spectrum Density (PSD), wave elevation records and the corresponding PSD generated through the Fast Fourier Transform – FFT. The total length of the record is 2300 s (with sampling frequency: $f_S = 100$ Hz) with the first 300 s (t_r) truncated and excluded from the analysis due to the initial transient phenomenon expected in the numerical simulation. The next section describes the corresponding convergence analysis that supports the truncation length choice.

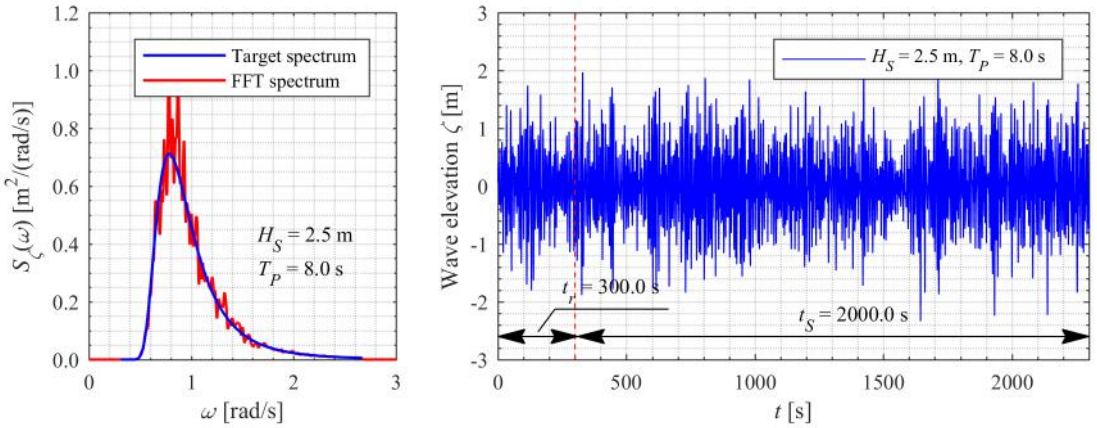

Figure 5.1: Irregular wave spectrum and wave elevation ($H_S = 2.5\,\text{m}$, $T_P = 8.0\,\text{s}$)

5.1.2 Nonlinear Froude-Krylov force

In irregular wave conditions, the nonlinear Froude-Krylov force model should be considered carefully. Applying the linear superposition theory to generate one irregular wave condition requires a great number of frequency components. As the nonlinear Froude-Krylov force changes with the buoy relative displacement, the linear wave superposition method directly applied to the analytical approach at each time step increases the computational efforts tremendously. The meshing approach which incorporates one additional dimension to the mesh would be even worse.

Following the derivations of nonlinear Froude-Krylov force in Chapter 3, the parameters – N_J and N_E, adopted in the present work, are listed in Table 5.2 by splitting the peak period T_P (or peak frequency ω_P) range into four regions.

Table 5.2: Polynomial fittings of $J_0(kR\sqrt{1-x^2})$ and e^{kRx}

T_P [s]	ω [rad/s]	kR [−]	N_Jth order	N_Eth order
≥ 7.0	3.05	2.37	4	5
≥ 6.0	3.56	2.23	6	7
≥ 5.0	4.27	4.65	8	9
≥ 4.0	5.34	7.27	10	11

Note: $\omega = 3.4 \cdot \omega_P$, corresponds to the highest frequency component considered in generating irregular wave series.

5.2 Convergence analysis in irregular waves

This section conducts the convergence analysis of the relevant parameters adopted in the simulation for irregular wave conditions. The analysis ensures adequate convergence for both cases: without and with NSMc.

5.2.1 Case without NSMc

First, the convergence analysis at the simulation time t_S features an irregular wave condition with a high steepness $S_P = 0.025$ when more significant nonlinearity is expected.

Figure 5.2 (a) shows the patterns of CWR with B_{PTO} under short, medium and long wave conditions (with effective simulation time $t_S = 2000$ s and sampling frequency $f_S = 100$ Hz). The solid curves represent the mean values of CWR for 50 different irregular waves defined by the same sea spectrum (therefore, with the same statistic properties) but distinct sets of random phases. Actually, there exists a shaded area defined by a given standard deviation range above and below each solid curve. However, in the present case, it is not noticeable because the solid curves overlapping the small differences. Note that as the wave period increases, the CWR changes with B_{PTO} become moderate and the corresponding optimal damping increases. The peaks of the solid curves, marked by three red points, represent points for different wave conditions. Figure 5.2 (b) depicts their changes with t_S where three solid curves show the patterns of mean CWR with respect to t_S and the colorful dashed curves describe the corresponding coefficient of variation (COV) for the maximum CWR.

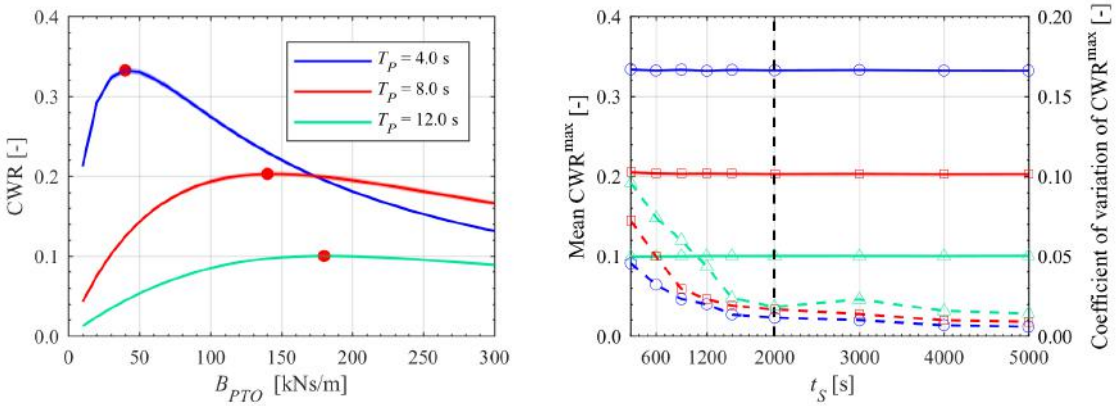

(a) (b)

Figure 5.2: Convergence analysis of the simulation length (t_S) for sea state: $S_P = 0.025$, $T_P = 4.0,\ 8.0,\ 12.0$ s

COV defines the ratio of standard deviation to the mean value. Values smaller than 3% for $t_S = 2000$s indicate that the data obtained from the 50 different irregular wave conditions defined by different random phase angles are stable and their mean values could be taken as the representative values to evaluate the corresponding system performance.

Based on the results from the convergence analysis, the WEC without NSMc could be submitted to a comprehensive simulation program. From Figure 5.3 to Figure 5.5, they describe the CWR obtained in both linear (black curves) and nonlinear (blue circles) models. The red curves present the differences (Diff_3) between two models.

$$\text{Diff}_3 = \frac{\text{CWR}_{\text{linear}} - \text{CWR}_{\text{nonlinear}}}{\text{CWR}_{\text{linear}}} \times 100\% \tag{5.10}$$

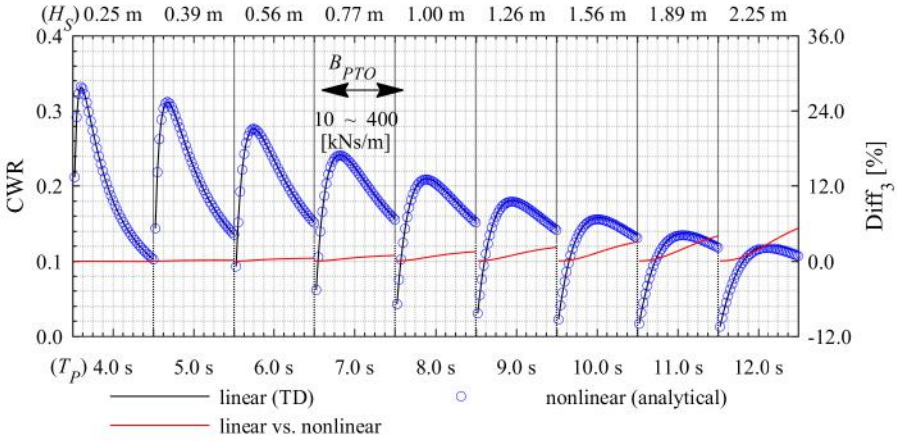

Figure 5.3: Linear and nonlinear models: CWR for wave steepness $S_P = 0.010$

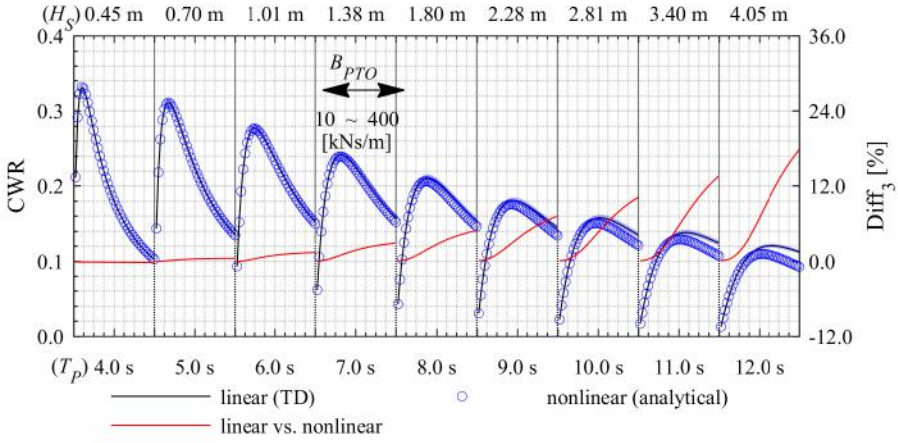

Figure 5.4: Linear and nonlinear models: CWR for wave steepness $S_P = 0.018$

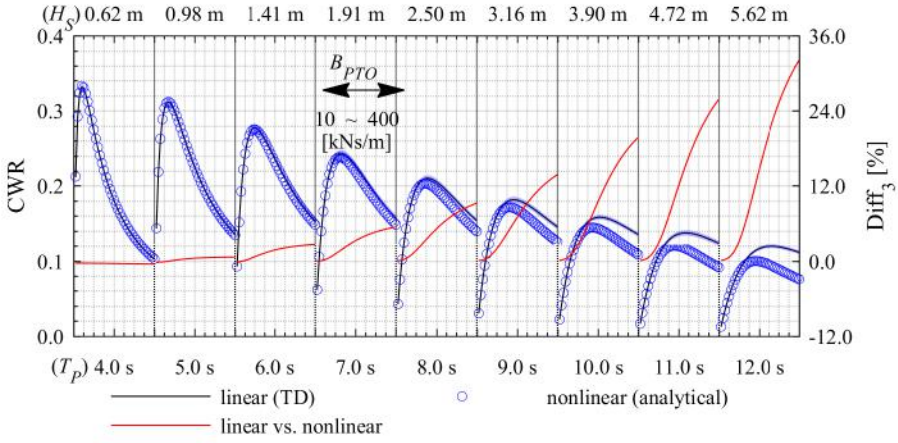

Figure 5.5: Linear and nonlinear models: CWR for wave steepness $S_P = 0.025$

In each figure, the differences become more evident as the wave period increases, as well as the wave height increases. In general, the results from the nonlinear model are smaller than from the linear model in the higher damping range.

Comparing the three figures, the CWR from the linear model (black curves) almost does not change with wave steepness complying with the fundamental properties of the linear model. Moreover, in the nonlinear model, the CWR decreases with wave steepness increasing.

The above simulation conditions do not cover the sphere natural period. The occurrence probability for short wave in real seas is quite low. Following the results from Chapter 4, one infers that the differences in short wave conditions are not significantly. On the other hand, to keep the accuracy of the analytical nonlinear model, short wave conditions require extra terms, increasing the computational efforts significantly. Thus, the present section avoids considering very short wave simulations.

To distinguish the results for the three different wave steepness conditions, the

mean power absorption P_m replaces the CWR when comparing meshing and analytical results for the optimal B_{PTO} (see Figure 5.6). The good agreement validates the use of the analytical approach in irregular wave conditions. Simultaneously, Figures 5.7 and 5.8 also confirm the consistency of the predicted motion using both approaches.

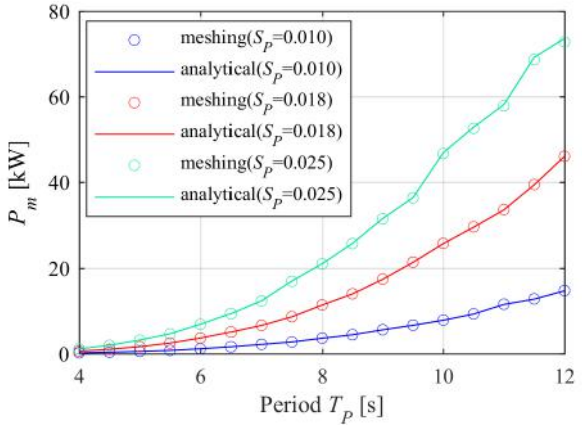

Figure 5.6: Meshing and analytical nonlinear models: mean power comparison

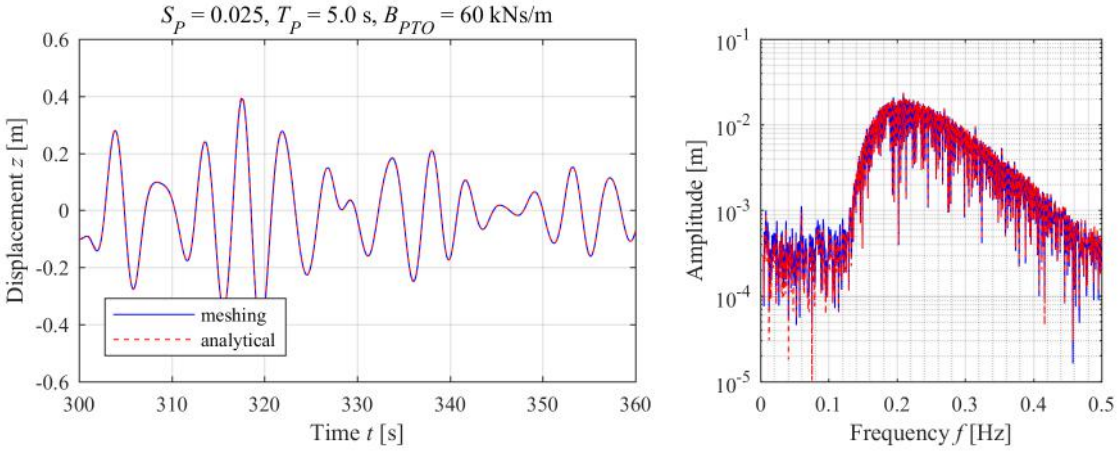

Figure 5.7: Meshing and analytical nonlinear models: displacement and amplitude spectrum($S_P = 0.025$, $T_P = 5.0\ s$)

In Figures 5.9 and 5.10, they describe the comparisons of wave excitation force series under two different wave conditions in detail. The relatively evident difference between the linear and nonlinear wave excitation force can be found in the peak/trough regions, especially for the case with a longer wave (in Figure 5.10). Thus, the CWR difference can be expected to become more obvious. Such a phenomenon is also consistent with the discoveries in Figure 5.5, which can be attributed to the amplification of nonlinearity excited by the high wave.

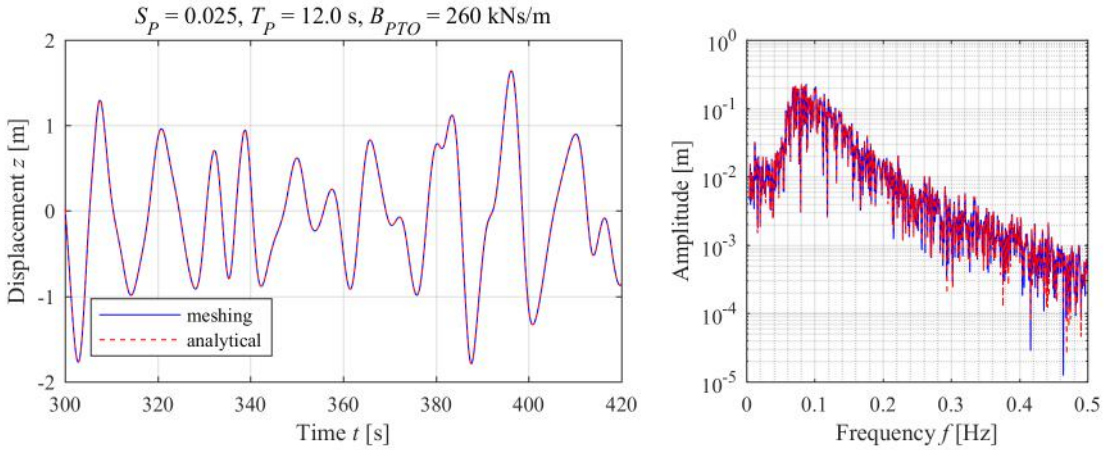

Figure 5.8: Meshing and analytical nonlinear models: displacement and amplitude spectrum ($S_P = 0.025$, $T_P = 12.0\ s$)

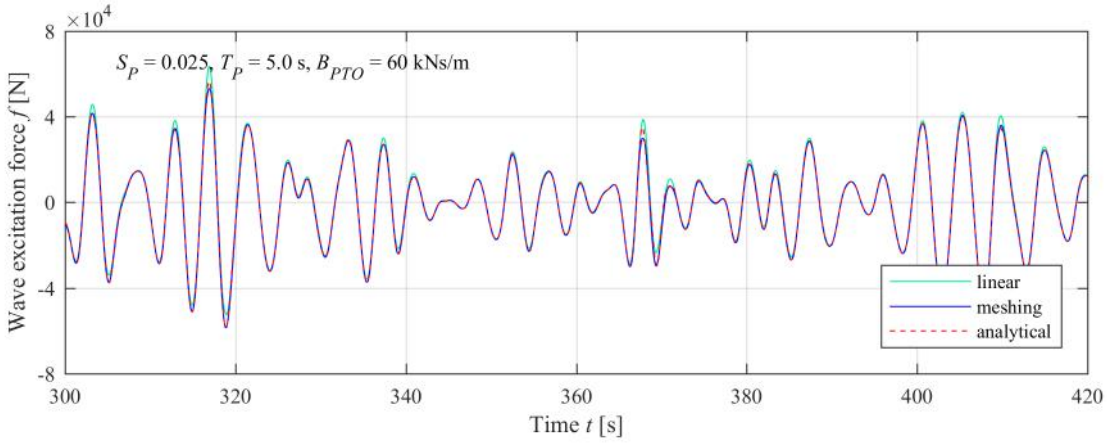

Figure 5.9: Linear, meshing and analytical nonlinear models: wave excitation force ($S_P = 0.025$, $T_P = 5.0\ s$)

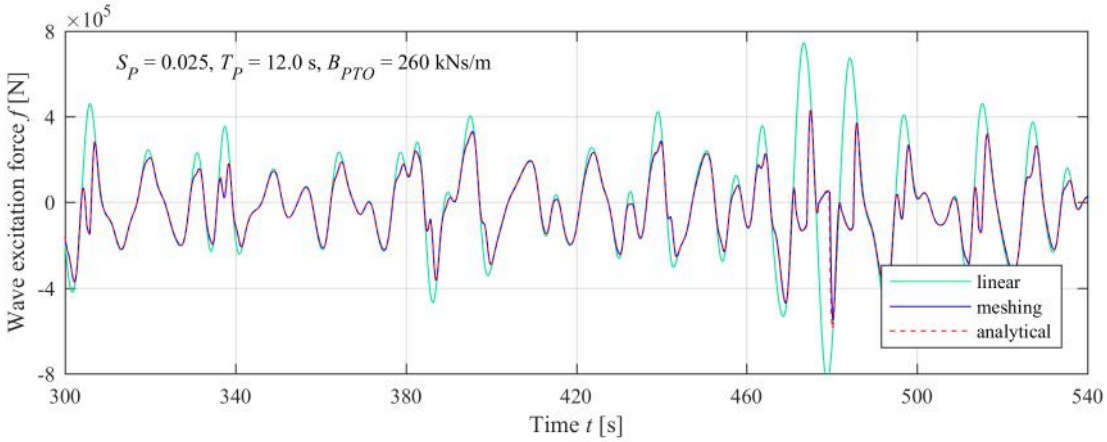

Figure 5.10: Linear, meshing and analytical nonlinear models: wave excitation force ($S_P = 0.025$, $T_P = 12.0\ s$)

5.2.2 Case with NSMc

Similar to the discussion presented in sub-section 5.2.1, this sub-section discusses the convergence analysis of the time length t_S for different NSMc configurations.

First, Figure 5.11 shows the pattern of CWR with B_{PTO} for the bi-stable system ($\alpha = 1.0$, $\gamma = 0.4$, $L = 2.0$ m). The solid curves and shaded area follow a similar definition as in Figure 5.2 (a). In addition, the scatters show the CWR data related to the 50 different irregular waves generated by different random phase angles. Their distributions show two distinct clusters of CWR appearing for most of the B_{PTO} ranges in the shorter wave condition (blue scatters). A similar phenomenon also appears in the medium length wave condition (red scatters). As analyzed in Chapter 4, the unique characteristic of the bi-stable system explains it. Such a behavior occurs even in irregular wave conditions, causing a larger standard deviation – more evident shaded area.

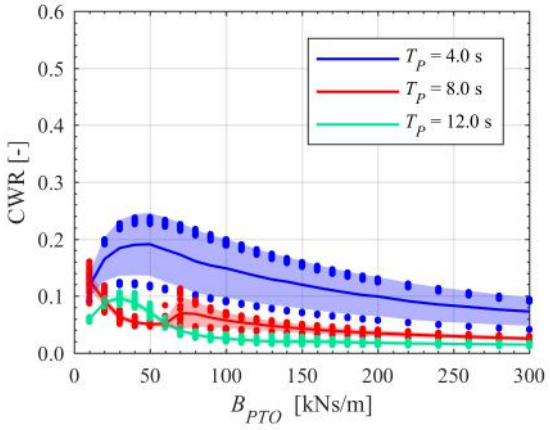

Figure 5.11: Sphere CWR with NSMc: bi-stable configuration ($\alpha = 1.0$, $\gamma = 0.4$, $L = 2.0$ m) for sea state: $S_P = 0.025$, $T_P = 4.0,\ 8.0,\ 12.0$ s

The above multiple solution phenomenon is not adequate for the real sea applications as the randomness makes it difficult to determine when the high-energy branch appears. In other words, the bi-stable system cannot provide the WEC with a reliable solution. Thus, the following simulations for the bi-stable system (based on the mean values) play the role of reference only, but not being considered into the power conversion estimation.

On the contrary, Figures 5.12 and 5.13 show that $t_S = 2000$ s is suitable enough to evaluate the QZS and mono-stable NSMc cases ($C_\gamma \geq 1.0$). Such stable outputs in irregular wave conditions indicate that they deserve further investigations.

Note that the above simulations are all conducted with respect to 50 different groups of random phase angles and fixed initial condition ($z_0 = 0$ and $v_0 = 0$). To investigate the influence of initial conditions on the simulations in irregular wave

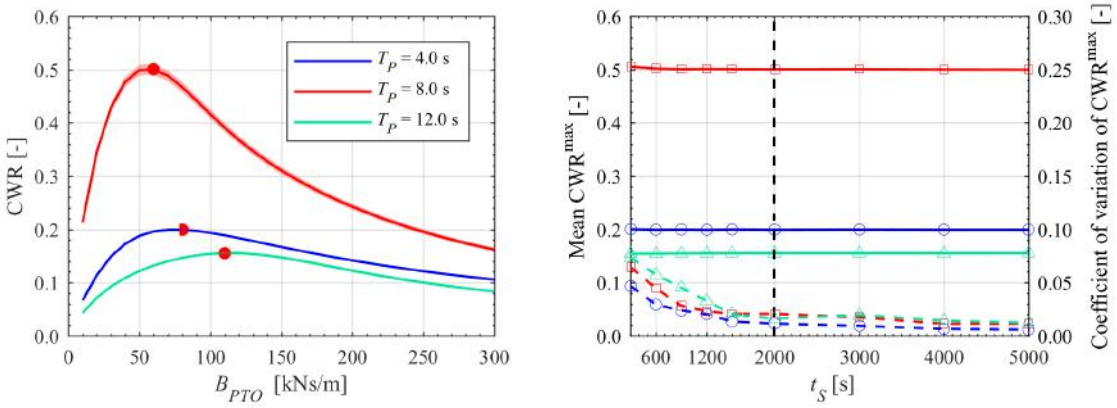

(a) (b)

Figure 5.12: Convergence analysis of the simulation length (t_S) with QZS NSMc ($\alpha = 1.0$, $\gamma = 0.5$, $L = 2.0$ m) for sea states: $S_P = 0.025$, $T_P = 4.0,\ 8.0,\ 12.0$ s

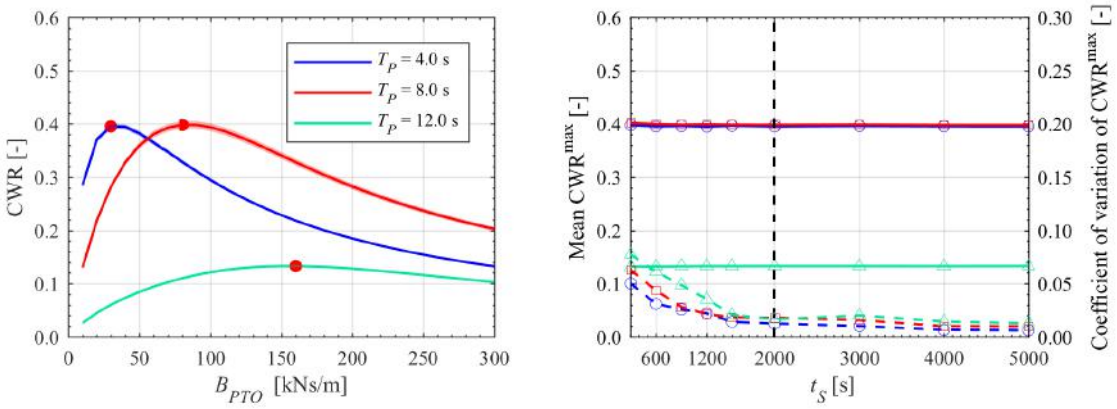

(a) (b)

Figure 5.13: Convergence analysis of the simulation length (t_S) with mono-stable NSMc ($\alpha = 1.0$, $\gamma = 0.6$, $L = 2.0$ m) for sea states: $S_P = 0.025$, $T_P = 4.0,\ 8.0,\ 12.0$ s

conditions, Figure 5.14 compares results from the previous simulation approach – Case I, with the simulation corresponding to 50 different groups of initial conditions ($z_0,\ v_0$) – Case II. Three different sea states ($S_P = 0.025,\ T_P = 4.0,\ 8.0, 12.0$ s) are selected in the comparison for both QZS ($\alpha = 1.0,\ \gamma = 0.5,\ L = 2.0$ m) and mono-stable ($\alpha = 1.0,\ \gamma = 0.6,\ L = 2.0$ m) configurations. The sub-groups – "1", "2" and "3" appearing in the legends correspond to three different wave conditions defined respectively.

The comparisons between Case I and Case II show that considering the random phase effect in irregular wave conditions can cover the influence of initial conditions which lead to distinct motion behavior, in a similar way as observed in the regular wave discussion (see the analysis of QZS and mono-stable configurations in Section 4.3.2). Thus, the following simulations with NSMc in irregular wave conditions

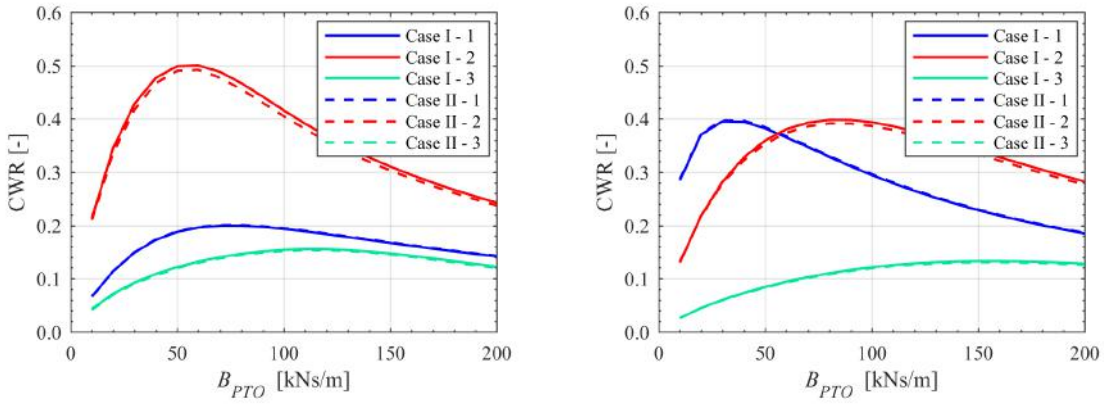

(a) QZS configuration

(b) mono-stable configuration

Figure 5.14: Case I and Case II comparisons: QZS and mono-stable configurations

adopt the same initial condition $z_0 = 0$ and $v_0 = 0$ but now considering 50 different groups of random phase angles.

5.3 Mechanical compression spring constraints

5.3.1 NSMc Feasibility

The conventional design procedure of mechanical springs defines a suitable group of variables (for both geometrical and physical properties) according to some special requirements. The present section discusses the practical limitations and physical constraints of mechanical compression springs, exploring the feasible region of both geometrical and physical variables associated with NSMc. Figure 5.15 presents an illustrative scheme and main dimensions of a typical compression spring.

The following steps describe the sequence to determine the feasible region of the mechanical compression spring design:

Step 1: Define the parameters ranges to be explored – horizontal length of NSMc L; the number of adopted springs n; geometry ratio γ and stiffness ratio α; wire diameter d; and spring index C, as listed in Table 5.3.

The L, γ and α ranges are adjusted according to the analysis presented in the previous section. The d and C ranges are determined based on the characteristics of the material (e.g., hard drawn wire A227) in the fatigue loading [116] considering that the PA oscillates in waves;

Step 2: Derive the basic parameters – stiffness K_0 (in N/m), free length L_0 (in m), coil diameter D (in mm), and curvature correction factor – Bergsträsser

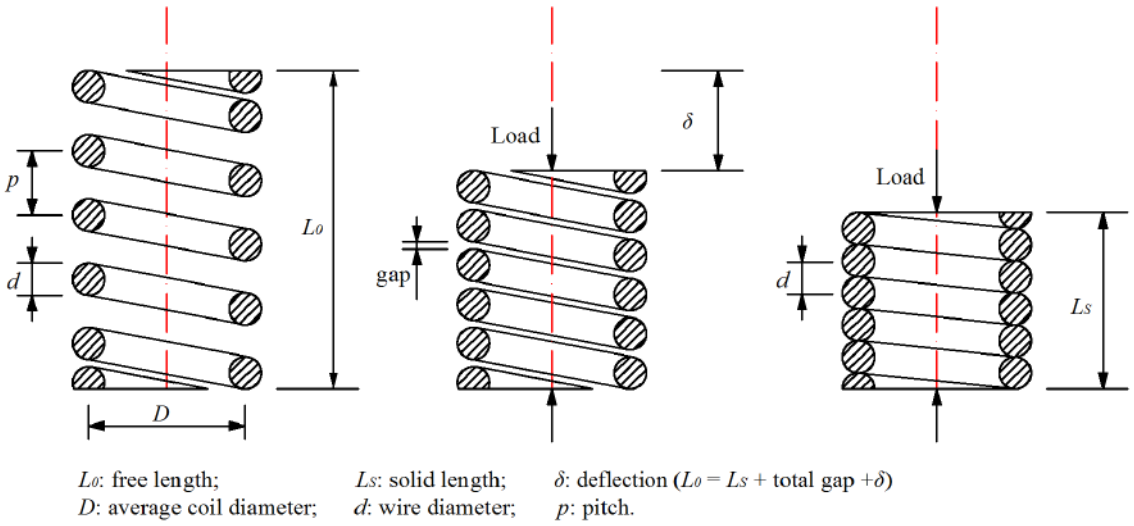

Figure 5.15: Schematic and dimensions of mechanical compression springs (adapted from [115])

Table 5.3: Mechanical compression spring parameters

Parameters	Units/Expressions	Values
L	[m]	/1.0, 1.5, 2.0, 2.5/
n	[-]	/3, 4, 6, 9, 12/
γ	L/L_0	$0.02 \sim 0.98$
α	C_{WL}/nK_0	$1.0 \sim 6.0$
d	[mm]	$3.2 \sim 10.0$
C	D/d	$4.0 \sim 12.0$

factor K_B [116];

$$K_0 = \frac{C_{WL}}{n\alpha} \tag{5.11}$$

$$L_0 = \frac{L}{\gamma} \tag{5.12}$$

$$D = C \cdot d \tag{5.13}$$

$$K_B = \frac{4C + 2}{4C - 3} \tag{5.14}$$

Step 3: Derive the axial load amplitude F_a (in kN), and the number of active coils N_a.

F_a is the average value of the maximum and minimum values of axial load [116]. The NSMc maximum load happens when the spring is at the horizontal equilibrium position and the minimum load is zero, then,

$$F_a = \frac{10^{-3} K_0 (L_0 - L)}{2} \tag{5.15}$$

The number of active coils N_a can be obtained according to the expression of stiffness,

$$K_0 = \frac{10^3 G d}{8 C^3 N_a} \tag{5.16}$$

where: shear modulus $G = 78603.0$ MPa.

Step 4: The above variables allowing for calculating the parameters: shear stress amplitude τ_a (in MPa), solid length L_S (in mm), and pitch p (in mm) for the squared and ground end.

$$\text{Maximum stress: } \tau_a = K_B \cdot \frac{8 F_a C}{\pi d^2} \cdot 10^3 \tag{5.17}$$

$$\text{Solid length: } L_S = (N_a + 2) d \tag{5.18}$$

$$\text{pitch: } p = \frac{10^3 L_0 - 2d}{N_a} \tag{5.19}$$

The conditions of stability and critical frequency are not considered. Because buckling can be avoided for long springs if guided by a sleeve or over an arbor [117].

Step 5: Constraints: first, the maximum stress τ_a should satisfy the strength condition:

$$\tau_a \leq \frac{S_{sa}}{n_f} \tag{5.20}$$

where, S_{sa} is the torsional endurance strength for infinite life. For the peened spring, $S_{sa} = 398$ MPa [116], and the safety factor $n_f = 1.5$.

Accordingly, the minimum total axial gap should be taken as 15% (c_{gap}) of the maximum deflection (δ_{max}) [117],

$$L_0 = L_S \times 10^{-3} + \text{total gap} + \delta_{max} \tag{5.21}$$

$$\text{total gap} = c_{\text{gap}} \cdot \delta_{max} \tag{5.22}$$

$$L_0 - L \leq \delta_{max} \tag{5.23}$$

the solid length L_S should satisfy the following relationship,

$$L_S + (1 + c_{\text{gap}}) \cdot (L_0 - L) \cdot 10^3 \leq L_0 \cdot 10^3 \tag{5.24}$$

Finally, the preferable pitch p should not be greater than half of the coil diameter,

$$d < p \leq 0.5D \tag{5.25}$$

The feasible parameters corresponding to the solution that simultaneously satisfy all the constraints defined in Step 5 – Eqs. 5.20, 5.24 and 5.25.

Figure 5.16 presents the feasible regions of (α, γ) with different (L, n) configurations, defined by following the recommendations described in the above steps. Each sub-graph corresponds to one group of (L, n) configuration, and defines the horizontal axis as α and the vertical axis as γ respectively. The black curve divides the (α, γ) domain into feasible (green) and unfeasible (white) regions. The blue and red dashed curves divide each sub-graph at $C_\gamma = 1$ and $C_\gamma = 2$. The parameters around $C_\gamma = 1$ or a least $C_\gamma < 2$ define the QZS or mono-stable configurations that are attractive for the wave energy conversion based on the previous analysis.

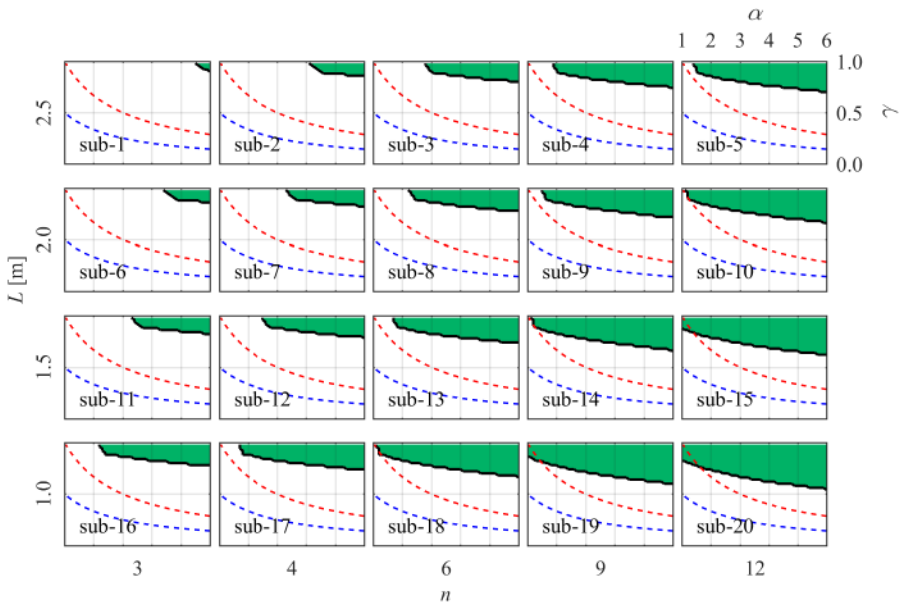

Figure 5.16: NSMc feasible regions

From the results observed in Figure 5.16, one may conclude that,

- In the lower range of α and γ for a fixed L,the larger the number of springs n, the broader the feasible region;
- For a fixed n, the shorter the horizontal length L, the lower the bound limit of γ and the broader the feasible region.

In other words, more springs and shorter horizontal length lead to more feasible configurations. Sub-graphs sub-16 and sub-8, or sub-18 and sub-10 allow for another interesting conclusion: the same feasible regions there exist if L/n for different configurations is kept constant,

$$\frac{L_{16}}{n_{16}} = \frac{L_8}{n_8} = \frac{1}{3} \text{ or } \frac{L_{18}}{n_{18}} = \frac{L_{10}}{n_{10}} = \frac{1}{6} \tag{5.26}$$

where: subscript number defines the corresponding sub-graph.

The practical selection of mechanical compression springs may benefit from using the constant values defined by the above relationship.

In addition, the feasible values for the parameters (α, γ) occupy the top-right region of each sub-graph, meaning that

- determination of (α, γ) indeed requires to observe the constraints limitation;
- in practice, it is rather difficult to obtain a feasible configuration for lower α and γ values.

The present distribution characteristics of the feasible NSMc configurations imposes a significant limitation in the enhancement of power capture with NSMc. The next sub-section consequently will investigate such a limitation in detail.

5.3.2 Feasible NSMc performance

To work in a realistic scenario, the evaluation of the sphere performance with NSMc considers the sea site in the nearshore region of Rio de Janeiro, Brazil. Table 5.4 lists the occurrence probability of each local sea state, together with the corresponding significant wave height H_S, average peak period T_P and steepness S_P. According to the simplified methodology proposed by Nielsen and Pontes [103], the AEP can be predicted by:

$$\text{AEP} = 8760 \cdot \sum_{i=1}^{N} P_{mi} \cdot w_i \tag{5.27}$$

$$\sum_{i=1}^{N} w_i = 1 \tag{5.28}$$

where, P_{mi} – mean power in the ith sea state;
w_i – occurrence probability;
N – total number of sea states considered (assumed to be equal to 9).

Table 5.4: Sea states selected in the nearshore region of Rio de Janeiro

H_S	T_P [s]							Occurrence	T_P [s]	S_P	No.
[m]	4	6	8	10	12	14	16	[%]	Average		
0.25	0.0	0.5	1.7	0.6	0.1	0.1	0.0	3.0	8.40	0.002	SS1
0.75	0.2	3.7	17.3	8.5	3.5	1.1	0.1	34.4	8.88	0.006	SS2
1.25	0.0	1.6	9.5	11.3	5.6	1.6	0.2	29.8	9.78	0.007	SS3
1.75	0.0	0.5	3.1	7.1	4.8	1.5	0.1	17.1	10.47	0.010	SS4
2.25	0.0	0.0	1.4	3.4	3.3	0.7	0.2	9.0	10.87	0.012	SS5
2.75	0.0	0.0	0.3	1.2	1.9	0.8	0.1	4.3	11.63	0.013	SS6
3.25	0.0	0.0	0.0	0.3	0.7	0.6	0.1	1.7	12.59	0.013	SS7
3.75	0.0	0.0	0.0	0.1	0.2	0.1	0.0	0.4	12.00	0.017	SS8
4.25	0.0	0.0	0.0	0.0	0.1	0.0	0.0	0.1	12.00	0.019	SS9

Figure 5.17 presents results from the linear model (NSMc1). The sub-graphs (a), (b), (c) and (d) correspond to different configurations, all defined with the same $n = 6$ but different $L = 1.0$, 1.5, 2.0, 2.5 m respectively.

The bar lengths in each sub-graph depict the AEPs obtained with one global optimal B_{PTO} for all sea states in the given sea site. The region with lower values of α and γ (satisfying the condition C_γ close to 1.0) concentrates the configurations with better performance in all sub-graphs. In that region, larger L enhances the maximum AEP, as indicated by hollow inverted markers. As the values of α and γ increase, the AEP approaches a stable value, whatever L and n are. Actually, the reference value happens to be close to the value obtained from WEC without NSMc (LnMd1, 62.25 MWh).

The color scale diagram presents the AEPs for feasible configurations considering the constraints. The optimal performance is marked by red solid inverted triangles in each sub-graph. As L increases, the feasible region becomes smaller and the optimal value also approaches the above reference value accordingly.

Furthermore, Table 5.5 presents the optimal AEP and the relative increase with respect to the reference value (AEP_0) for a more comprehensive number of configurations.

$$\text{Percentage Increase} = \frac{\text{AEP} - \text{AEP}_0}{\text{AEP}_0} \times 100\% \tag{5.29}$$

For situations without constraints, the relative increase reaches values around at least 170%. Larger L leads to an even improved increase. However, if one considers the practical constraints, such improvements dramatically decrease to percentages

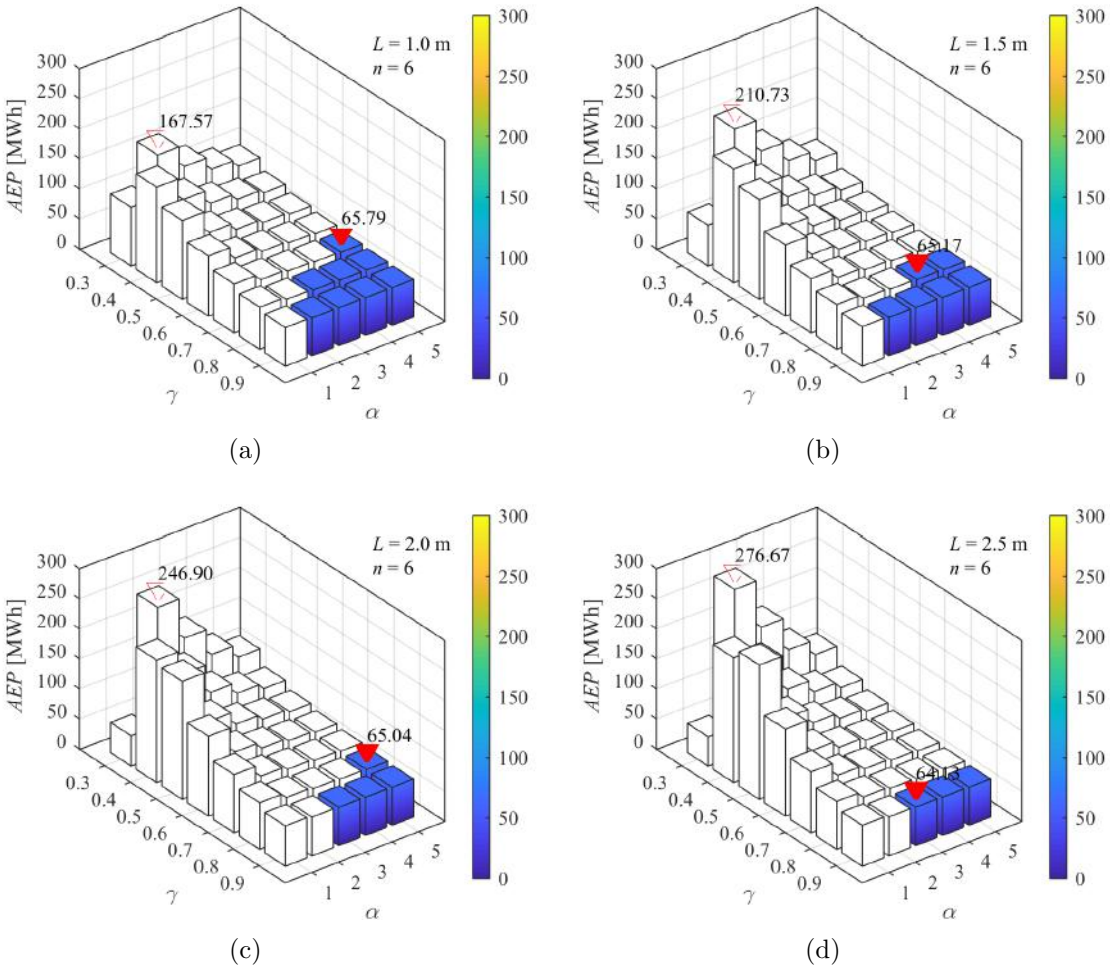

Figure 5.17: AEP: sphere buoy with NSMc1 ($n = 6$) in the nearshore region of Rio de Janeiro

as small as 10%. Observing the data in Table 5.5, one may draw the following conclusions:

- for the configurations in the same feasible region (in Figure 5.16, cells within the same background color areas), larger L induces higher improvement;
- for a given fixed L, the larger the number of springs n, the better the WEC performance.

Figure 5.18 shows that adopting more springs can increase the percentage increase. In general, for a fixed number of springs, the larger the length L is, the smaller the percentage increase. The exceptions would be the cases where fewer springs restrict the feasible regions.

By considering the more practical nonlinear model of the spherical WEC (NSMc3), the estimated AEP is a little smaller than that with NSMc1 as shown in Figure 5.19. The non-uniform waterplane area of the sphere makes the nonlinear

Table 5.5: AEP: sphere buoy with NSMc1 (LnMd1, $AEP_0 = 62.25$ MWh)

		n					No	
		3	4	6	9	12	constraints	
L [m]	1.0	63.84	64.24	65.79	66.69	68.78	167.57	AEP [MWh]
	1.5	63.14	63.44	65.17	66.96	68.23	210.73	
	2.0	63.20	63.44	65.04	65.75	67.66	246.90	
	2.5	–	63.37	64.13	66.11	67.48	276.67	
L [m]	1.0	2.55%	3.20%	5.69%	7.13%	10.49%	169.19%	Percentage Increase
	1.5	1.43%	1.91%	4.69%	7.57%	9.61%	238.52%	
	2.0	1.53%	1.91%	4.48%	5.62%	8.69%	296.63%	
	2.5	–	1.80%	3.02%	6.20%	8.40%	344.45%	

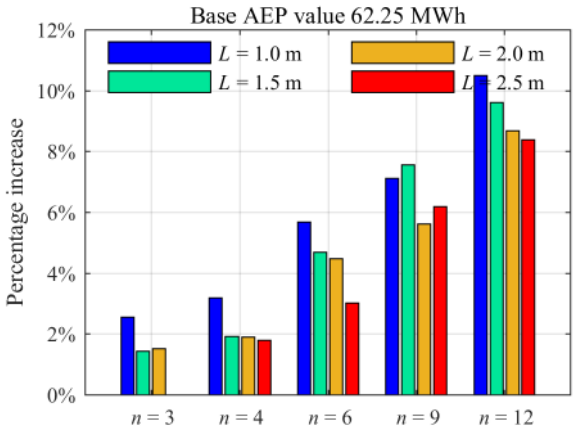

Figure 5.18: AEP percentage increase: sphere buoy with NSMc1

Froude-Krylov force acting on the buoy surface decreases if compared with the linear Froude-Krylov force.

Especially, the AEPs for bi-stable configurations decreases heavily compared with the QZS and mono-stable configurations (see Figure 5.17) with, $\alpha = 1.0$ and $\gamma = 0.3$). Further, it indicates that the bi-stable system with the nonlinear Froude-Krylov force model is not suitable for the applications in irregular wave conditions.

Other tendencies for NSMc3 (see Table 5.6 and Figure 5.20) are similar to that for NSMc1 analyzed previously. However, it is also evident that both NSMc1 and NSMc3 cannot improve the wave energy conversion significantly when considering the practical constraints imposed on the mechanical compression springs adopted in NSMc system, no matter if taking account of the nonlinear Froude-Krylov force model.

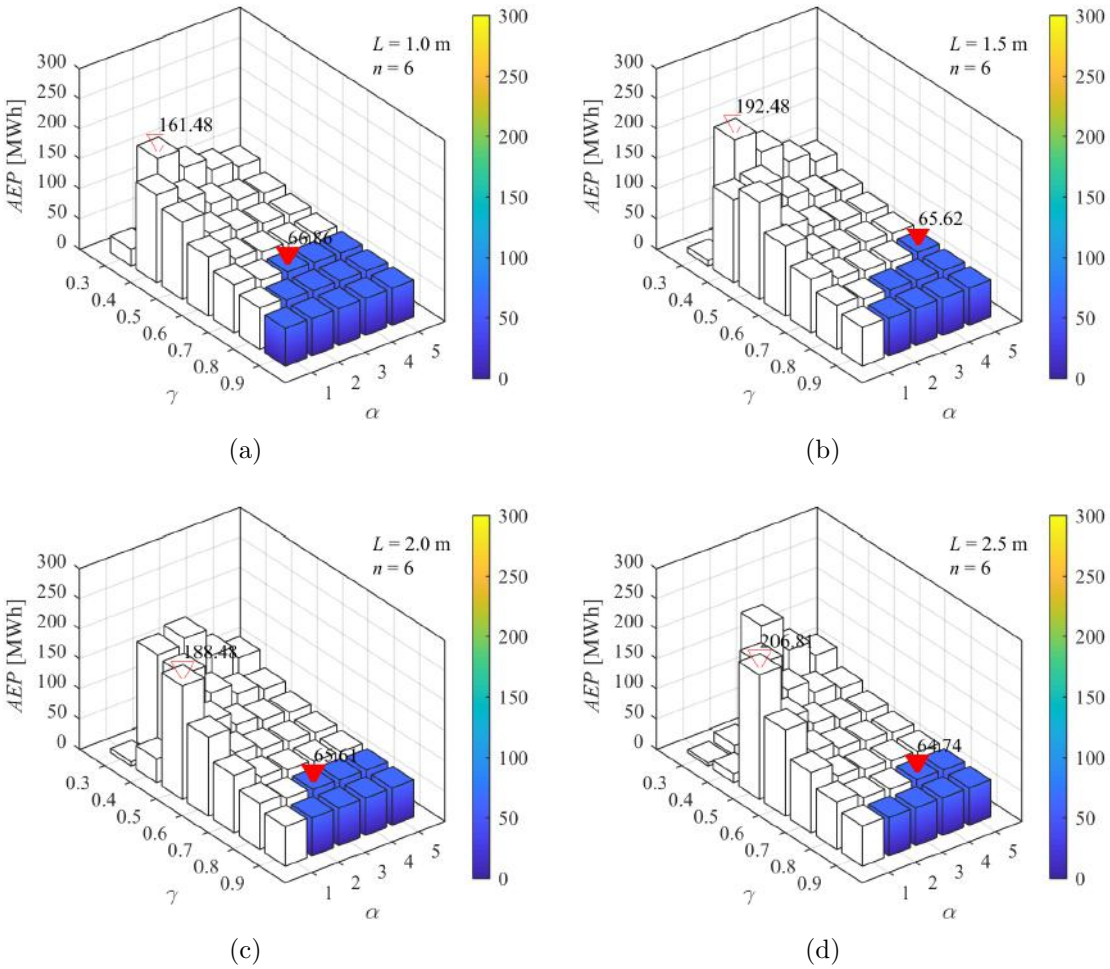

Figure 5.19: AEP: sphere buoy with NSMc3 ($n = 6$) in the nearshore region of Rio de Janeiro

Table 5.6: AEP: sphere buoy with NSMc3 (LnMd3, $\text{AEP}_0 = 60.82$ MWh)

		n					No constraints	
		3	4	6	9	12		
L [m]	1.0	62.38	62.79	64.39	65.32	67.43	161.48	AEP [MWh]
	1.5	61.70	61.99	63.76	65.62	66.88	192.48	
	2.0	61.75	61.98	63.64	64.37	66.29	188.48	
	2.5	–	61.91	62.69	64.74	66.12	206.81	
L [m]	1.0	2.56%	3.24%	5.87%	7.40%	10.87%	165.50%	Percentage Increase
	1.5	1.45%	1.92%	4.83%	7.89%	9.96%	216.47%	
	2.0	1.53%	1.91%	4.64%	5.84%	8.99%	209.90%	
	2.5	–	1.79%	3.07%	6.45%	8.71%	240.04%	

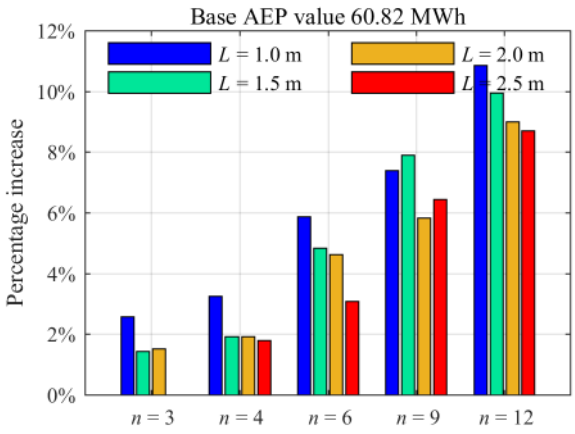

Figure 5.20: AEP percentage increase: sphere buoy with NSMc3

5.4 Summary

The present chapter started validating the analytical approach to calculate the non-linear Froude-Krylov force for both cases without and with the NSMc system. Then, the convergence analysis defined a reliable simulation time.

Simulations for the case with NSMc showed that the bi-stable NSMc cannot improve the WEC performance in a stable way if compared with the other two types of configurations: QZS and mono-stable.

The designing process of the mechanical compression springs imposed practical constraints on the NSMc. Further investigations of the wave energy conversion in the feasible region demonstrated that the NSMc was not suitable to enhance the WEC performance. In practice, it is the mechanical constraint that restricts dramatically its feasibility.

The above conclusions consequently inspired additional investigations to identify other feasible ways to apply the NSS concept, which will be the subject in the next chapter.

Chapter 6

Alternative NSS in WEC

The practical consideration in Chapter 5 imposed the limitation of the WEC performance with NSMc due to some realistic mechanical compression springs constraints. To overcome such NSMc practical restrictions, one possible approach substitutes the mechanical compression springs by equivalent pneumatic cylinders working like springs.

6.1 NSS with pneumatic cylinders (NSPn)

6.1.1 Description

As shown in Figure 6.1, pneumatic cylinders filled with pressurized gas (blue area) replace the conventional mechanical compression springs. The cylinder rods hinges from one of their ends to follow the buoy heave motion. An additional gas tank is necessary to feed all cylinders, composing the whole pneumatic system. The gas tank plays two primary functions: first, it equalizes the gas pressure in all cylinders to balance the force on the horizontal plane; second, the additional volume broadens the optional range of pressure and volume. Figure 4.1 (in Chapter 4) shows other schematic explanations valid for the pneumatic cylinders as well. The following sub-section describes further explanations of the relevant parameters.

6.1.2 Mathematical model

In the NSPn device, n cylinders (each piston area is A_0) are axisymmetrically connected. At the equilibrium position, each cylinder length is L, the total gas volume is V_0, and the pressure is P_0. A simple geometry derivation provides the gas volume V calculation for a given displacement of z,

$$V = V_0 + nA_0 \cdot (\sqrt{z^2 + L^2} - L) \tag{6.1}$$

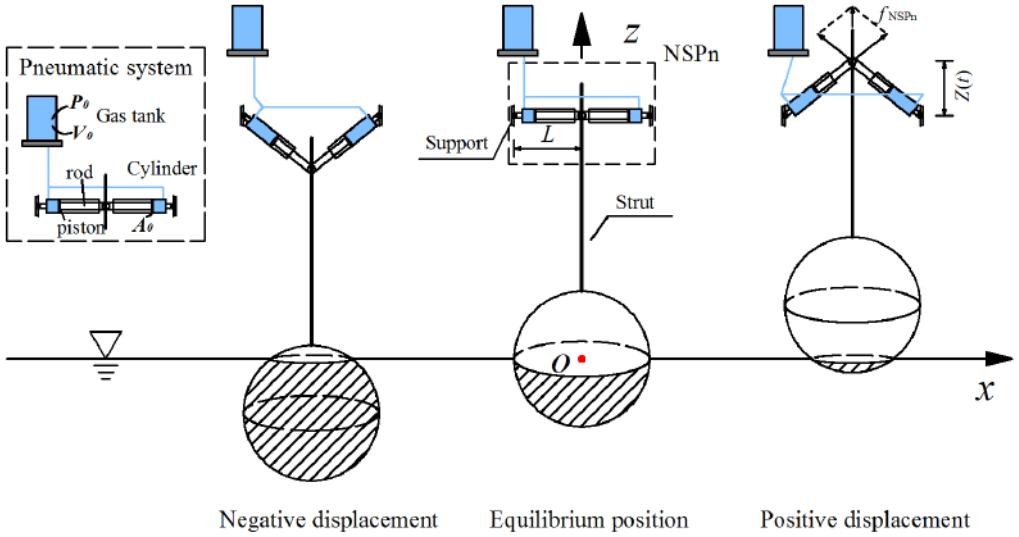

Figure 6.1: Schematic view of NSS with pneumatic cylinders (NSPn)

Assuming the adiabatic process, the corresponding pressure P satisfies the following relationship,

$$PV^{\mu} = P_0 V_0^{\mu} \tag{6.2}$$

where: μ is the specific heat ratio (1.4 in the case of nitrogen). Thus, the net vertical force supplied by the NSPn device acting on the buoy can be expressed as,

$$f_{\mathrm{NSPn}}(z) = nP_0A_0 \cdot \frac{z}{\sqrt{z^2 + L^2}} \cdot \left(\frac{V_0}{V}\right)^{\mu} \tag{6.3}$$

Many researchers have proposed different models to simulate the friction effect of the pneumatic cylinder. For instance, both Tustin [118] and Palomares et al. [119] involved Coulomb friction and additional velocity-dependent friction into the model; reference [120] provides some other simplified models. Nevertheless, in most cases, the friction forces are much smaller than the forces supplied by the cylinder. Some manufacturers even defined the cylinder efficiency η_P by:

$$\eta_P = \frac{f_{\mathrm{NSPn}}}{P \cdot A_0} \tag{6.4}$$

suggesting values between 0.85 and 0.90 for η_P which might be larger for a cylinder with larger piston area A_0 [120]. Therefore, ignoring friction force completely will not affect much the results.

Furthermore, for the sake of simplicity, two variables define the equivalent stiff-

ness nK_0 and the equivalent length L_0:

$$nK_0 = \frac{nP_0A_0}{L} \tag{6.5}$$

$$L_0 = \frac{V_0}{nA_0} \tag{6.6}$$

Substituting the above two equations into Eq. 6.3 reduces the expression of f_{NSPn} dimension from (n, L, P_0, A_0, V_0) to (n, L, L_0, K_0),

$$f_{\text{NSPn}}(z) = nK_0 \cdot \frac{z}{\sqrt{z^2 + L^2}} \cdot L \cdot \left(\frac{L_0}{L_0 + \sqrt{z^2 + L^2} - L} \right)^{\mu} \tag{6.7}$$

Consequently, defining two non-dimensional parameters (in a similar way as defined for the NSMc case),

$$\alpha = \frac{C_{WL}}{nK_0} = \frac{C_{WL}L}{nP_0A_0} \tag{6.8}$$

$$\gamma = \frac{nA_0L}{V_0} \tag{6.9}$$

For the NSPn, α is a ratio to describe the relative stiffness, and γ is an equivalent volume ratio.

Based on the Eqs. 6.1 and 6.2, the change of pressure P inside of the pneumatic system with the displacement of the buoy is expressed as,

$$\frac{P}{P_0} = \left(\frac{V_0}{V} \right)^{\mu} = \left(\frac{V_0}{V_0 + nA_0 \cdot (\sqrt{z^2 + L^2} - L)} \right)^{\mu} = \frac{1}{\left[1 + \gamma(\sqrt{(z/L)^2 + 1} - 1) \right]^{\mu}} \tag{6.10}$$

Figure 6.2 depicts P/P_0 patterns for different γ values with $L = 2.5$ m. At the equilibrium position ($z = 0$), $P = P_0$; as the buoy leaves out from the equilibrium position, the pressure decreases. The curves with different colors also show that the larger the γ value, the faster P changes.

Similar to z_{f0} mentioned earlier in the NSMc discussion, there is a limit (z_{lim}) for the NSPn excursion as well. Such a limit is actually related to the allowable piston stroke ($\triangle L$) from the equilibrium position.

$$z_{\text{lim}} = \pm\sqrt{(L + \triangle L)^2 - L^2} \tag{6.11}$$

$$\beta = \arctan\left(\frac{z_{\text{lim}}}{L} \right) \tag{6.12}$$

where, β is the maximum pneumatic cylinder rotational angle. The present work

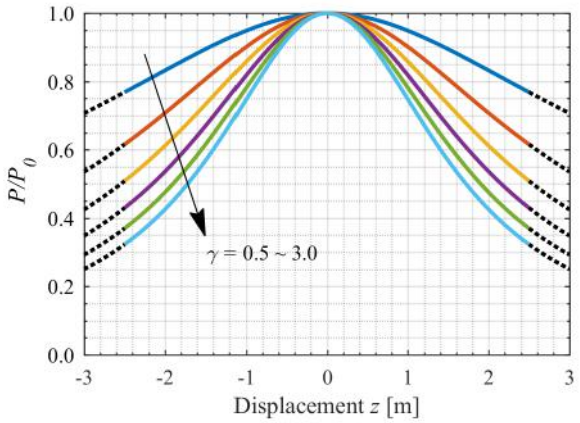

Figure 6.2: P/P_0 patterns for different γ values ($L = 2.5$ m)

selects $\beta = 45°$ referred to the application of "WaveSpring" technology in CorPower buoy [42]. Thus,

$$z_{\text{lim}} = \pm L \tag{6.13}$$

$$\triangle L = (\sqrt{2} - 1)L \approx 0.4L \tag{6.14}$$

After the piston reaches its limiting stroke, as well as the buoy's displacement is z_{lim}, if it has a further tendency to exceed the limit, the NSPn disconnects from the buoy, otherwise, the NSPn force acts on the buoy. Herein, the complete expression of $f_{\text{NSPn}}(z)$ is,

$$f_{\text{NSPn}}(z) = \begin{cases} nK_0 \cdot \dfrac{z}{\sqrt{z^2 + L^2}} \cdot L \cdot \left[\dfrac{L_0}{L_0 + \sqrt{z^2 + L^2} - L}\right]^{\mu} & |z| \leq L \\ 0 & |z| > L \end{cases} \tag{6.15}$$

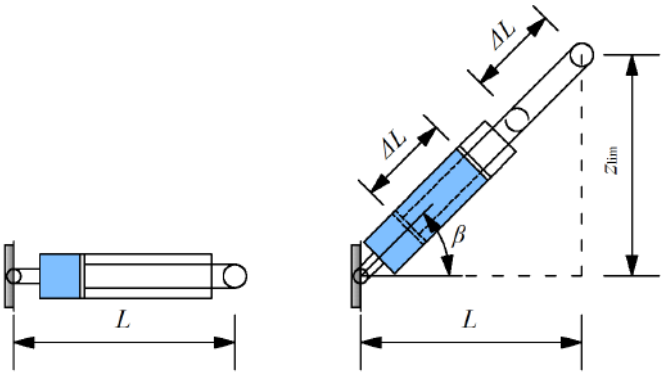

Figure 6.3: Pneumatic cylinder schematic view

However, differently from the NSMc, f_{NSPn} (z_{lim}) is not zero (as the red curve

shown in Figure 6.4) because of the remaining pressure inside of the pneumatic cylinder chambers.

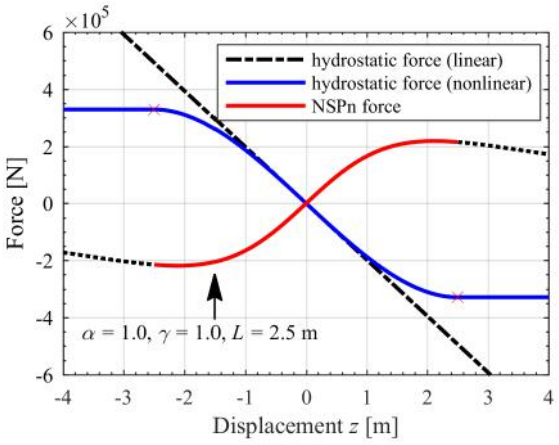

Figure 6.4: Hydrostatic force and NSPn force ($\alpha = 1.0$, $\gamma = 1.0$, $L = 2.5$ m)

The potential energy curve $e_{\mathrm{NSPn}}(z)$ is also described as,

$$\begin{aligned} e_{\mathrm{NSPn}}(z) &= -\int_0^z f_{\mathrm{NSPn}}(\zeta)d\zeta + e_{\mathrm{NSPn}}(0) \\ &= -\frac{nK_0LL_0}{\mu-1}\cdot\left[1-\left(\frac{L_0}{L_0+\sqrt{z^2+L^2}-L}\right)^{\mu-1}\right], \quad \text{when } |z| \le L \end{aligned} \tag{6.16}$$

where, potential energy $e_{\mathrm{NSPn}}(0) = 0$, not affecting the practical static analysis.

6.2 Static characteristic analysis

Furthermore, the analysis of the parameter effects on the NSPn characteristics adopts a similar approach as used for the NSMc case. It should be noticed that adjusting piston area A_0 and gas volume V_0 provides a corresponding suitable L_0. Thus, the γ value can be either larger or smaller than 1.0, which is another obvious difference compared with the NSMc system.

Figure 6.5 presents the patterns of the sphere restoring force in terms of displacement (z), with different NSPn configurations. Obviously, the system behavior definition is only related to α, and different values of α define three distinct behaviors:

- $\alpha < 1.0$, bi-stable behavior, leading to three zero points of restoring force;
- $\alpha = 1.0$, QZS behavior, leading to only one zero point of restoring force and zero stiffness at the equilibrium position;

- $\alpha > 1.0$, mono-stable behavior,leading to only one zero point of restoring force but non-zero stiffness at equilibrium position.

The above features also indicate that α plays a more important role than γ in determining the NSPn characteristics.

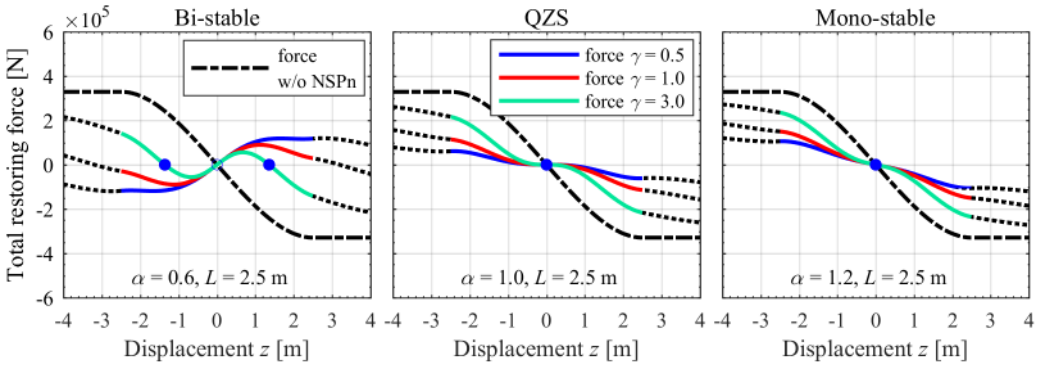

Figure 6.5: Sphere static restoring force with NSPn ($L = 2.5$ m)

In Figure 6.6, the bi-stable configuration still features two stable equilibrium points. For the cases, $\gamma = 0.5$ and 1.0, the corresponding stable equilibrium positions with respect to the bi-stable configurations exceed the displacement limit z_{lim}, thus they are not presented on the corresponding curves (blue and red curves).

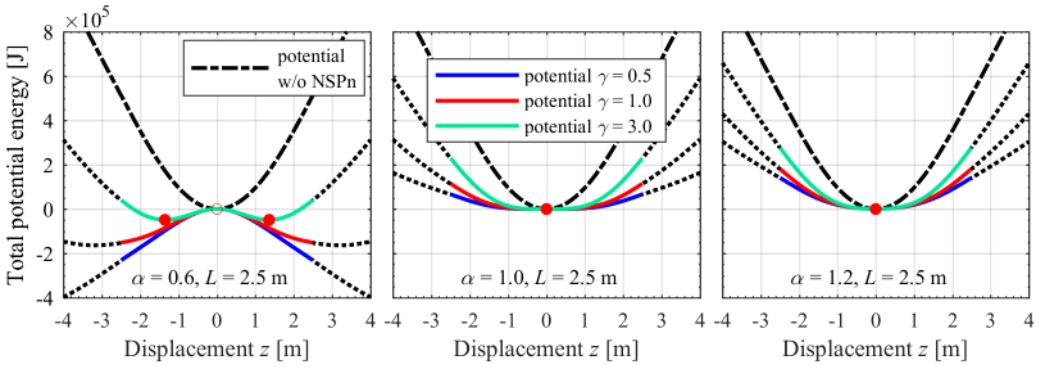

Figure 6.6: Sphere potential energy with NSPn ($L = 2.5$ m)

Figures 6.5 and 6.6 also show that, if either α or γ increases, both the restoring force and potential energy curves further approach the corresponding original nonlinear hydrostatic restoring force and potential energy. The direct conclusion would be that the NSPn system with too large α and γ values cannot significantly change the characteristics of the sphere buoy dynamics. Thus, no significant improvements would be obtained.

6.3 Validation and convergence analysis

6.3.1 Response for regular wave conditions

Figure 6.7 presents the CWR contours for the NSPn with QZS ($\alpha = 1.0$, $\gamma = 1.0$) and mono-stable ($\alpha = 1.2$, $\gamma = 1.0$) configurations using linear (NSPn1) and nonlinear models (meshing – NSPn2 and analytical – NSPn3) acted by different wave heights. In each contour, the dark red color area depicts higher CWR values, while the dark blue color area depicts lower CWR values. The white dot indicates the maximum CWR value for each contour. The contour line for the level of CWR = 0.45, that is equal to the CWR peak value of the model without NSPn, is defined by the black dashed curve. Thus within the region under the curve, it determines the wave period and PTO damping values which extract more wave energy than that in the resonant state of LnMd can be extracted. Note that all the simulations in regular wave conditions are conducted considering the drag correction with a drag coefficient $C_d = 0.6$ (as recommended by Giorgi and Ringwood [98] for the same sphere buoy). The following section continues to analyze the C_d influence.

Figure 6.7 compares four groups of contours for meshing and analytical nonlinear models and they present very good consistencies. Thus, the analytical nonlinear model confirms further validation for applications in NSPn analysis.

Moreover, the mono-table configuration produces broader (T, B_{PTO}) region featuring higher CWR than for the QZS configuration. The wave period with respect to the maximum CWR decreases period around 1.0 s from the QZS to the mono-stable configuration. However, the CWR peak presents an increase for the nonlinear model which is the opposite in the NSMc case analyzed in Chapter 4. Such a characteristic is also different from the linear model in Figure 6.7, though the linear model induces broader and higher CWR response. In another aspect, applying the NSPn system, the nonlinear model requires to handle the nonlinear Froude-Krylov force due to the sphere waterplane area variation.

In addition, considering the multiple solutions characteristic of the NSPn with bi-stable configuration, the CWR responses are described by the scatters corresponding to different B_{PTO} values instead of the contour, as shown from Figure 6.8 to Figure 6.9. The bi-stable configuration features $\alpha = 0.8$, $\gamma = 1.0$, $L = 2.5$ m, and three different B_{PTO} values ($B_{PTO} = 20,\ 70,\ 120$ kNs/m). In each figure, the blue dots depict the solutions featuring the intra-well motion (as defined in Chapter 4), while the red dots represent the inter-well and chaotic solutions (actually only in the low damping conditions the chaotic behavior appears).

When using the linear model (see Figure 6.8, multiple solutions only appear under high wave and large damping conditions besides the chaos. However, with the analytical nonlinear model (in Figure 6.9), the multiple solutions ranges become

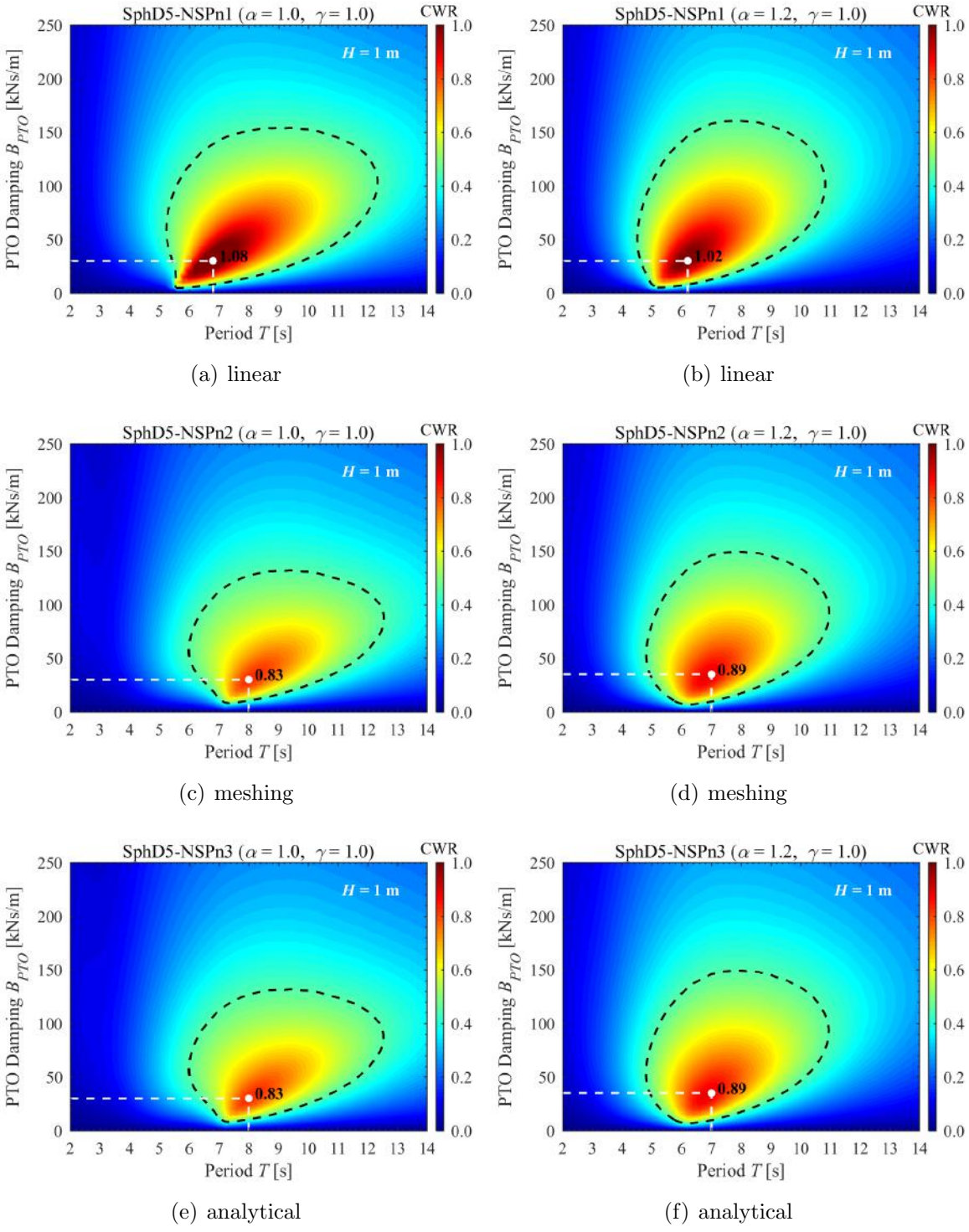

(a) linear (b) linear

(c) meshing (d) meshing

(e) analytical (f) analytical

Figure 6.7: CWR comparisons between linear and nonlinear models ($H = 1.0$ m)

much larger, increasing with the damping. Almost all the multiple solutions feature intra-well motion. The reason is the contribution from the nonlinear Froude-Krylov force model strengthening the nonlinear effects of the system with NSPn and the potential energy obstacle. In addition, due to the large damping, the buoy experiences more difficulties to escape from the local "potential well" around either of the

stable equilibrium positions. Not only the multiple solutions increase the system instability, but also the responses are weakened.

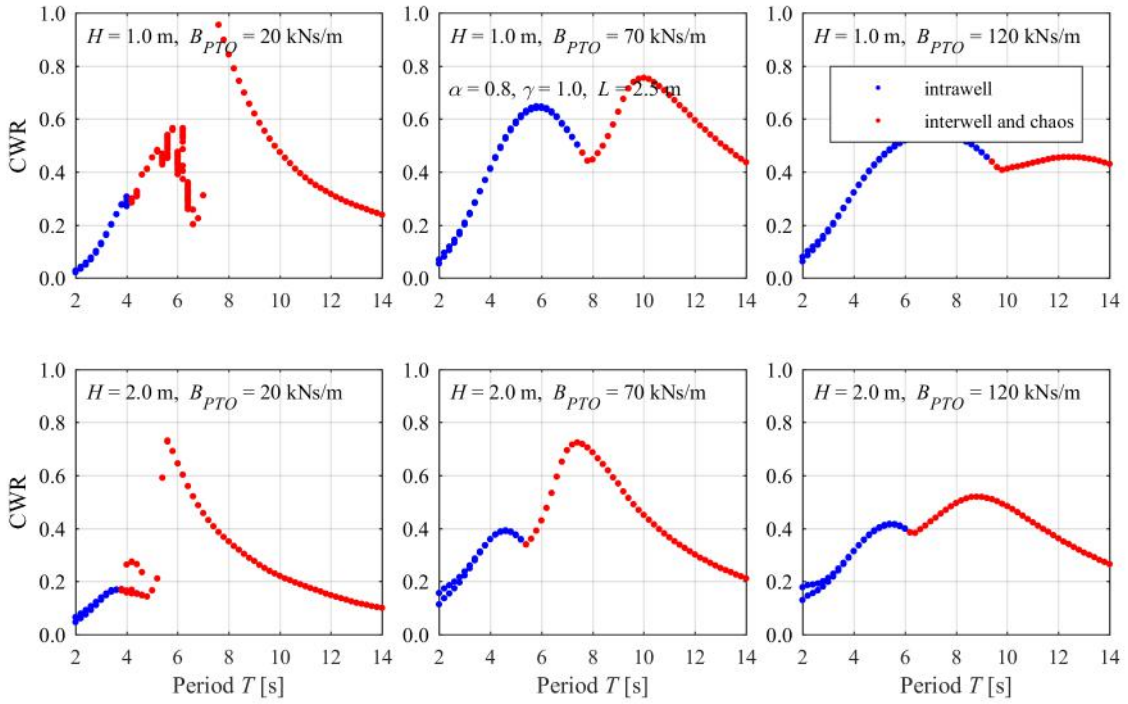

Figure 6.8: CWR with bi-stable configuration ($\alpha = 0.8, \gamma = 1.0, L = 2.5$ m) using linear approach

Though increasing γ can reduce the appearance of multiple solutions under the long wave conditions with bi-stable configuration, the optimal CWR is not an attractive solution as that associated with both QZS and mono-stable configurations. Thus only the latter two configurations are investigated more emphatically in the following analysis.

6.3.2 Convergence analysis for irregular wave conditions

Based on the previous analysis, the convergence analysis for the QZS and mono-stable systems is conducted following the same simulation parameters as those used in the NSMc case. Figures 6.10 and 6.11 validate the effective simulation period $t_S = 2000$ s and sampling frequency $f_S = 100$ Hz used for the NSPn case in irregular wave analysis.

6.4 NSPn Feasibility

Following the preliminary investigations, this section analyzes the NSPn feasibility. First, Table 6.1 presents the main parameters of the NSPn. Here, D_0 is the piston

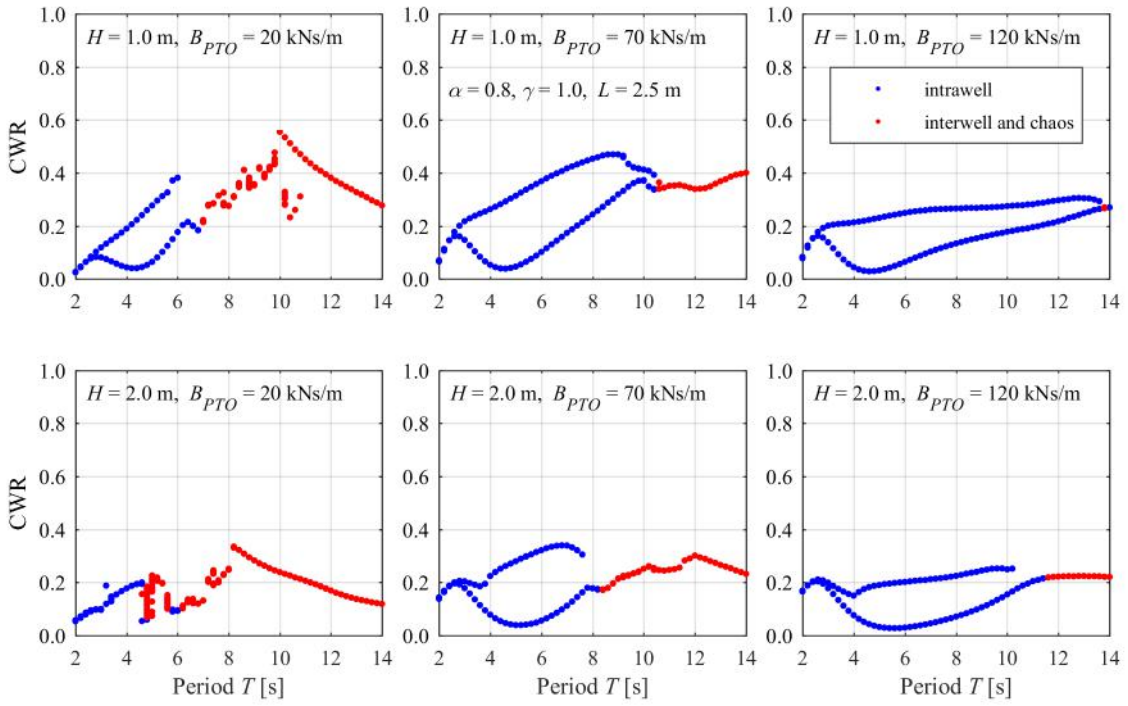

Figure 6.9: CWR with bi-stable configuration ($\alpha = 0.8, \gamma = 1.0, L = 2.5$ m) using analytical nonlinear approach

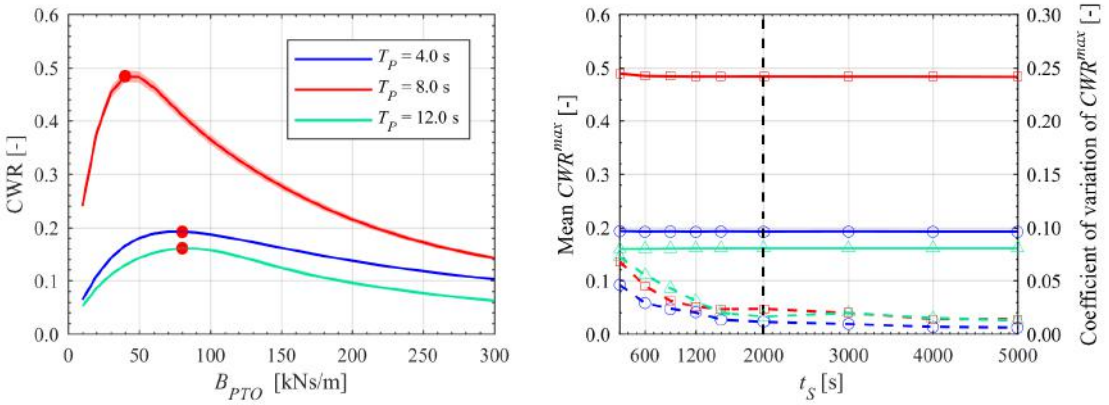

(a) (b)

Figure 6.10: Convergence analysis of the simulation length (t_S) with QZS configuration ($\alpha = 1.0$, $\gamma = 1.0$, $L = 2.5$ m) for sea states: $S_P = 0.025$, $T_P = 4.0$, 8.0, 12.0 s

diameter (piston area $A_0 = \pi D_0^2/4$). The geometric parameters are not strongly restricted. However, the pressure cannot be too high in the industrial applications [33]. At present, the only prototype application known is the 1/2 model scale CorPower buoy. It works with pressure around 21.5 bar according to the parameter published by Todalshaug et al. [42].

For a pneumatic cylinder, the buckling of the rod is an important effect that has to be avoided during the operation. To prevent buckling, the maximum permissible

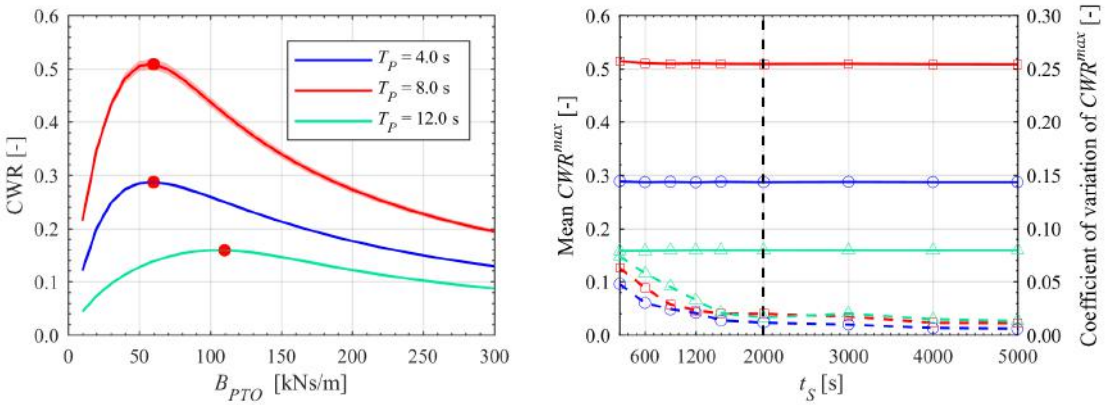

(a) (b)

Figure 6.11: Convergence analysis on the simulation length (t_S) with mono-stable configuration ($\alpha = 1.2$, $\gamma = 1.0$, $L = 2.5$ m) for sea states: $S_P = 0.025$, $T_P = 4.0,\ 8.0,\ 12.0$ s

Table 6.1: NSPn main parameters

Parameters	Units	Min	Max
D_0	[cm]	2	30
P_0	[bar] (1 bar = 10^5 Pa)	1	20
V_0	[m^3]	0.001	1

compressive axial load on a piston rod is [120],

$$F_k = \frac{\pi^3 \cdot E \cdot D_{\text{rod}}^4}{64 l_k^2 S} \tag{6.17}$$

where, F_k – permissible buckling force in N;

E – modulus of elasticity of rod material (e.g., $210,000\text{N/mm}^2$ for steel);

D_{rod} – rod diameter in mm;

l_k – effective length in mm;

S – safety factor, often used value is 5.

Here, the effective length l_k is the distance between the free-end and support. Actually, its maximum value equals the length of cylinder when it reaches the stroke limit $\sqrt{2}L \cdot 10^3$.

This permissible value should be higher than the value suggested by the maximum working pressure P_0 and the piston area A_0, which is related with α.

$$F_k > F_{k0} = P_0 A_0 = \frac{C_{WL} L}{n\alpha} \tag{6.18}$$

The corresponding permissible rod diameter should satisfy,

$$D_{\text{rod}} > \left(\frac{64 l_k^2 S F_{k0}}{\pi^3 E}\right)^{0.25} \tag{6.19}$$

Certainly, D_{rod} is not larger than D_0 at most. The condition below supplies more redundancy for the design,

$$D_{\text{rod}} \leq 0.5 D_0 \cdot 10 \tag{6.20}$$

Combining Eqs. 6.19 and 6.20, the condition related with D_0 is defined,

$$\left(\frac{64 l_k^2 S F_{k0}}{\pi^3 E}\right)^{0.25} < 0.5 D_0 \cdot 10 \tag{6.21}$$

Finally, the parameters in the space of (D_0, P_0, V_0) as shown in Table 6.1 should satisfy the Eq. 6.21 to define one feasible set of (α, γ). Thence, Figure 6.12 presents the NSPn feasible regions (α, γ) under different combinations of (L, n).

One of the most evident features resulting from the present analysis indicates that the feasible region occupies a broader area, meaning that the constraints' influences are quite limited. Similar to the NSMc feasible region as shown in Figure 5.16, decreasing L or increasing n induces the feasible region covering (α, γ) with smaller values where the better performance is expected to appear. However, when the L/n values are the same, the feasible regions are no longer the same as can be observed in the NSMc feasible analysis.

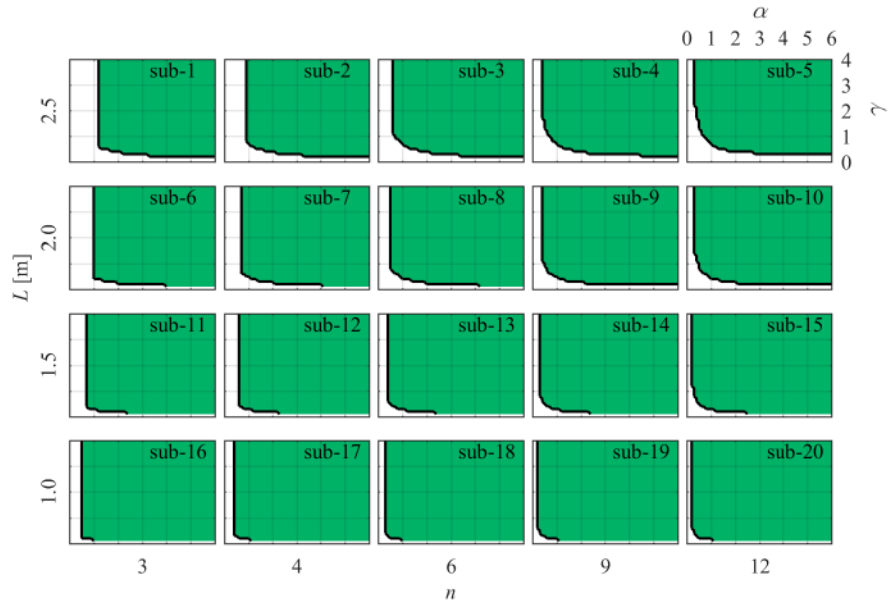

Figure 6.12: NSPn feasible regions

Continually, Figure 6.13 presents the NSPn1 AEP in the nearshore region of Rio de Janeiro, where the range of (α, γ) can cover bi-stable, QZS and mono-stable

configurations.

Not considering the (α, γ) constraints, the maximum AEP appears at the smallest α and γ for each L configuration as the bars shown in Figure 6.13. Simultaneously, it increases as L also increases. Compared with the previous NSMc1, the present AEP features a decline, but not more than 10%. However, considering the performance under the feasible (α, γ) parameters as shown in Figure 6.12, the corresponding maximum AEP does not decrease dramatically as it happens for NSMc1 basically because of its broader feasible region. Furthermore, the number of pneumatic cylinders adopted is less than the necessary springs in the NSMc case.

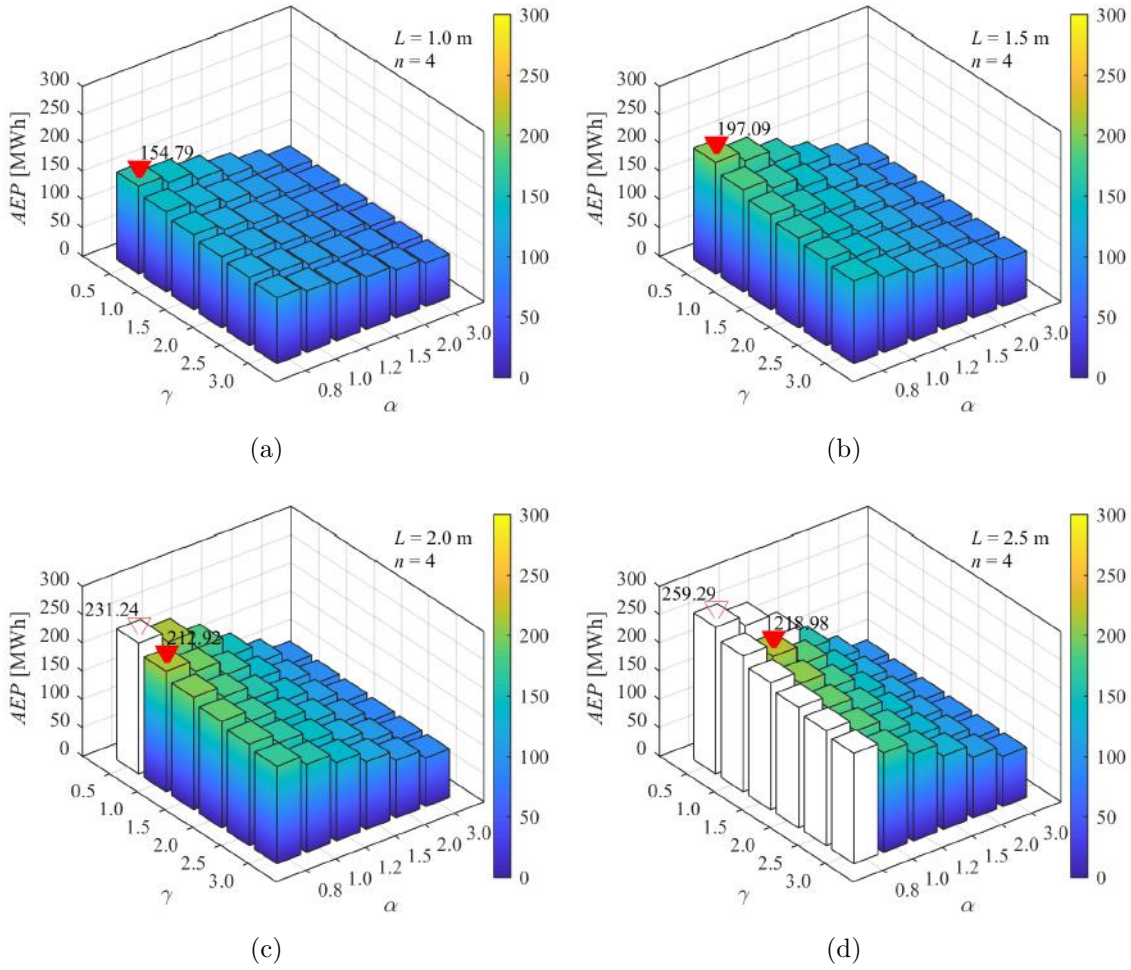

Figure 6.13: AEP: sphere buoy with NSPn1 ($n = 4$) in the nearshore region of Rio de Janeiro

The Table 6.2 and Figure 6.14 present a far more comprehensive comparison considering different number of pneumatic cylinders. For all groups of pneumatic cylinders, the longer L, the larger the percentage of increasing, except that if $n = 3$, the feasible (α, γ) with $L = 2.5$ m is more heavily restricted than any other cases. The least increase is greater than 150%, even considering the feasible configuration. It indicates the great advantage of NSPn1 if compared with NSMc1.

Table 6.2: AEP: sphere buoy with NSPn1 (LnMd1, $AEP_0 = 62.25$ MWh)

		n						
		3	4	6	9	12	No constraints	
L [m]	1.0	154.79	154.79	154.79	154.79	154.79	154.79	AEP [MWh]
	1.5	197.09	197.09	197.09	197.09	197.09	197.09	
	2.0	212.88	212.92	212.92	212.92	212.92	231.24	
	2.5	186.83	218.98	240.01	240.01	240.01	259.29	
L [m]	1.0	148.67%	148.67%	148.67%	148.67%	148.67%	148.67%	Percentage Increase
	1.5	216.62%	216.62%	216.62%	216.62%	216.62%	216.62%	
	2.0	241.97%	242.05%	242.05%	242.05%	242.05%	271.47%	
	2.5	200.13%	251.77%	285.56%	285.56%	285.56%	316.53%	

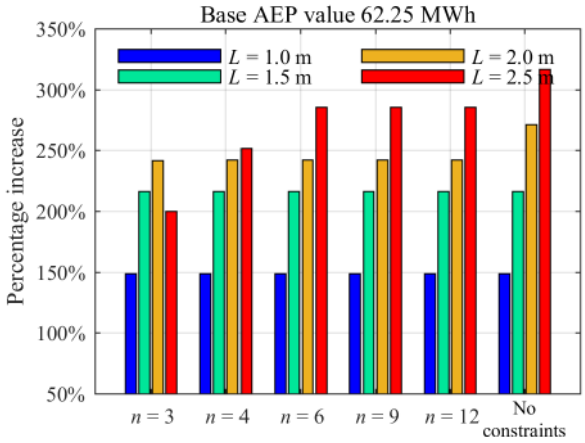

Figure 6.14: AEP percentage increase: sphere buoy with NSPn1

Consequently, Figure 6.15 presents the results for the NSPn3 model analysis. One obvious difference from the NSPn1 results is the maximum AEP without considering the practical constraints not appearing at the smallest α and γ for the cases $L = 2.0,\ 2.5$ m. The instability of bi-stable NSPn as explained in Section 6.3 would be the reason for such a difference. An even smaller γ value can further weaken the output (see Figure 6.15 (c) and (d)). Thus, it confirms that the configurations for $\alpha \geq 1$ with more reliable outputs are better options for practical applications.

Besides, if compared with the NSMc, considering the feasible (α, γ) configurations, the NSPn3 presents more AEP decreasing with respect to the NSPn1. It is because the role of the NSMc is dramatically weakened by imposing practical constraints. The system behaves more like a linear model with a small amplitude motion. Thus, the influence of nonlinear Froude-Krylov force is not too significant, while the feasibility restriction on the NSPn will be so limited that the nonlinear Froude-Krylov force still plays a non-negligible role.

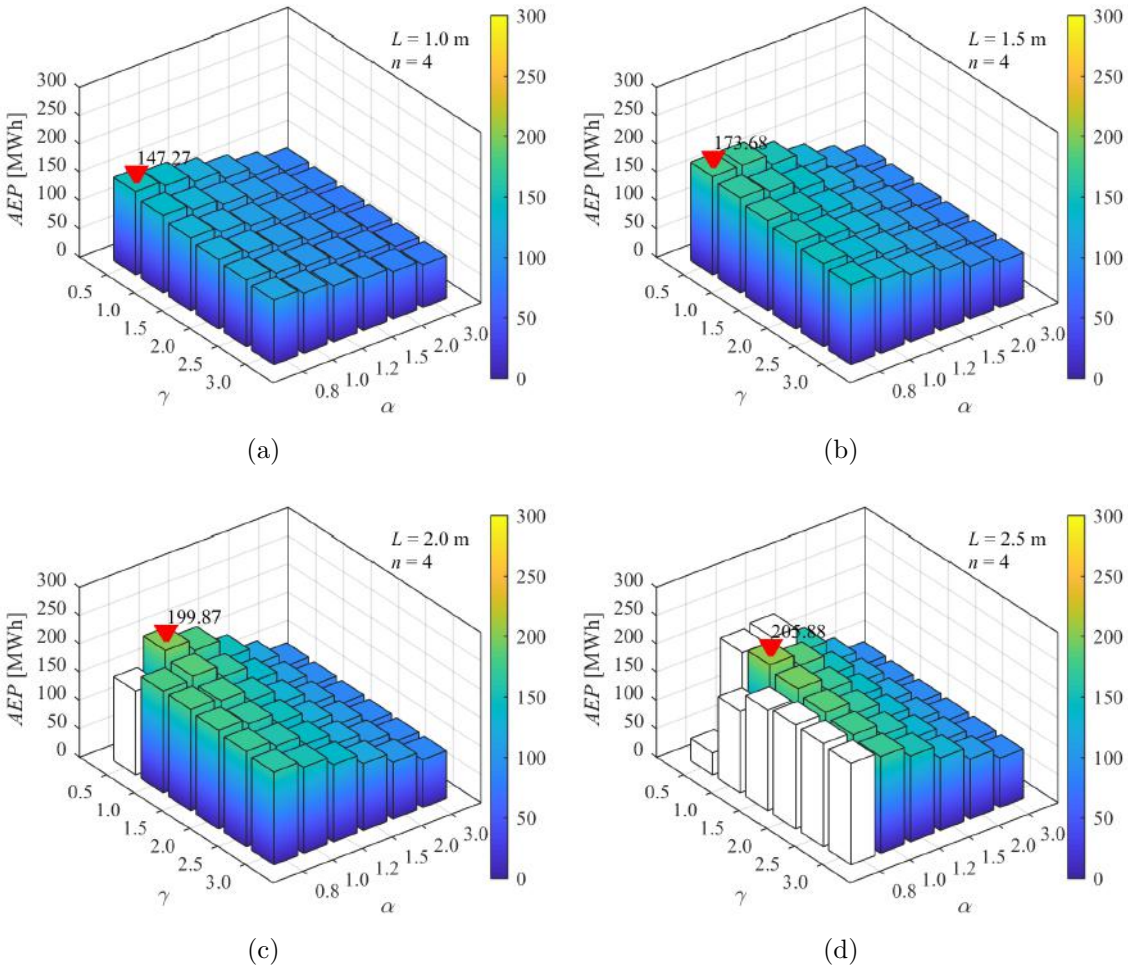

Figure 6.15: AEP: sphere buoy with NSPn3 ($n = 4$) in the nearshore region of Rio de Janeiro

Table 6.3: AEP: sphere buoy with NSPn3 (LnMd3, $\text{AEP}_0 = 60.82$ MWh)

		n					No	
		3	4	6	9	12	constraints	
L [m]	1.0	147.27	147.27	147.27	147.27	147.27	147.27	AEP [MWh]
	1.5	173.68	173.68	173.68	173.68	173.68	173.68	
	2.0	199.87	199.87	199.87	199.87	199.87	199.87	
	2.5	185.05	205.88	205.88	205.88	205.88	205.88	
L [m]	1.0	142.14%	142.14%	142.14%	142.14%	142.14%	142.14%	Percentage Increase
	1.5	185.56%	185.56%	185.56%	185.56%	185.56%	185.56%	
	2.0	228.63%	228.63%	228.63%	228.63%	228.63%	228.63%	
	2.5	204.26%	238.51%	238.51%	238.51%	238.51%	238.51%	

Figure 6.16 depicts the limited influence of the feasible consideration in a more obvious way. Almost all the cases with different amounts of pneumatic cylinders

behave in a similar manner as they were not considering the feasibility restriction.

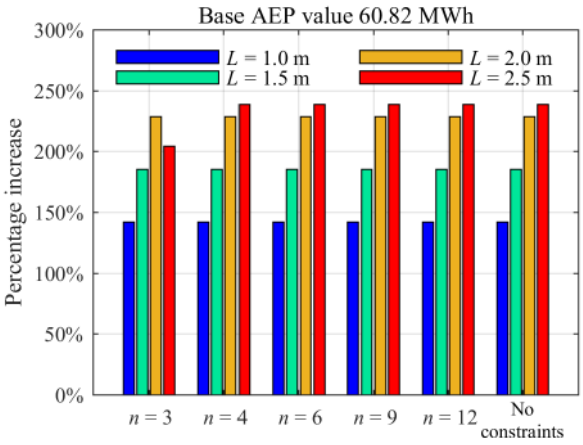

Figure 6.16: AEP percentage increase: sphere buoy with NSPn3

6.5 Performance analysis

Based on the previous feasibility analysis, the constraints on the NSPn performance is not as significant as for the NSMc case. The effects of the relevant parameters – α and γ on the performance can be explored in a broad feasible region inherently. Besides, the drag correction effect makes the analysis more comprehensive and qualified. As the effect of L and n discussed in the previous section, the present investigation takes one example with $L = 2.5\,\mathrm{m}$, $n = 4$ into consideration to focus more on the influences of other factors.

6.5.1 The α effect

With $L = 2.5\,\mathrm{m}$, $n = 4$, the feasible α range is defined by $\alpha \geq 1.0$ as shown in Figure 6.15 (d). Figure 6.17 describes the influence of α on the CWR for nine different sea states in the nearshore region of Rio de Janeiro (see Table. 5.4). The investigation also includes the CWR changes as a function of B_{PTO}. The colorful solid curves represent the average results with respect to 50 different irregular waves defined by the same statistic properties but distinct random phase angles. The black dashed curves depict the reference results of LnMd3. The shaded bars correspond to the occurrence probability of the nine sea states.

For the sea state SS1 ($H = 0.25\,\mathrm{m}$), the configurations with $\alpha = 1.2$ and 1.5 perform better than that with $\alpha = 1.0$. In other words, some of the mono-stable configurations can achieve better performance than the QZS configuration. Such a phenomenon occurs because sea state SS1 is not energetic enough to force the QZS system to "jump" from the low-energy branch to the high-energy branch. However,

considering the smaller occurrence probability and lower energy density of SS1, it will not affect the global AEP significantly.

For the other sea states investigated, the optimal CWR in terms of B_{PTO} with the QZS configuration is always larger than that with the mono-stable configuration. It decreases with increasing α, while the corresponding optimal B_{PTO} increases. It features one approaching tendency to the LnMd3 if α increases continually. It further indicates that the NSPn configuration with α equal to or close to 1.0 is more preferable even in random sea states.

Note that the red dots depict the cases featuring the average maximum excursion exceeding the z_{lim} with respect to the 50 different irregular waves defined by the same statistic properties but distinct random phase angles. For the sea states with medium energy level, such as from SS2 to SS5, the suitable B_{PTO} around the optimal value can force the motion not to exceed the excursion limit. Moreover, for the other more energetic sea states, even larger B_{PTO} are required to restrict the buoy motion.

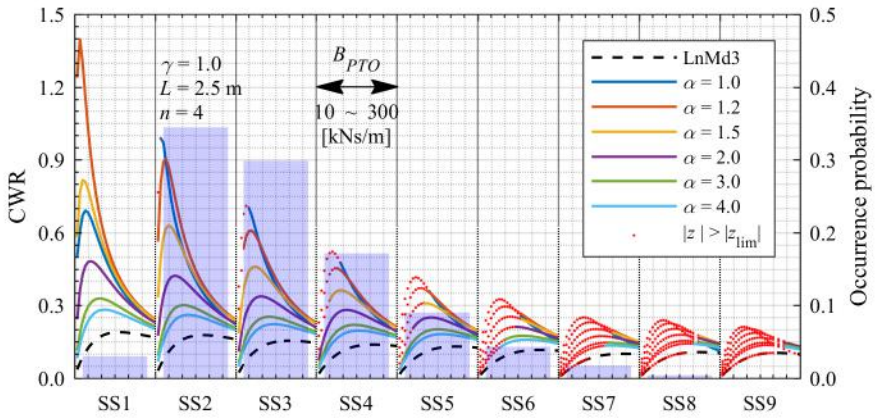

Figure 6.17: CWR: sphere buoy with NSPn ($\gamma = 1.0$, $L = 2.5$ m and $n = 4$) for different sea states

6.5.2 The γ effect

Similarly, with smaller α, such as in the QZS configuration shown in Figure 6.18, increasing γ slightly reduces the optimal CWR. For larger α (as shown in Figure 6.19), the curves for distinct γ are almost overlapped with each other, meaning that the influence of γ on the CWR becomes weaker as α increases.

Compared with the significant changes observed when α was varied in the previous analysis, γ has only a minor effect on selecting the NSPn configuration. Herein, the NSPn parameter related with α, such as P_0, requires more careful considerations in the design process.

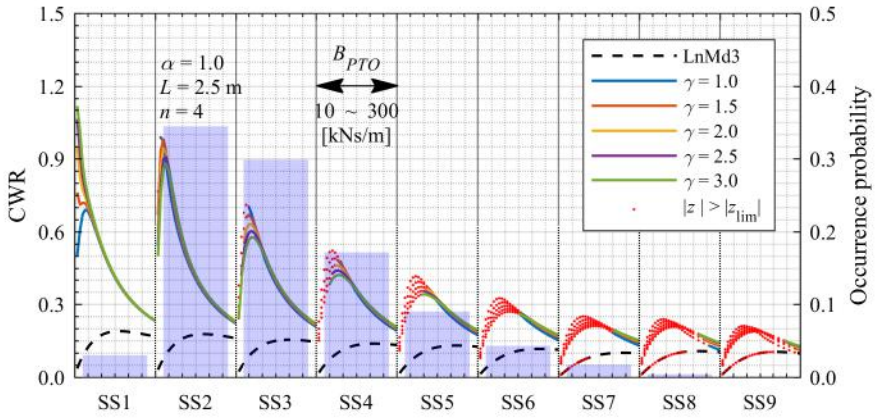

Figure 6.18: CWR: sphere buoy with NSPn ($\alpha = 1.0$, $L = 2.5$ m and $n = 4$) for different sea states

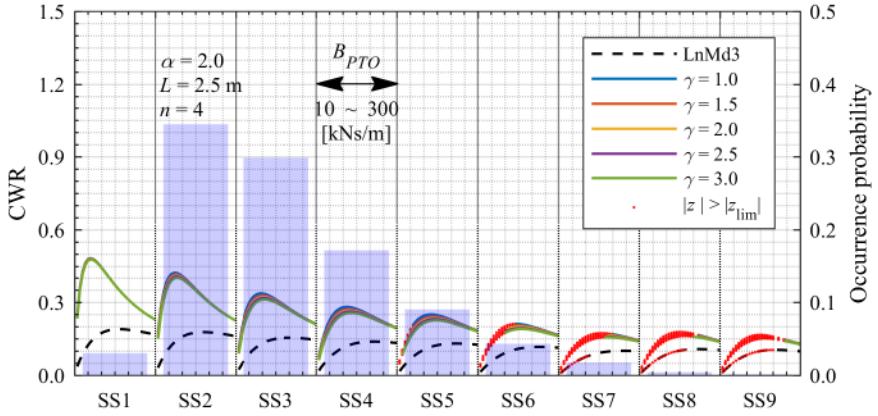

Figure 6.19: CWR: sphere buoy with NSPn ($\alpha = 2.0$, $L = 2.5$ m and $n = 4$) for different sea states

6.5.3 The C_d effect

To evaluate the C_d effect on AEP, a series of values are adopted with the reference value $C_d = 0.6$ recommended in [98]. In Figure 6.20, blue bars corresponding to the left axis depict the percentage difference between the reference C_d and other values, while the red curve describes the corresponding AEP pattern. Relative to the case without C_d, only 11% decrease is induced with $C_d = 0.6$. As the C_d increases, the descending becomes more moderate. Similar phenomenon appears in [98] as well.

Here, the AEP computation does not consider the excursion limit mentioned in the previous two sections. The large motion occurrence amplifies the drag effect. More robust analysis conducted in the comparisons among LnMd, LtCt, and NSPn will consider such a factor further.

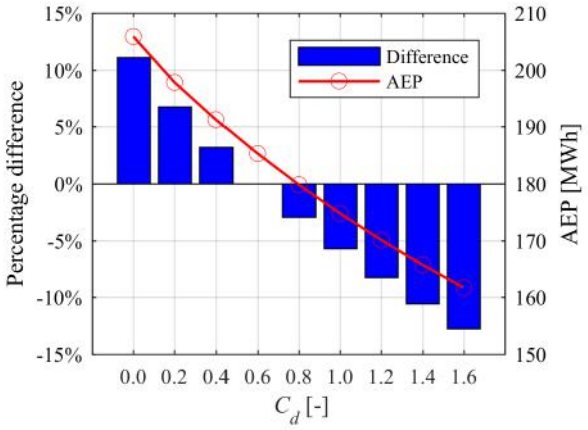

Figure 6.20: C_d influence on AEP ($L = 2.5$ m, $n = 4$)

6.6 Comparisons

Based on the understanding of the NSPn characteristics and from the analysis of the influence factors, it would be reasonable to select several typical configurations featuring better performance in wave energy conversion, such as the QZS and monostable configurations with α around 1.0. Four configurations are listed in Table 6.4.

Table 6.4: NSPn configurations

NSPn	α	γ	L [m]	n
I	1.0	1.0	2.5	4
II	1.0	3.0	2.5	4
III	1.2	1.0	2.5	4
IV	1.2	3.0	2.5	4

6.6.1 Frequency response contour

In addition, the present section adopts latching control (LtCt) with constant latching duration [15, 121] to conduct the comparison as it is easy to be implemented practically and no reactive power flow increases the cost of the PTO system. Figures 6.21 and 6.22 present the CWR responses in regular wave conditions for both LnMd and LtCt using linear (LnMd1, LtCt1) and analytical nonlinear (LnMd3, LtCt3) models respectively. Drag coefficient $C_d = 0.6$ is still taken as the reference value.

As LnMd cannot generate large amplitude motion, the effect of nonlinear model is not significant. Herein, for LnMd1 and LnMd3, the CWR contours do not change too much, even increasing wave height H from 1.0 m to 2.0 m (see Figure 6.21). The optimal CWR appears around the natural period $T_0 = 3.2$ s.

Moreover, the peak value CWR = 0.45 works as a reference value featuring the range of contour in which better wave energy conversion can be achieved for both NSPn and LtCt.

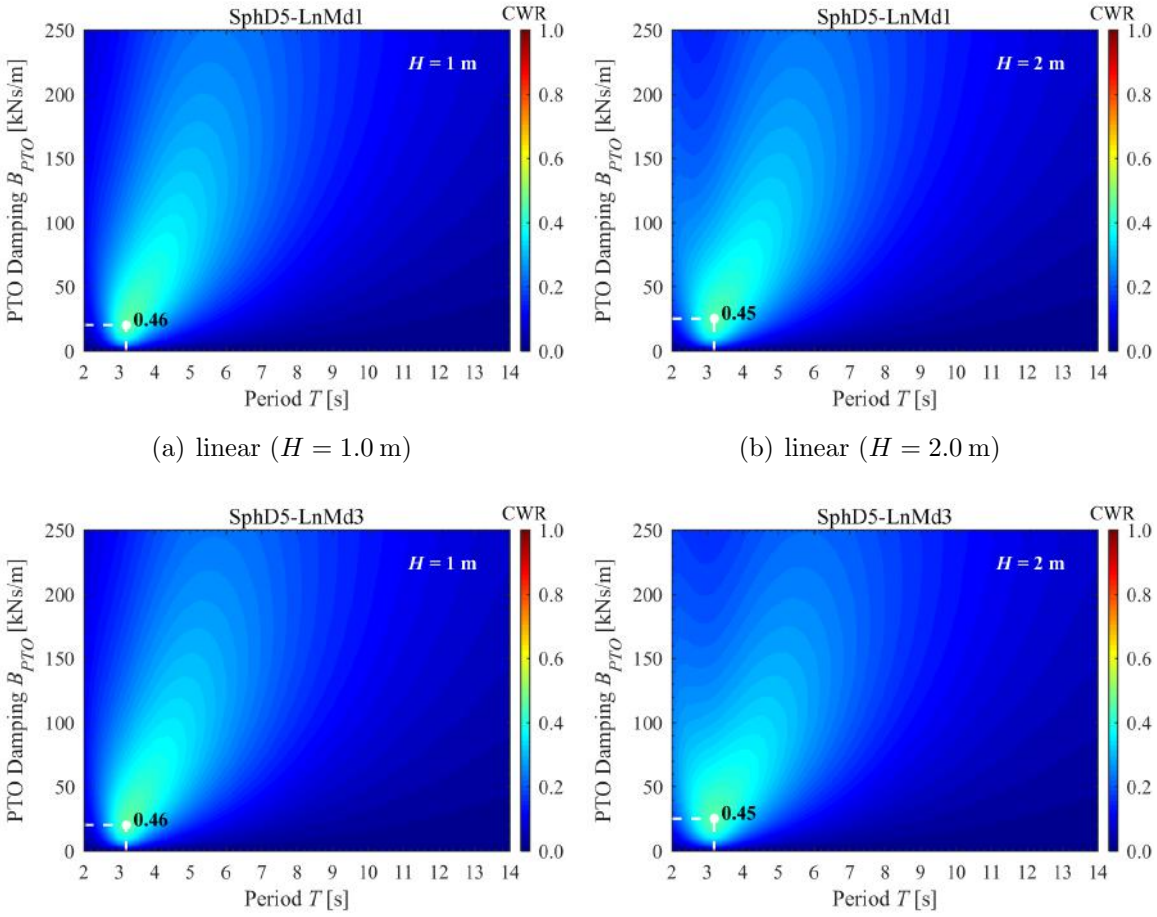

(a) linear ($H = 1.0$ m)

(b) linear ($H = 2.0$ m)

(c) nonlinear ($H = 1.0$ m)

(d) nonlinear ($H = 2.0$ m)

Figure 6.21: LnMd CWR using linear and nonlinear models ($H = 1.0,\ 2.0$ m)

In the LtCt cases, together with B_{PTO}, latching duration also affects the CWR. The conventional analytical formula of constant latching duration is based on the undamped natural period. Therefore it does not work correctly if PTO damping is included, not to mention the nonlinear Froude-Krylov force effect. Thus, the optimal latching duration is evaluated for each B_{PTO} from a series of latching durations smaller than the values provided by the analytical formula. The corresponding CWR is defined as the tuned CWR.

Similar to the NSPn case investigated in the previous section, the response contours of LtCt also capture a large area featuring higher CWR than that of LnMd (see Figure 6.22). The core region shape features a triangle-like form with a broad "bottom" and narrow "top", while the previous NSPn features a broader "top" than the "bottom" as shown in Figure 6.7. In other words, the wave period range where LtCt could capture competitive wave energy becomes narrow as B_{PTO} increasing.

Under small B_{PTO} conditions, though, the LtCt case captures in a broader range than the NSPn case.

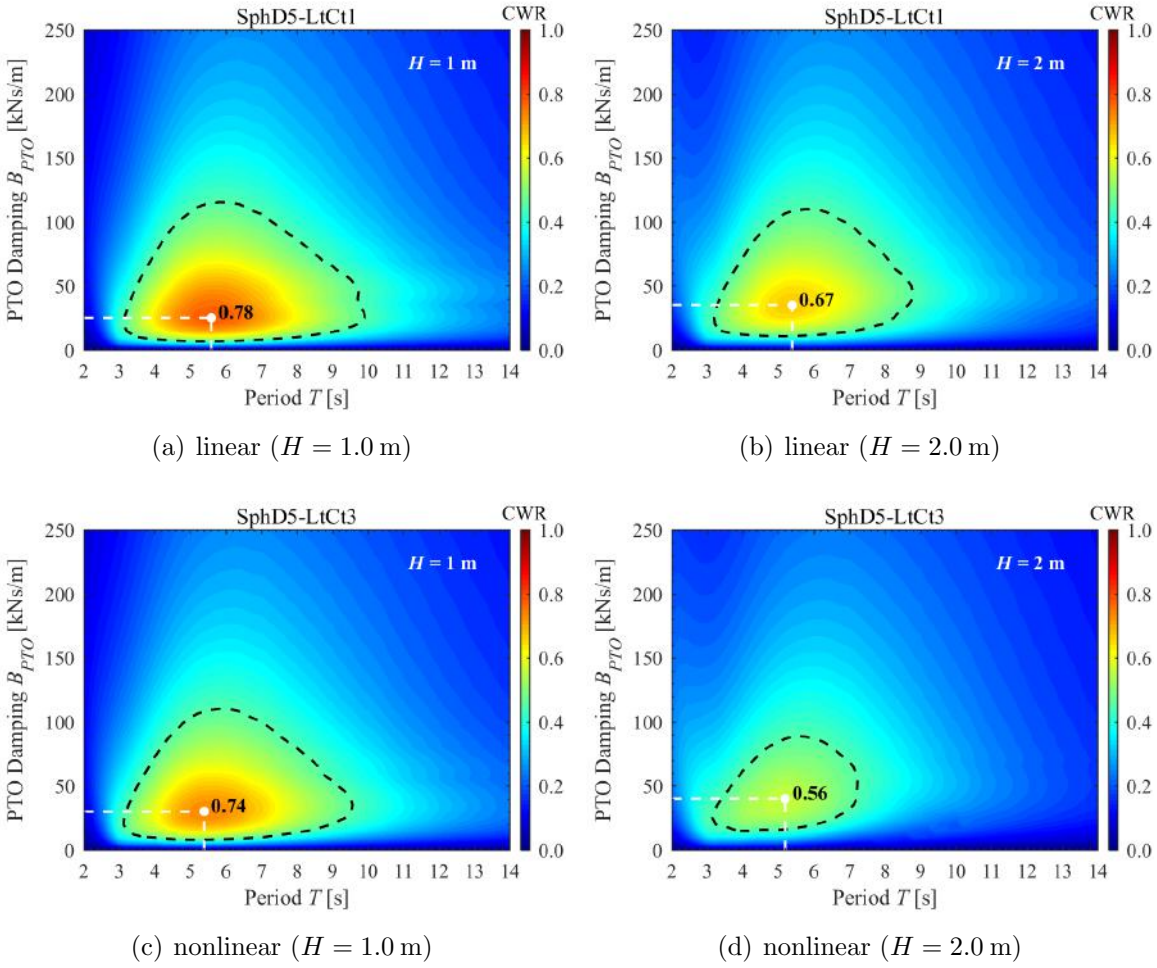

(a) linear ($H = 1.0$ m)

(b) linear ($H = 2.0$ m)

(c) nonlinear ($H = 1.0$ m)

(d) nonlinear ($H = 2.0$ m)

Figure 6.22: LtCt CWR using linear and nonlinear models ($H = 1.0,\ 2.0$ m)

Figure 6.23 presents the optimal CWR (the optimal result in the tuned CWR contour) and the corresponding latching duration (LD) with optimal B_{PTO} under wave conditions with three different wave steepnesses. The black dashed curve depicts the LD calculated analytically based on the formula (Eq. 2.1). Due to the nonlinear Froude-Krylov force model, the real optimal LD is smaller than the analytical one. Besides, such a tendency becomes more significant as both wave period and wave steepness increase. It means the nonlinear effect gets stronger. It is also shown that the present LtCt is far more suitable for the wave with a moderate period, such as from 4.0 to 8.0 s according to the CWR curves.

Moreover, not only the wave period with respect to the CWR peak in the NSPn contours is larger than that of LtCt (as shown in Figure 6.24), increasing B_{PTO} also shifts the optimal wave period to an even large value. In Figure 6.24 one observes that, using the nonlinear Froude-Krylov force model, the peak period for LtCt does not change too much though latching control increases the resonance period, while

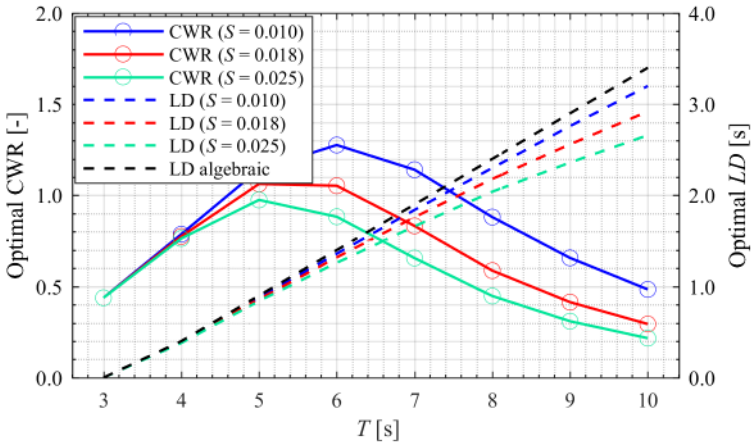

Figure 6.23: Optimal CWR and LD for different wave conditions

for NSPn it increases significantly, especially for cases with small α and γ values.

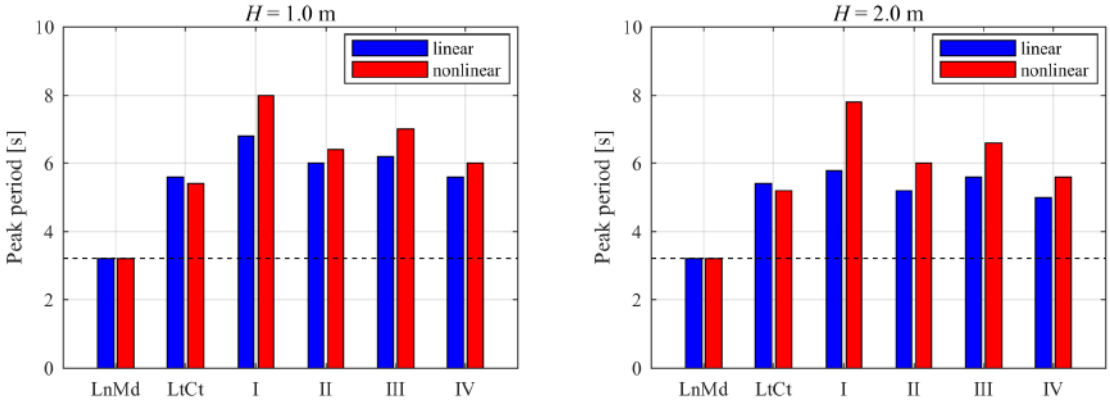

(a) $H = 1.0$ m (b) $H = 2.0$ m

Figure 6.24: Peak period comparisons of different models in regular wave conditions

In Figure 6.25, it is shown that the linear model obviously overestimates the CWR, especially for the NSPn case. Therefore, it indicates that the nonlinear model would be necessary for the prediction of wave energy conversion with NSPn. Besides, it should be noticed that the QZS configuration does not always perform better than mono-stable ones.

In summary, the above comparisons indicate that the NSPn achieves competitive wave energy harvest under a relatively long wave condition, even outperforms LtCt if it involves large B_{PTO}.

6.6.2 Performance in a given sea site

Continually, the performance comparisons in the nearshore region of Rio de Janeiro include four situations :

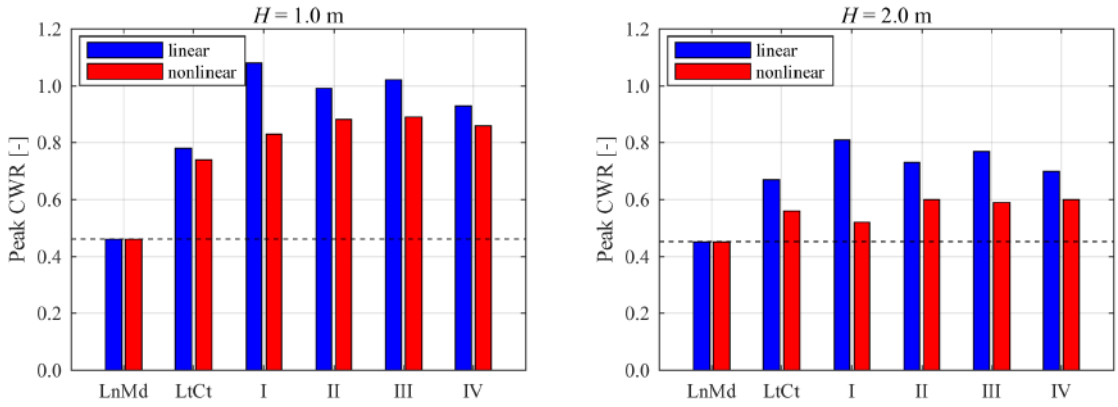

(a) $H = 1.0\,\mathrm{m}$ (b) $H = 2.0\,\mathrm{m}$

Figure 6.25: Peak CWR comparisons of different models in regular wave conditions

- Non-constrained & untuned – no displacement limit and applies one optimal B_{PTO} for all the sea states;
- Non-constrained & tuned – no displacement limit, however, applies different optimal B_{PTO} for each sea state;
- Constrained & untuned – considers the displacement limit ($z_{\mathrm{lim}} = 2.5\,\mathrm{m}$) and applies one optimal B_{PTO} for all the sea states;
- Constrained & tuned – considers the displacement limit ($z_{\mathrm{lim}} = 2.5\,\mathrm{m}$), however, applies different optimal B_{PTO} for each sea state.

Both cases without drag correction and with $C_d = 0.6$ considered in the comparisons. Figure 6.26 depicts the AEP.

First, the most evident phenomenon is that the AEPs in Figure 6.26 (c) present great decreasing compared with the other three cases, especially, for the four items of NSPn. It is because that for LtCt and NSPn, the motion is amplified, so larger probability exceeding the excursion limit appears. Thus in the constrained & untuned condition, a very large damping makes the motion satisfy all the sea states. For instance, in the SS9, the damping larger than 300 kNs/m is required. Therefore, the system is forced to work in an overdamped situation for those less energetic sea states.

Consequently, from the dramatic increase of AEP for the NSPn items in Figure 6.26 (d) one can conclude that NSPn can achieve around twice increase relative to LnMd and one time increase compared with LtCt if the system can be tuned for distinct sea states. For the sea states form SS1 to SS6, which occupy 97.2% of the occurrence and 86.7% power density, the maximum B_{PTO} that satisfies the constrained condition is around 150 kNs/m in SS6 which is almost half of that in SS9.

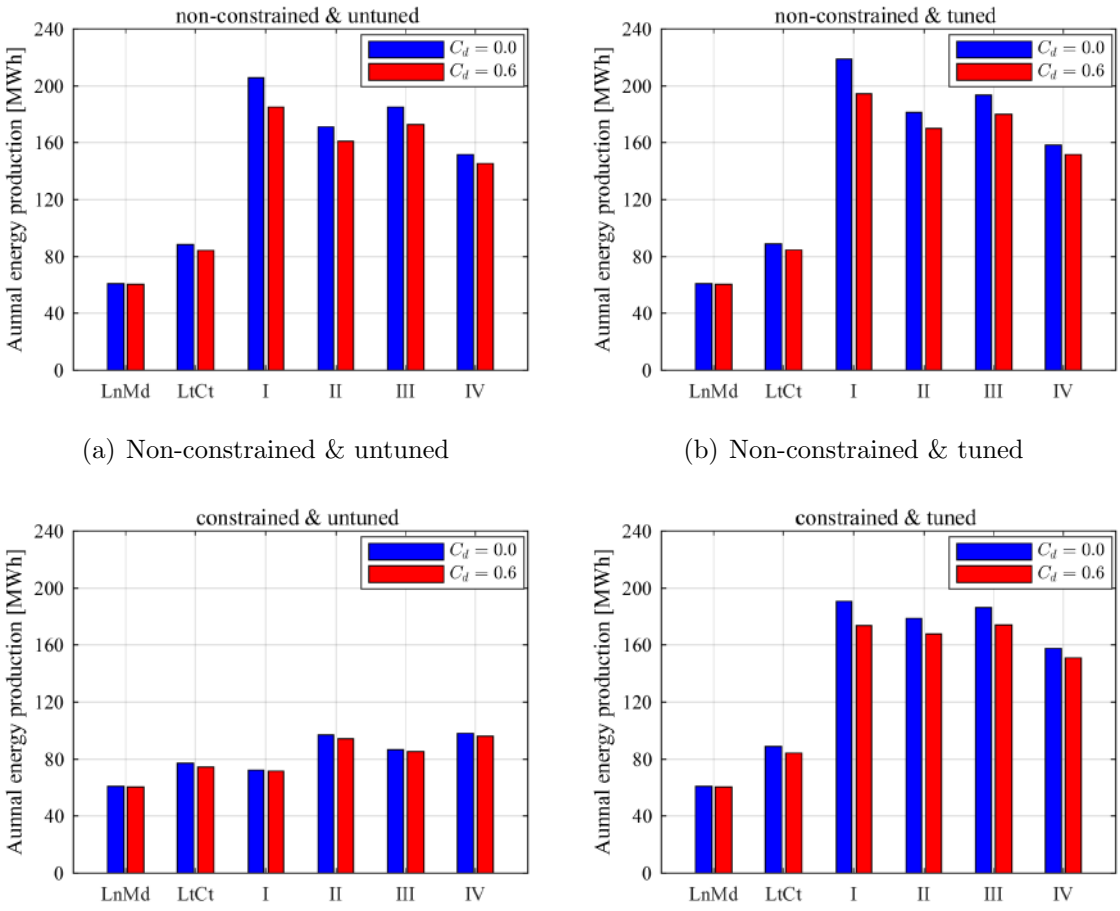

(a) Non-constrained & untuned

(b) Non-constrained & tuned

(c) Constrained & untuned

(d) Constrained & tuned

Figure 6.26: AEPs for four cases

Besides, due to larger damping is adopted to satisfy the motion constraint, the effect of C_d on the constrained & tuned case becomes weaker, even less than 10%.

In the four items of NSPn, I, II and III can capture a little more energy than IV in Figure 6.26 (d), however, item I presents the largest decrease in Figure 6.26 (c). It means that item I depends more on the large motion to increase the power absorption. To release the stress of exceeding motion limit, item III with a larger α in mono-stable configuration is more suitable.

Figure 6.27 presents another important parameter that can evaluate the quality of power absorption: peak-to-average power ratio (P_{max}/P_m). The vacuum circles depict the case without drag correction, while the solid dots describe the case with $C_d = 0.6$.

Obviously, all the NSPn items feature a less P_{max}/P_m value than LtCt until SS7, which means that NSPn can achieve smoother power capture. However, for the highly energetic sea states, SS8 and SS9, the items I and II of NSPn cannot absorb wave energy as smoothly as LtCt and LnMd.

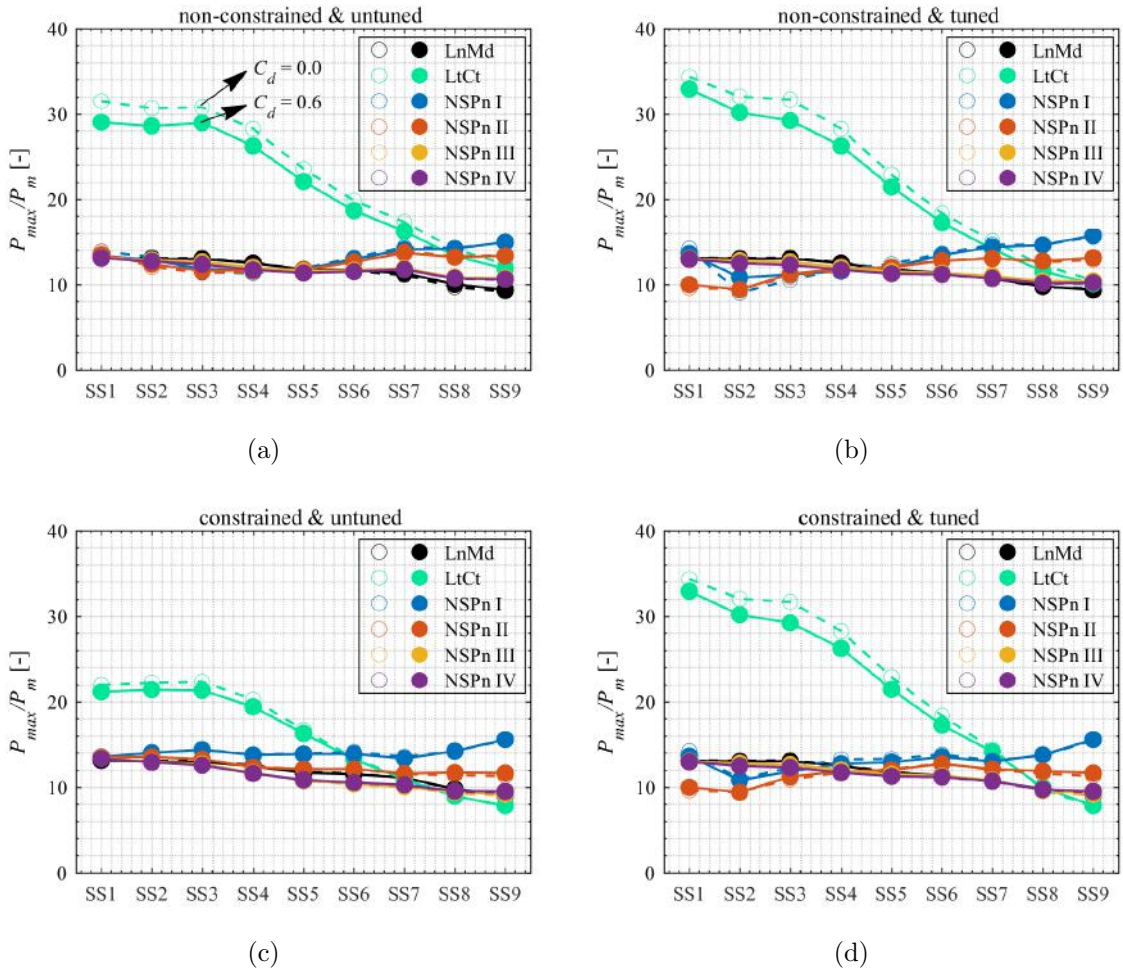

Figure 6.27: Ratio of peak power to mean power for four cases

Finally, considering both quantity and quality of power absorption, a mono-stable NSPn with α close to 1.0 and not too large γ, such as item III, is the best choice, even outperforms LtCt.

6.7 Summary

This chapter investigates both static and dynamic characteristics of the NSPn comprehensively, as an alternative substitution for the NSMc. Through the feasibility analysis, it is observed that the effect of constraints on NSPn configurations is not as significant as that on NSMc.

The consequent comparisons with LnMd and LtCt also verify that NSPn can outperform LtCt with constant latching duration in both quantity and quality aspects.

Furthermore, a mono-stable NSPn with α close to 1.0 and not too large γ is recommended in the wave energy conversion applications.

Chapter 7

Conclusions and Future Work

7.1 Conclusions

The thesis investigates the nonlinear stiffness concept in improving wave energy conversion for a point absorber type wave energy converter, as the original narrow bandwidth and short natural period cannot achieve efficient wave energy conversion when the wave period is out of the resonance period, not to mention that the real sea states are random naturally.

The WEC is featured in one widely studied shape – sphere. Due to its non-uniform waterplane area, the weakly nonlinear Froude-Krylov force model is implemented to conduct more accurate simulations.

Two types of nonlinear stiffness systems are investigated, including the system composed of mechanical compression springs – NSMc; and the system composed of pneumatic cylinders – NSPn.

One set of in-house code is established to simulate and analyze the WEC dynamics. To verify the code, a series of numerical tests are conducted and compared with the results from the International Energy Agency (IEA) Ocean Energy Systems (OES) Task 10 project.

7.1.1 Nonlinear Froude-Krylov force model

Both the meshing and analytical approaches are included:

- The meshing approach is one direct method to use Bernoulli's equation to calculate the Froude-Krylov force over the meshes by discretizing the instantaneous wetted surface. In the code-to-code verifications – free decay tests, simulations in regular wave conditions and irregular wave conditions, the good consistency determines that it can be taken as a reference for the verification of the analytical nonlinear Froude-Krylov force model;

- The present work also improves the analytical nonlinear model. Through adopting the Bessel function, more comprehensive expression of nonlinear Froude-Krylov force is proposed. Using the adaptive polynomial fitting technique, instead of Taylor's series expansion, both the Bessel function and exponential function could be approximated with higher accuracy under a wider wave frequency domain. Simultaneously, the separation of the frequency-dependent term from the relative real-time updated relative displacement improves the computational efficiency, especially in irregular wave conditions with multiple frequency components. In the extensive numerical simulations, the accuracy and efficiency of the analytical approach are validated through comparisons with the meshing approach.

In addition, the nonlinear effect of the non-uniform waterplane area also interacts with the NSS to change both static and dynamic characteristics of PA type WEC.

7.1.2 NSS characteristics

The static analysis of the classical NSMc describes three types of configurations: bi-stable, QZS (Quasi-Zero Stiffness), and mono-stable, which are determined by both stiffness and geometry ratios. However, for the NSPn, though two novel equivalent non-dimensional parameters are defined similarly to that in NSMc analysis, only the equivalent stiffness ratio determines the system behavior. In addition, the dynamic analysis presents that the equivalent stiffness ratio plays a more important role than the equivalent geometry ratio in affecting the system response. Consequently, the gas pressure inside of the pneumatic system P_0 affects the characteristics most.

In the feasibility analysis, this thesis sets up one procedure of determining the feasible region of NSMc parameters according to the conventional design procedure of mechanical compression springs. While, the NSPn feasible region is set up according to the parameters' range in the industry application, together with the consideration fo rod buckling condition. Considering such practical limitations, most parts of the attractive configurations that can improve the wave absorption for the NSMc are not feasible anymore. Thus, the NSMc advantages are dramatically weakened. However, these constraints do not restrict the NSPn's attractive (α, γ) area dramatically. Thus its annual energy production (AEP) is not reduced too much. Such a discovery inherently verifies that the NSPn features better feasibility than NSMc.

7.1.3 NSS with nonlinear Froude-Krylov force model

Not considering the nonlinear Froude-Krylov force model, the NSS function is over-estimated, when implementing the NSS in the PA type WEC with non-uniform

waterplane area. With the nonlinear Froude-Krylov force model, the resonance response is even pushed to the larger period range, as well as the response bandwidth is broadened.

The combination of the NSS concept with nonlinear Froude-Krylov force model makes the bi-stable configurations produce multiple solutions more easily. Such a more significant motion instability reduces the WEC's power absorption in both regular and irregular conditions. However, the QZS and mono-stable configurations still feature stable enough motion. Especially, some mono-stable configurations close to the QZS perform even better.

The comparison with latching control method conducted under the wave climate in the nearshore region of Rio de Janeiro, Brazil, imposes that PA could harvest more power with the NSPn, than with latching control, featuring almost once increase. Moreover, the lower peak-to-average power ratio verifies that the process of power absorption is smoother with the NSPn. Thus, the NSPn outperforms latching control in both quantity and quality of wave energy conversion.

7.2 Future work

Besides the thesis work, the nonlinear stiffness concept deserves deeper investigation.

The following work will continue to strengthen the understanding of NSPn characteristics and promote its application in wave energy conversion, such as,

- Setting up a finer mathematical model of NSPn through the scaled model test. It may be a set of dry tests to emulate the NSPn static and dynamic characteristics;
- Conducting more comparisons with other approaches, e.g., threshold latching, MPC, etc. and with different sea states. Thus, the NSPn adaptability would be investigated comprehensively;
- Investigating better approaches to handle the motion limit problem, for instance, adopting minor adjust of the pneumatic system to restrict the excessive motion, or designing a suitable end-stop system, etc.

In addition, not limited to the NSPn, the interactions of NSS with other relevant concepts will be an alternative approach to give full play to the advantages individually and overcome their limitations.

- Searching for the optimal geometric dimension and shape with the non-uniform waterplane area by using the analytical approach to solve the hydrodynamic problem. For instance, to protect the device in high sea states, increasing the

waterplane area around the motion stroke limit would behave as a moderate end-stop mechanism. Together with NSS, these two types of nonlinear effects interactions may bring more benefits to WEC;

- In the WEC offshore applications, combining NSS with the two-body system is one hopeful approach. Moreover, the broad bandwidth characteristic of the NSS concept and the multiple resonances of the two-body system would enhance the performance of WEC in different sea states together.

Bibliography

[1] ENERDATA. "Global energy statistical yearbook". 2019. Available in: <https://yearbook.enerdata.net>. Accessed in: 2019-10-14.

[2] LEWIS, A., ESTEFEN, S., HUCKERBY, J., et al. "Ocean Energy". In: Edenhofer, O., Pichs-Madruga, R., Sokona, Y., et al. (Eds.), *IPCC Special Report on Renewable Energy Sources and Climate Change Mitigation*, cap. 6, pp. 497–534, Cambridge, United Kingdom and New York, NY, USA, Cambridge University Press, 2011.

[3] SIMS, R. E., SCHOCK, R. N., ADEGBULULGBE, A., et al. "Energy Supply". In: Metz, B., Davidson, O., Bosch, P., et al. (Eds.), *Climate Change 2007: Mitigation. Contribution of Working Group III to the Fourth Assessment Report of the Intergovernmental Panel on Climate Change*, cap. 4, pp. 251–322, Cambridge, United Kingdom and New York, NY, USA, Cambridge University Press, 2007.

[4] RUUD, K., FRANK, N. *Wave Energy Technology Brief*. Technical report, IRENA, 2014.

[5] FOWLER, M. J., OWENS, B., BULL, D., et al. "Hydrodynamic Module Coupling in the Offshore Wind Energy Simulation (OWENS) Toolkit". In: *ASME 2014 33rd International Conference on Ocean, Offshore and Arctic Engineering*. American Society of Mechanical Engineers Digital Collection, 2014.

[6] SHADMAN, M., SILVA, C., FALLER, D., et al. "Ocean Renewable Energy Potential, Technology, and Deployments: A Case Study of Brazil", *Energies*, v. 12, n. 19, pp. 3658, 2019.

[7] SHENG, W. "Wave energy conversion and hydrodynamics modelling technologies: A review", *Renewable and Sustainable Energy Reviews*, v. 109, pp. 482–498, 2019.

[8] MARIA-ARENAS, A., GARRIDO, A. J., RUSU, E., et al. "Control Strategies Applied to Wave Energy Converters: State of the Art", *Energies*, v. 12, n. 16, pp. 3115, 2019.

[9] JIN, S., PATTON, R. J., GUO, B. "Enhancement of wave energy absorption efficiency via geometry and power take-off damping tuning", *Energy*, v. 169, pp. 819–832, 2019.

[10] RODRÍGUEZ, C. A., ROSA-SANTOS, P., TAVEIRA-PINTO, F. "Assessment of damping coefficients of power take-off systems of wave energy converters: A hybrid approach", *Energy*, v. 169, pp. 1022–1038, 2019.

[11] GARCIA-ROSA, P. B., KULIA, G., RINGWOOD, J. V., et al. "Real-Time Passive Control of Wave Energy Converters Using the Hilbert-Huang Transform", *IFAC-PapersOnLine*, v. 50, n. 1, pp. 14705–14710, 2017.

[12] BUDAL, K., FALNES, J. "System for the conversion of sea wave energy". 1980. US Patent 4,203,294.

[13] ANTÓNIO, F. D. O. "Phase control through load control of oscillating-body wave energy converters with hydraulic PTO system", *Ocean Engineering*, v. 35, n. 3-4, pp. 358–366, 2008.

[14] LOPES, M., TODALSHAUG, J. H., GOMES, R., et al. "Experimental and numerical investigation of non-predictive phase-control strategies for a point-absorbing wave energy converter", *Ocean Engineering*, v. 36, n. 5, pp. 386–402, 2009.

[15] SHENG, W., ALCORN, R., LEWIS, A. "On improving wave energy conversion, part II: Development of latching control technologies", *Renewable energy*, v. 75, pp. 935–944, 2015.

[16] BABARIT, A., DUCLOS, G., CLÉMENT, A. H. "Comparison of latching control strategies for a heaving wave energy device in random sea", *Applied Ocean Research*, v. 26, n. 5, pp. 227–238, 2004.

[17] BABARIT, A., GUGLIELMI, M., CLÉMENT, A. H. "Declutching control of a wave energy converter", *Ocean Engineering*, v. 36, n. 12-13, pp. 1015–1024, 2009.

[18] TODALSHAUG, J. H., FALNES, J., MOAN, T. "A comparison of selected strategies for adaptive control of wave energy converters", *Journal of Offshore Mechanics and Arctic Engineering*, v. 133, n. 3, pp. 031101, 2011.

[19] GENEST, R., RINGWOOD, J. V. "A critical comparison of model-predictive and pseudospectral control for wave energy devices", *Journal of Ocean Engineering and Marine Energy*, v. 2, n. 4, pp. 485–499, 2016.

[20] NGUYEN, H.-N., SABIRON, G., TONA, P., et al. "Experimental validation of a nonlinear MPC strategy for a wave energy converter prototype". In: *ASME 2016 35th international conference on ocean, offshore and arctic engineering*. American Society of Mechanical Engineers Digital Collection, 2016.

[21] SON, D., YEUNG, R. W. "Optimizing ocean-wave energy extraction of a dual coaxial-cylinder WEC using nonlinear model predictive control", *Applied energy*, v. 187, pp. 746–757, 2017.

[22] FAEDO, N., OLAYA, S., RINGWOOD, J. V. "Optimal control, MPC and MPC-like algorithms for wave energy systems: An overview", *IFAC Journal of Systems and Control*, v. 1, pp. 37–56, 2017.

[23] SÁNCHEZ, E. V., HANSEN, R. H., KRAMER, M. M. "Control performance assessment and design of optimal control to harvest ocean energy", *IEEE Journal of Oceanic Engineering*, v. 40, n. 1, pp. 15–26, 2014.

[24] NGUYEN, H.-N., TONA, P. "Continuously adaptive PI control of wave energy converters under irregular sea-state conditions". 2017.

[25] NGUYEN, H.-N., TONA, P. "An efficiency-aware continuous adaptive proportional-integral velocity-feedback control for wave energy converters", *Renewable Energy*, v. 146, pp. 1596–1608, 2020.

[26] FOLLEY, M. *Numerical modelling of wave energy converters: state-of-the-art techniques for single devices and arrays*. Academic Press, 2016.

[27] ANDERLINI, E., FOREHAND, D. I., STANSELL, P., et al. "Control of a point absorber using reinforcement learning", *IEEE Transactions on Sustainable Energy*, v. 7, n. 4, pp. 1681–1690, 2016.

[28] ANDERLINI, E., FOREHAND, D. I., BANNON, E., et al. "Reactive control of a two-body point absorber using reinforcement learning", *Ocean Engineering*, v. 148, pp. 650–658, 2018.

[29] KORDE, U. A., RINGWOOD, J. *Hydrodynamic control of wave energy devices*. Cambridge University Press, 2016.

[30] ENGSTRÖM, J., KURUPATH, V., ISBERG, J., et al. "A resonant two body system for a point absorbing wave energy converter with direct-driven linear generator", *Journal of applied physics*, v. 110, n. 12, pp. 124904, 2011.

[31] AL SHAMI, E., WANG, X., ZHANG, R., et al. "A parameter study and optimization of two body wave energy converters", *Renewable energy*, v. 131, pp. 1–13, 2019.

[32] ZHANG, X., YANG, J. "Power capture performance of an oscillating-body WEC with nonlinear snap through PTO systems in irregular waves", *Applied Ocean Research*, v. 52, pp. 261–273, 2015.

[33] TODALSHAUG, J. H. "Wave Energy Converter". 2016. US Patent App. 15/111,659.

[34] HARNE, R. L., WANG, K. "A review of the recent research on vibration energy harvesting via bistable systems", *Smart materials and structures*, v. 22, n. 2, pp. 023001, 2013.

[35] HARNE, R. L., WANG, K.-W. *Harnessing bistable structural dynamics: for vibration control, energy harvesting and sensing*. John Wiley & Sons, 2017.

[36] OCEAN ENERGY SYSTEMS. "Wave Energy Converters Modelling Verification and Validation". 2019. Available in: <https://www.ocean-energy-systems.org/oes-projects/wave-energy-converters-modelling-verification-and-validation/>. Accessed in: 2019-08-09.

[37] RINGWOOD, J. V., BACELLI, G., FUSCO, F. "Energy-maximizing control of wave-energy converters: The development of control system technology to optimize their operation", *IEEE control systems magazine*, v. 34, n. 5, pp. 30–55, 2014.

[38] OZKOP, E., ALTAS, I. H. "Control, power and electrical components in wave energy conversion systems: A review of the technologies", *Renewable and Sustainable Energy Reviews*, v. 67, pp. 106–115, 2017.

[39] KORDE, U. A. "Systems of reactively loaded coupled oscillating bodies in wave energy conversion", *Applied ocean research*, v. 25, n. 2, pp. 79–91, 2003.

[40] FRENCH, M. "On the difficulty of inventing an economical sea wave energy converter: a personal view", *Proceedings of the Institution of Mechanical*

Engineers, Part M: Journal of Engineering for the Maritime Environment, v. 220, n. 3, pp. 149–155, 2006.

[41] CHEN, Z., ZHANG, L., YEUNG, R. W. "Analysis and optimization of a Dual Mass-Spring-Damper (DMSD) wave-energy convertor with variable resonance capability", *Renewable energy*, v. 131, pp. 1060–1072, 2019.

[42] TODALSHAUG, J. H., ÁSGEIRSSON, G. S., HJÁLMARSSON, E., et al. "Tank testing of an inherently phase-controlled wave energy converter", *International Journal of Marine Energy*, v. 15, pp. 68–84, 2016.

[43] TEILLANT, B., KRÜGEL, K., GUÉRINEL, M., et al. *Engineering challenges related to full scale and large deployment implementation of the proposed breakthroughs*. Technical report, WavEC Offshore Renewables Teamwork, 2016.

[44] ROVEDA, S. *Numerical assessment of negative spring on spar OWC based in the IVV method*. Master's dissertation, University of Lisbon, 2016.

[45] GRADOWSKI, M., ALVES, M., GOMES, R. P., et al. "Integration of a Hydrodynamic Negative Spring Concept into the OWC Spar Buoy". In: *Proceedings of the 12th European Wave and Tidal Energy Conference, Aug*, 2017.

[46] KURNIAWAN, A., GREAVES, D., CHAPLIN, J. "Wave energy devices with compressible volumes", *Proceedings of the Royal Society A: Mathematical, Physical and Engineering Sciences*, v. 470, n. 2172, pp. 20140559, 2014.

[47] KURNIAWAN, A., CHAPLIN, J., GREAVES, D., et al. "Wave energy absorption by a floating air bag", *Journal of Fluid Mechanics*, v. 812, pp. 294–320, 2017.

[48] BUDAL, K., FALNES, J. "Wave power conversion by point absorbers: a Norwegian project", *International Journal of Ambient Energy*, v. 3, n. 2, pp. 59–67, 1982.

[49] BUDAL, K., FALNES, J., IVERSEN, L. C., et al. "The Norwegian wave-power buoy project". In: *The second international symposium on wave energy utilization*, 1982.

[50] PEÑALBA RETES, M., MÉRIGAUD, A., GILLOTEAUX, J.-C., et al. "Nonlinear Froude-Krylov force modelling for two heaving wave energy point absorbers". In: *Proceedings of the 11th European Wave and Tidal Energy Conference*. European Wave and Tidal Energy Conference 2015, 2015.

[51] FENG, Z., KERRIGAN, E. C. "Latching control of wave energy converters using derivative-free optimization". In: *52nd IEEE Conference on Decision and Control*, pp. 7474–7479. IEEE, 2013.

[52] ANTÓNIO, F. D. O., JUSTINO, P. A., HENRIQUES, J. C., et al. "Reactive versus latching phase control of a two-body heaving wave energy converter". In: *2009 European Control Conference (ECC)*, pp. 3731–3736. IEEE, 2009.

[53] EIDSMOEN, H. *Simulation of a slack-moored heaving-buoy wave-energy converter with phase control*. Technical report, Division of Physics, Norwegian University of Science and Technology NTNU, Trondheim, 1996.

[54] TODALSHAUG, J. H., BJARTE-LARSSON, T., FALNES, J. "Optimum reactive control and control by latching of a wave-absorbing semisubmerged heaving sphere". In: *ASME 2002 21st International Conference on Offshore Mechanics and Arctic Engineering*, pp. 415–423. American Society of Mechanical Engineers Digital Collection, 2009.

[55] PASALA, D., SARLIS, A., NAGARAJAIAH, S., et al. "Adaptive negative stiffness: New structural modification approach for seismic protection", *Journal of Structural Engineering*, v. 139, n. 7, pp. 1112–1123, 2012.

[56] SARLIS, A. A., PASALA, D. T. R., CONSTANTINOU, M., et al. "Negative stiffness device for seismic protection of structures", *Journal of Structural Engineering*, v. 139, n. 7, pp. 1124–1133, 2012.

[57] CHURCHILL, C. B., SHAHAN, D. W., SMITH, S. P., et al. "Dynamically variable negative stiffness structures", *Science advances*, v. 2, n. 2, pp. e1500778, 2016.

[58] PALOMARES, E., NIETO, A., MORALES, A., et al. "Numerical and experimental analysis of a vibration isolator equipped with a negative stiffness system", *Journal of Sound and Vibration*, v. 414, pp. 31–42, 2018.

[59] RAMLAN, R., BRENNAN, M., MACE, B., et al. "Potential benefits of a non-linear stiffness in an energy harvesting device", *Nonlinear dynamics*, v. 59, n. 4, pp. 545–558, 2010.

[60] DAQAQ, M. F., MASANA, R., ERTURK, A., et al. "On the role of nonlinearities in vibratory energy harvesting: a critical review and discussion", *Applied Mechanics Reviews*, v. 66, n. 4, 2014.

[61] SHAN, G., WANG, D. F., SONG, J., et al. "A spring-assisted adaptive bistable energy harvester for high output in low-excitation", *Microsystem Technologies*, v. 24, n. 9, pp. 3579–3588, 2018.

[62] ZHANG, X., YANG, J., XIAO, L., et al. "Numerical study of an oscillating wave energy converter with nonlinear snap-through power-take-off systems in regular waves". In: *The twenty-fourth international ocean and polar engineering conference*. International Society of Offshore and Polar Engineers, 2014.

[63] ZHANG, X., TIAN, X., XIAO, L., et al. "Application of an adaptive bistable power capture mechanism to a point absorber wave energy converter", *Applied energy*, v. 228, pp. 450–467, 2018.

[64] ZHANG, X., TIAN, X., XIAO, L., et al. "Mechanism and sensitivity for broadband energy harvesting of an adaptive bistable point absorber wave energy converter", *Energy*, v. 188, pp. 115984, 2019.

[65] CORPOWER. "CorPower". 2019. Available in: <`http://www.corpowerocean.com/`>. Accessed in: 2019-09-24.

[66] PERETTA, S., RUOL, P., MARTINELLI, L., et al. "Effect of a negative stiffness mechanism on the performance of the WEPTOS rotors". In: *International Conference on Computational Methods in Marine Engineering*, pp. 58–72. CNR, 2015.

[67] KURNIAWAN, A., ZHANG, X. "Application of a Negative Stiffness Mechanism on Pitching Wave Energy Devices". In: *5th Offshore Energy and Storage Symposium*, 2018.

[68] WANG, L., TANG, H., WU, Y. "On a submerged wave energy converter with snap-through power take-off", *Applied Ocean Research*, v. 80, pp. 24–36, 2018.

[69] TÊTU, A., FERRI, F., KRAMER, M., et al. "Physical and Mathematical Modeling of a Wave Energy Converter Equipped with a Negative Spring Mechanism for Phase Control", *Energies*, v. 11, n. 9, pp. 2362, 2018.

[70] YOUNESIAN, D., ALAM, M.-R. "Multi-stable mechanisms for high-efficiency and broadband ocean wave energy harvesting", *Applied energy*, v. 197, pp. 292–302, 2017.

[71] LI, L., ZHANG, X., YUAN, Z., et al. "Multi-stable mechanism of an oscillating-body wave energy converter", *IEEE Transactions on Sustainable Energy*, 2019.

[72] HARNE, R., SCHOEMAKER, M., DUSSAULT, B., et al. "Wave heave energy conversion using modular multistability", *Applied energy*, v. 130, pp. 148–156, 2014.

[73] XIAO, X., XIAO, L., PENG, T. "Comparative study on power capture performance of oscillating-body wave energy converters with three novel power take-off systems", *Renewable energy*, v. 103, pp. 94–105, 2017.

[74] ZHANG, H., XI, R., XU, D., et al. "Efficiency enhancement of a point wave energy converter with a magnetic bistable mechanism", *Energy*, 2019.

[75] BACELLI, G., NEARY, V. S., MURPHY, A. W. *Damping optimization for wave energy converters with compressible volumes.* Technical report, Sandia National Lab, Albuquerque, NM (United States), 2016.

[76] GILLOTEAUX, J.-C., DUCROZET, G., BABARIT, A., et al. "Non-linear model to simulate large amplitude motions: application to wave energy conversion". In: *22nd International Workshop on Water Waves and Floating Bodies*, 2007.

[77] GILLOTEAUX, J.-C., BABARIT, A., DUCROZET, G., et al. "A non-linear potential model to predict large-amplitudes-motions: application to the SEAREV wave energy converter". In: *ASME 2007 26th International Conference on Offshore Mechanics and Arctic Engineering*, pp. 529–535. American Society of Mechanical Engineers Digital Collection, 2009.

[78] MÉRIGAUD, A., GILLOTEAUX, J.-C., RINGWOOD, J. V. "A nonlinear extension for linear boundary element methods in wave energy device modelling". In: *ASME 2012 31st International Conference on Ocean, Offshore and Arctic Engineering*, pp. 615–621. American Society of Mechanical Engineers Digital Collection, 2013.

[79] YU, Y.-H., RUEHL, K., RIJ, J. V., et al. "WEC-Sim Theosy". 2019. Available in: <`https://wec-sim.github.io/WEC-Sim/theory`>. Accessed in: 2019-10-15.

[80] GIORGI, G., RINGWOOD, J. V. "Nonlinear Froude-Krylov and viscous drag representations for wave energy converters in the computation/fidelity continuum", *Ocean Engineering*, v. 141, pp. 164–175, 2017.

[81] GIORGI, G., RINGWOOD, J. V. "Computationally efficient nonlinear Froude–Krylov force calculations for heaving axisymmetric wave energy point absorbers", *Journal of Ocean Engineering and Marine Energy*, v. 3, n. 1, pp. 21–33, 2017.

[82] GIORGI, G., RINGWOOD, J. V. "Comparing nonlinear hydrodynamic forces in heaving point absorbers and oscillating wave surge converters", *Journal of Ocean Engineering and Marine Energy*, v. 4, n. 1, pp. 25–35, 2018.

[83] GIORGI, G., RINGWOOD, J. V. "Analytical representation of nonlinear Froude-Krylov forces for 3-DoF point absorbing wave energy devices", *Ocean Engineering*, v. 164, pp. 749–759, 2018.

[84] CONG, D., SHANG, J., LUO, Z., et al. "Energy Efficiency Analysis of Multi-Type Floating Bodies for a Novel Heaving Point Absorber with Application to Low-Power Unmanned Ocean Device", *Energies*, v. 11, n. 12, pp. 3282, 2018.

[85] MÉRIGAUD, A., RINGWOOD, J. V. "Power production assessment for wave energy converters: Overcoming the perils of the power matrix", *Proceedings of the Institution of Mechanical Engineers, Part M: Journal of Engineering for the Maritime Environment*, v. 232, n. 1, pp. 50–70, 2018.

[86] CUMMINS, W. *The impulse response function and ship motions.* Technical report, David Taylor Model Basin Washington DC, 1962.

[87] PEÑALBA RETES, M., GIORGI, G., RINGWOOD, J. V. "Mathematical modelling of wave energy converters: a review of nonlinear approaches", *Renewable and Sustainable Energy Reviews*, v. 78, pp. 1188–1207, 2017.

[88] PECHER, A., KOFOED, J. P. *Handbook of ocean wave energy.* Springer London, 2017.

[89] FALNES, J. *Ocean waves and oscillating systems: linear interactions including wave-energy extraction.* Cambridge university press, 2002.

[90] LEE, C.-H. *WAMIT Theory Manual*, 1995.

[91] ANSYS INC. *Aqwa Theory Manual*, 2015.

[92] BABARIT, A., DELHOMMEAU, G. "Theoretical and numerical aspects of the open source BEM solver NEMOH". 2015.

[93] HULME, A. "The wave forces acting on a floating hemisphere undergoing forced periodic oscillations", *Journal of Fluid Mechanics*, v. 121, pp. 443–463, 1982.

[94] YEUNG, R. W. "Added mass and damping of a vertical cylinder in finite-depth waters", *Applied Ocean Research*, v. 3, n. 3, pp. 119–133, 1981.

[95] PÉREZ, T., FOSSEN, T. I. "Time-vs. frequency-domain identification of parametric radiation force models for marine structures at zero speed", *Modeling, Identification and Control: A Norwegian Research Bulletin*, v. 29, n. 1, pp. 1–19, 2008.

[96] PÉREZ, T., FOSSEN, T. I. "A matlab toolbox for parametric identification of radiation-force models of ships and offshore structures", 2009.

[97] ABRAMOWITZ, M., STEGUN, I. *Handbook of mathematical functions: with formulas, graphs, and mathematical tables*, v. 55. Courier Corporation, 1965.

[98] GIORGI, G., RINGWOOD, J. V. "Consistency of viscous drag identification tests for wave energy applications". In: *Proceedings of the 12th European Wave and Tidal Energy Conference (EWTEC), Cork, Ireland*, v. 27, 2017.

[99] JIN, S., PATTON, R. J., GUO, B. "Viscosity effect on a point absorber wave energy converter hydrodynamics validated by simulation and experiment", *Renewable energy*, v. 129, pp. 500–512, 2018.

[100] BABARIT, A., TODALSHAUG, J. H., MULIAWAN, M., et al. "Numerical benchmarking study of a selection of wave energy converters", *Renewable Energy*, v. 41, pp. 44–63, 2012.

[101] JOURNÉE, J., MASSIE, W. *Offshore Hydromechanics*. TU Delft.

[102] FALNES, J. "A review of wave-energy extraction", *Marine structures*, v. 20, n. 4, pp. 185–201, 2007.

[103] NIELSEN, K., PONTES, T. "Report T02-1.1 OES IA Annex II Task 1.2 Generic and Site-related Wave Energy Data", *Ocean Energy Systems IEA*, 2010.

[104] PASTOR, J., LIU, Y. "Wave climate resource analysis based on a revised gamma spectrum for wave energy conversion technology", *Sustainability*, v. 8, n. 12, pp. 1321, 2016.

[105] WENDT, F. F., YU, Y.-H., NIELSEN, K., et al. "International energy agency ocean energy systems task 10 wave energy converter modeling verification and validation". In: *12th European Wave and Tidal Energy Conference*. doi: 10.1109/TAP.2012.2196918.

[106] NIELSEN, K., WENDT, F. F., YU, Y.-H., et al. "OES Task 10 WEC heaving sphere performance modelling verification". In: *Proceedings of the 3rd International Conference on Renewable Energies Offshore (RENEW 2018)*, pp. 265–272.

[107] NAVE, C. R. "Potential Energy". 2016. Available in: <http://hyperphysics.phy-astr.gsu.edu/hbase/pegrav.html>. Accessed in: 2019-08-27.

[108] WIKIPEDIA CONTRIBUTORS. "Mechanical equilibrium". 2019. Available in: <https://en.wikipedia.org/wiki/Mechanical_equilibrium>. Accessed in: 2019-08-27.

[109] WU, Z., LEVI, C., ESTEFEN, S. F. "Wave energy harvesting using nonlinear stiffness system", *Applied Ocean Research*, v. 74, pp. 102–116, 2018.

[110] PÉREZ, T., FOSSEN, T. "FDI Toolbox". 2019. Available in: <https://github.com/cybergalactic/MSS>. Accessed in: 2019-10-22.

[111] WIKIPEDIA CONTRIBUTORS. "Coefficient of determination". 2019. Available in: <https://en.wikipedia.org/wiki/Coefficient_of_determination>. Accessed in: 2019-11-14.

[112] CHEN, X. B., DIEBOLD, L., DOUTRELEAU, Y. "New Green-function method to predict wave-induced ship motions and loads". In: *Twenty-Third Symposium on Naval HydrodynamicsOffice of Naval ResearchBassin d'Essais des CarenesNational Research Council*, 2001.

[113] DNV. "Environmental conditions and environmental loads", 2014.

[114] YU, Y., LIU, S. *Random wave and its applications to engineering*. Dalian University of Technology Press, Dalian, 2000.

[115] WU, Z., LEVI, C., ESTEFEN, S. F. "Practical considerations on nonlinear stiffness system for wave energy converter", *Applied Ocean Research*, v. 92, pp. 101935, 2019.

[116] BUDYNAS, R. G., NISBETT, J. K. *Shigley's Mechanical Engineering Design*. McGraw Hill, New York, 2009.

[117] BHANDARI, V. *Design of machine elements*. Tata McGraw-Hill Education, 2010.

[118] TUSTIN, A. "The effects of backlash and of speed-dependent friction on the stability of closed-cycle control systems", *Journal of the Institution of Electrical Engineers-Part IIA: Automatic Regulators and Servo Mechanisms*, v. 94, n. 1, pp. 143–151, 1947.

[119] PALOMARES, E., NIETO, A., MORALES, A., et al. "Dynamic behaviour of pneumatic linear actuators", *Mechatronics*, v. 45, pp. 37–48, 2017.

[120] BEATER, P. *Pneumatic drives*. Springer, 2007.

[121] SHADMAN, M. *Application of the latching control on a wave energy converter*. Doctoral thesis, Federal University of Rio de Janeiro, 2017.